The Improved Hydrogen Release of Sodium Amide-Sodium Borohydride System with Transition Metal Additions and Investigations of New Amide-Borohydride Systems as Potential Hydrogen Storage Materials

by

Cevriye Koz

A Thesis Submitted to the
Graduate School of Engineering
in Partial Fulfillment of the Requirements for
the Degree of

Master of Science
in
Material Science and Engineering
Koç University

August 2009

Koc University

Graduate School of Sciences and Engineering

This is to certify that I have examined this copy of a master's thesis by

Cevriye Koz

and have found that it is complete and satisfactory in all respects,
and that any and all revisions required by the final
examining committee have been made.

Committee Members:

_____

Mehmet Suat Somer, Ph. D. (Advisor)

_____

Annamaria Miko, Ph. D.

_____

Özgür Birer, Ph. D.

Date: _____

ABSTRACT

The present study consists of two main parts. T*he first one* is focused on improvement of the hydrogen release behavior of $NaNH_2$-$NaBH_4$ system. For this purpose, samples with different molar ratios of the constituents -sodium amide and sodium borohydride- were prepared by using ball-milling technique and transition metal additives as catalysts. In all cases, the product obtained after ball-milling was α-Na_2BNH_6 exhibiting the same thermal decomposition behavior as the previously synthesized one by the thermal method. According to the results of Mass Spectroscopy and DTA/TG, the addition of ~ 5 wt% of Pt, Pd, $PtCl_2$ and $PdCl_2$ decreased the dehydrogenation temperature of $NaNH_2$-$NaBH_4$ system approximately by 20-60 K. The most significant decrease in the hydrogen release temperature was observed in the presence of Pt/Vulcan carbon and Pd/Black Pearl. With the addition of 5.6 wt% Pt/Vulcan carbon, the temperature for hydrogen release decreased from 553 to 404 K, and a marked shift of 161 K was detected for the addition of 2.9 wt% Pd/Black Pearls. The hydrogen uptake experiments were performed at 473 K and 400 bar H_2 for additive free Na_3BN_2 and at 373 K and 350 bar H_2 pressure for samples with 5.6 wt% Pt/Vulcan carbon addition, respectively. No change was observed in the XRPD diagrams of the samples after hydrogen loading, except for the formation of NaH. The results indicate that the hydrogenation process for the sodium amide-borohydride system is not reversible under the given conditions.

In *the second part* of the study, the reaction conditions of the mixed alkali metal complex hydride systems of $LiNH_2$-$NaBH_4$, $LiNH_2$-KBH_4 and $NaNH_2$-KBH_4 (2:1 and 1:1 molar ratio) were investigated by using thermal and mass spectroscopic methods. The resulting intermediate and final products were characterized by X-ray powder diffraction, DTA/TG and vibrational spectroscopy (FT-Raman, FT-IR). According to the results of the DTA/TG and Mass spectroscopic measurements, the hydrogen release for the $LiNH_2$-$NaBH_4$ and $LiNH_2$-KBH_4 systems starts at 621 K and 683 K, respectively. While the dehydrogenation process of the $LiNH_2$-$NaBH_4$ samples

occurred in two steps, the latter decomposed in a single step, accompanied by high amount of NH_3 release. For both cases, the decomposition products identified were practically the same: Li_3BN_2, Na or K (trace) and amorphous boron.

Unlike the aforementioned two systems, the dehydrogenation for the $NaNH_2$-KBH_4 mixture starts at 596 K and peaking out at 700 K. The final product after the dehydrogenation process turned out surprisingly to be a hitherto unknown ternary nitridoborate, Na_2KBN_2, which crystallizes in the tetragonal space group $I\,4/mmm$ (No.139) with a = 4.2359(0) Å, c = 10.3014(2) Å and Z = 2. The crystal structure is characterized by elongated rhombic dodecahedra formed by 8 Na and 6 K atoms each which are centered by the linear $[N{-}B{-}N]^{3-}$ moieties. The (B–N) bond lengths are 1.357(4) Å. The vibrational spectra of Na_2KBN_2 were measured and interpreted based on the $D_{\infty h}$ symmetry of the linear $[N{-}B{-}N]^{3-}$ groups.

ÖZET

Bu çalışma iki ana başlıktan oluşmaktadır. Çalışmanın ilk kısmı $NaNH_2$-$NaBH_4$ sisteminin hidrojen verme özelliklerinin geliştirilmesi üzerine yoğunlaşmıştır. Bu amaçla, numuneler sodyum amid ve sodyum borohidritin farklı mol oranlarında bilyeli değirmen tekniğiyle sentezlenmiş ve geçiş metalleri de sisteme katalizör olarak eklenmiştir. Bilyeli değirmenle hazırlanan bütün numunelerden α-Na_2BNH_6 elde edilmiş olup, termal yolla sentezlenmiş numunelerle aynı termal bozunma özelliklerini göstermiştir. Kütle spektroskopisi ve termal analiz sonuçlarına göre kütlece %5'lik Pt, Pd, $PtCl_2$ ve $PdCl_2$ eklemeleri $NaNH_2$-$NaBH_4$ sisteminin hidrojen verme sıcaklığını 553 K' den yaklaşık olarak 20 ila 60 K kadar düşürmeyi başarmıştır. Sistemin hidrojen verme sıcaklığında en önemli düşüş karbon siyahı üzerine tutturulmuş Pt ve Pd' un eklenmesiyle gözlemlenmiştir. Kütlece % 5,6'lık eklenen Pt/Vulcan carbon sistemin hidrojen verme sıcaklığını 553 K' den 404 K' e düşürürken, kütlece % 2,9'luk Pd/Black Pearls hidrojen verme sıcaklığını yaklaşık olarak 161 K kadar azaltmıştır. Sistemin dekompozisyonundan sonra oluşan ürünün (Na_3BN_2) hidrojeni geri alma özellikleri incelenmiştir. Katalizör kullanılmadan elde edilen Na_3BN_2 ve kütlece % 5,6'lık Pt/Vulcan carbon eklenmiş Na_3BN_2 örnekleri 10 saat boyunca sırasıyla 473 K' de 400 bar hidrojen ve 373 K' de 350 bar hidrojen yüklenmesine maruz bırakılmıştır. Bu deneyler sonucunda, örneklerin X-ray kırınım difraktometresinde NaH oluşumu dışında herhangi bir değişiklik gözlemlenmemiştir. Bu sonuçlar, belirtilen şartlar altında sodyum amid – sodyum borohidrit sisteminin hidrojen verme reaksiyonunun tersinir olmadığını göstermektedir.

Çalışmanın ikinci kısmında, 2:1 ve 1:1 molar oranlarda hazırlanmış alkali metal kompleks hidritlerinin ($LiNH_2$-$NaBH_4$, $LiNH_2$-KBH_4 ve $NaNH_2$-KBH_4) termal bozunma özellikleri termal analiz ve kütle difraktometresi yardımıyla incelenmiştir. Reaksiyonlar sonucunda oluşan ara fazlar ve son ürünler X-ray kırınım spektroskopisi, DTA/TG, kütle ve titreşim spektroskopisiyle karakterize edilmiştir. Termal analiz ve kütle spektroskopisi sonuçlarına göre $LiNH_2$-$NaBH_4$ ve $LiNH_2$-KBH_4 sistemleri

hidrojen vermeye sırasıyla 621 K ve 683 K' de başlamaktadır. $LiNH_2$-$NaBH_4$ sistemi hidrojeni iki aşamada verirken, $LiNH_2$-KBH_4 sistemi hidrojeni yüksek miktarda NH_3 gazı ile tek basamakta verir. Bu iki sistemin termal bozunmasıyla oluşan ürünler (Li_3BN_2, Na ya da K ve B) benzerlik göstermektedir.

Yukarıda bahsedilen iki sistemden farklı olarak, $NaNH_2$-KBH_4 sistemi hidrojen vermeye 596 K' de başlar ve maksimum hidrojen salınımı 700 K' de gözlemlenir. Bu sistemin termal bozunması sonucunda oluşan son ürün şimdiye dek bilinmeyen tetragonal uzay gruba ($I\,4/mmm$ (No.139)) sahip bir nitridoborittir. Bu nitridoboritin, Na_2KBN_2, latis parametreleri a = 4,2359(0) Å, c = 10,3014(2) Å ve Z = 2 şeklinde hesaplanmış ve kristal yapısı 8 Sodyum, 6 Potasyum ve merkezde de lineer $[N{-}B{-}N]^{3-}$ bileşenlerinden oluşan 'elongated rhombic dodecahedron' olarak tanımlanmıştır. Boron ve nitrojen atomları arasındaki bağ uzunluğu 1.357(4) Å olarak hesaplanmıştır. Na_2KBN_2 bileşiğinin titreşim spektroskopi ölçümleri yapılmış ve bu ölçümler lineer $[N{-}B{-}N]^{3-}$ gruplarının $D_{\infty h}$ simetrisine sahip olduğu temel alınarak yorumlanmıştır.

ACKNOWLEDGEMENTS

Foremost, I owe my deepest gratitude to my supervisor, Prof. Dr. Mehmet Somer, who has supported me throughout my thesis with his patience and knowledge whilst allowing me work in his group.

I would like to thank Dr. Annamaria Miko who has provided assistance while I was writing my thesis. This thesis would not have been finished without her supports.

Also, I would like to express my gratitude to Prof. Dr. Can Erkey and his group members Betül Cangül and Ayşe Bayrakçeken for sharing their knowledge.

I am indebted to many of my colleagues to support me in numerous ways, especially Selçuk Acar, Aslıhan Kırcalı, Burcu Uslu, Atilla Aşar, Ali Baş, Semih Afyon, Ahmet Topçu, Zeliha Şentürk, Murat Gençoğlu, Tuğba Eynur, Sinan Öztürk, İlkin Kokal and Kamil Kiraz.

I want to express my gratitude to Dr. Gudrun Auffermann for High Pressure Experiments, Umut Aydemir and Dr. Raul Cardoso for XRD measurements, Dr. Yurii Prots for interpretation of the results, and finally Muharrem Usta for his amazing glass works.

I also thank to TUBİTAK (The Scientific and Technological Research Council of Turkey) for their financial support.

I would like to thank my parents for their support and encouragement and I dedicate my thesis to my family who never give up on me.

TABLE OF CONTENTS

LIST OF FIGURES

LIST OF TABLES

NOMENCLATURE

ΔH: Enthalpy change

$\Delta T_{1/2}$: Midpoint of hydrogen release reaction

ΔT: Temperature difference

amu: Atomic mass unit

CB: Carbon Black

CUTE: Clean Urban Transport for Europe

DC: Direct Current

DOE: Department of Energy

DSC: Differential Scanning Calorimetry

DTA: Differential Thermal Analysis

EIA: Energy Information Administration

ECTOS: Ecological City Transport *S*ystem Project

HT: High Temperature

HT-XRD: High Temperature X-Ray Diffraction

HSAB: Hard Soft Acid Base Principle

LT: Low Temperature

MID: Multiple Ion Detection

MS: Mass Spectroscopy

m/z: Mass to charge ratio

RF: Radio Frequency

RT: Room Temperature

T_{dec}: Decomposition temperature

T_{max}: Temperature at maximum amount of hydrogen release

TG: Thermal Gravimetry

STA: Simultaneous Thermal Analysis

XRD: X-Ray Diffraction

XRPD: X-Ray Powder Diffraction

Chapter 1

INTRODUCTION

1.1 Hydrogen as an Alternative Energy

The modern history of petroleum had begun with the extraction of oil from coal and kerosene in the mid 19th century. As a result, the uses for oil expanded to a variety of areas from heating to industrial and transportation needs. However, with the turn of the 21st century, world's population has increased to over six billion, a number that has quadrupled within the last hundred years [1]. As a consequence of increasing population, the need for energy sources has increased significantly. Today oil supplies about 40% of the world's energy and 96% of the transportation energy [2]. According to the most optimistic assumption of Energy Information Administration (EIA) on the long term world oil supply, the estimated peak year of production (the point in time when the maximum rate of global petroleum extraction is reached, after which the rate of production enters terminal decline) ranges from 2021 to 2067 [3]. It means roughly in 70 years, Earth's oil reserves will start to exhaust drastically. In addition, due to burning of the fossil fuel CO and CO_2 appear in the atmosphere. Therefore, the usage of fossil fuels can be addressed as the major reason of global warming causing environmental damage such as changes in the microclimate or increase of sea water level, floods, hurricanes and many other negative effects. Mainly because of exhaustion of the fossil fuel sources and the destructive effect on the environment it has become highly important to develop an alternative energy sources.

In recent years, improvements in clean and renewable energy technologies such as solar energy, wind power, geothermal energy, hydropower, biomass, and tidal (ocean) power have been accelerated. The energy, which is produced from these technologies, cannot be stored and transported efficiently. However it can be converted to electricity as an energy carrier, still important amount of electricity is lost during the

transportation on the electric power lines (for U.S.A 7.2 % in 1995). Hydrogen as an alternative energy source and carrier can also offer a new route to replace fossil fuel.

Hydrogen is very attractive for several reasons. First of all, hydrogen is able to carry energy without any loss for long distances with small pumping power. In addition, hydrogen can be produced by numerous techniques from many sources such as water, without emissions of pollutants and greenhouse gases. Furthermore, hydrogen gas can be burned or combined with oxygen in fuel cell to release energy and produce water with no pollution [4].

1.2 Requirements for On-board Applications of Hydrogen

Besides the good storage and transportation properties, hydrogen has roughly three times the energy content of gasoline on a per-weight basis, and this makes hydrogen as the most promising energy source for stationary and on-board applications. On the other hand, on volumetric basis, hydrogen's energy is only 8 MJ/L for the cryogenic liquid compared with gasoline's 32 MJ/L [5]. This huge energy difference on volumetric basis is the hindrance for on-board applications of hydrogen. The success to replace petroleum to hydrogen fuel in transportation depends on developing new infrastructures. The main problems are carrying hydrogen to the vehicle and storing useful quantities of hydrogen on-board.

Today, cars can be refueled in a few minutes and can travel approximately 300 miles (~ 483 km) with a full tank of gasoline [5]. For the public acceptance of hydrogen as a transportation fuel, hydrogen needs to satisfy the expectations of today's consumers. Because of this reason, U.S. Department of Energy (DOE) has set the targets for the performance of hydrogen powered cars which was reported in 2003.

According to the DOE report, in 2010 a hydrogen storage system should have an energy density of 7.2 MJ/kg and 5.4 MJ/L. For further future, 2015 DOE's standards becomes more strict and requires 9 wt% of hydrogen (0.081 kg/L hydrogen) or energy density of 10.8 MJ/kg and 9.7 MJ/L in new systems. This is greater than the density of

liquid hydrogen (the density of liquid hydrogen is approximately 70.9 kg/m^3) at 20 K and 1 atm) [6].

The most important parameters in DOE standards are:

i) *Gravimetric Capacity* which provides information on gravimetric basis about the usable, specific-energy from H_2 and calculated from the quotient of the net useful energy and the maximum system mass. Generally, the full mass is used for systems that gain weight and the highest mass during discharge used for the calculation.

ii) *Volumetric Capacity* denotes the usable energy density from H_2 calculated on volumetric basis as the quotient of the net useful energy and the maximum system volume.

iii) *Storage system cost*. This target refers to the total projected cost of the entire on-board hydrogen system including all hardware and storage media, plus for any component that would have to be replaced for the system to demonstrate a useful life of 15 years or 150,000 miles in a vehicle.

iv) *Fuel cost* which includes off-board costs such as liquefaction, compression, regeneration, and so on. The 2015 targets based on H_2 production cost of $1.50/gasoline gallon equivalent (pump price) untaxed.

v) *Operating ambient temperature.* The vehicles can be expected by consumers to operate perfectly in any weather conditions. Operating ambient temperature is stated as the ambient temperature plus full solar load number. The notation (sun) indicates the upper temperature and the hot soak condition in full direct sun.

vi) *Cycle life* (1/4 tank to full). Customers expect the fuel system to last the life of vehicle, typically 150,000 miles. Assuming a 300 mile range, that amounts to 500 full fill cycles.

vii) *Minimum and Maximum delivery temperature of H_2 from tank*

viii) *System Fill Time for 5-kg hydrogen*

ix) *Loss of useable hydrogen.* This target expresses the loss of usable hydrogen during extended periods of rest (for example parking during a vacation). Vehicles purchased by consumers will be expected to have minimal perceptible loss during few

weeks' disuse, similar to gasoline vehicles. The unit is given in (g/h)/kg, calculated from the hydrogen loss under any road conditions and divided by the stored hydrogen (kg).

x) *Purity (H_2 from storage system).*

The DOE standards values for development of new hydrogen storage systems are given in Table 1.1 in details.

Table 1.1: DOE Technical Targets: On-board Hydrogen Storage Systems [6]

Storage Parameter	**Units**	**2007***	**2010**	**2015**
Gravimetric Capacity	kWh/kg (wt% hydrogen)	1.5 (4.5%)	2 (6%)	3 (9%)
Volumetric Capacity	kWh/L (kg H_2/L)	1.2 (0.036)	1.5 (0.045)	2.7 (0.081)
Storage system cost	$/kWh net ($/kg H_2)	6 (200)	4 (133)	2 (67)
Fuel cost	$ per gallon gasoline equivalent at pump	3	1.5*	1.5*
Operating ambient temperature	K	253-323 (sun)	243-323 (sun)	233-333 (sun)
Cycle life (1/4 tank to full)	Cycles	500	1000	1500
Minimum and Maximum delivery temperature of H_2 from tank	K	253-358	243-281	233-358
System Fill Time for 5-kg hydrogen	Min	10	3	2.5
Loss of useable hydrogen	(g/h)/kg H_2 stored	1	0.1	0.05
Purity (H_2 from storage system)	98% (dry basis)			

* Note that compressed hydrogen and liquid hydrogen tanks fulfill some of the 2007 targets. These interim 2007 targets are primarily for materials-based technologies such as solid-state systems (e.g. complex metal hydrides) or liquids (such as liquid chemical hydrides).

Besides energy density, cost and safety are other important factors for public acceptance of hydrogen as fuel. According to some studies on "willingness to pay for hydrogen" the cost was another major barrier for development of hydrogen [7, 8].

1.3 Hydrogen Storage Methods

With the consideration of the requirements for the on-board application of hydrogen, many approaches to packing a large quantity of hydrogen in low weight, low volume systems has been studied. The five most important candidates for hydrogen storage are compression, liquefaction, physisorption, metallic hydrides and complex hydrides.

1.3.1 Compression

Compressed gaseous storage is the simplest way and the closest to technical feasibility because of simplicity and familiarity. Hydrogen gas can be stored in a cylinder of pressure up to 20 MPa. The major difficulty with compressed hydrogen is its energy density. The energy density of compressed hydrogen is too low to satisfy the fuel demand of on-board applications [9]. In addition to this, high-pressure tanks have complex structures containing multiple layers with strength and impact resistance. This means additional cost for high pressure tanks. Furthermore, the tanks must be cylindrical or near-cylindrical in shape and it limits the applications in small vehicles. On the other hand, these tanks can be used in large vehicles such as buses which have more available space, for example on the roof. The examples of the application of this method can be seen in Clean Urban Transport for Europe (CUTE) buses and with the Citaro buses of Ecological City TranspOrt *S*ystem Project (ECTOS) in Iceland [8, 10]. Figure 1.1 shows the general bus layout for the Mercedes Benz fuel cell Citaro.

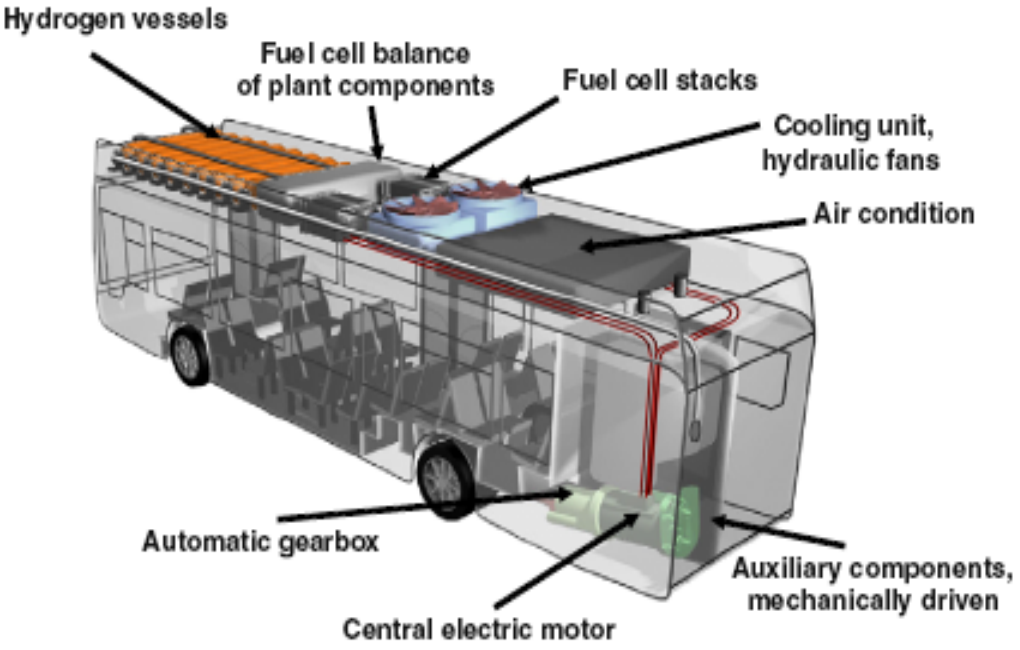

Figure 1.1: The Mercedes-Benz Fuel Cell Citaro [8]

1.3.2 Liquefaction

Hydrogen can be stored in cryogenic tanks as a liquid at 21.2 K at ambient pressure. The critical temperature of hydrogen is 33 K, therefore the liquid form can only be stored in open systems otherwise the pressure in the closed system can increase to ~ 10^4 bar at room temperature [11]. By this method, the volumetric capacity has been improved compared to compressed gas. However, this method has other two problems for the on-board applications; the large energy loss for liquefaction process and boil-off of the liquid. As reported by Pinkerton, approximately 30 % of the energy content of liquid hydrogen is lost for the liquefaction process [12]. In addition to liquefaction cost, boiling-off of the liquid limits this storage method. The gasification of the liquid hydrogen inside the cryogenic vessel is an unavoidable loss even with a perfect insulation. Although, the cost of liquid hydrogen storage is too much for the on-board

applications, as it can be seen in Fig. 1.2 this method is the closest one to the DOE 2010 targets from the aspect of energy density.

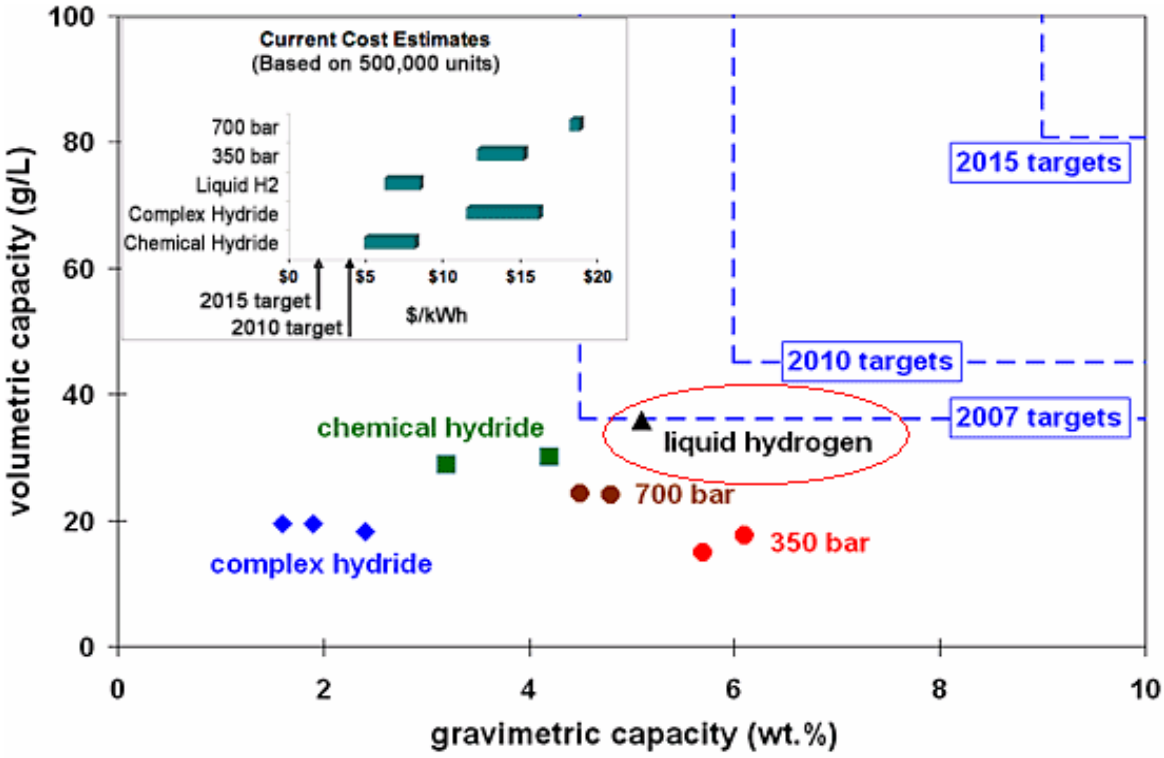

Figure 1.2: Status in terms of weight, volume and cost of existing hydrogen storage technologies for 2006 relative to the DOE targets [13]

1.3.3 Physisorption

The physisorption method is more reliable method when the storage reversibility is considered, because the adsorbed gas can be released reversibly. Activated or nanostructured carbon and carbon nanotubes are possible substrates for the physisorption. However, ongoing studies show that the storage at ambient temperature is too low to be practically utilized [9, 11].

1.3.4 Metallic Hydrides

Hydrogen can be chemically bound and stored as a solid compound. This storage method has been recognized as one of the most practical approaches for on-board applications. Because storing hydrogen in solid compounds permits to design flexibility in terms of shape of the container and its location on the vehicle.

The best known solid compounds for hydrogen storage are the reversible metal hydrides, such as magnesium hydride and lanthanum nickel hydride. MgH_2 contains 7.6 wt% hydrogen. This value approaches to feasible energy density which is targeted by DOE for 2010. Unfortunately, its operating temperature is above 623 K, which is too high for practical use [14-17]. Previous studies showed that the light alkali metal hydrides LiH and NaH are even more stable than MgH_2, with high decomposition temperatures exceeding 773 K [18]. Because of their high thermodynamic stability, these materials are not suitable for on-board applications. In order to lower high stability of these compounds, new metal hydride systems, such as magnesium nickel hydride, and lanthanum nickel hydride, were investigated. With the addition of more electronegative metal, especially transition metals, energy barrier for H_2 evolution decreases and decomposition temperature (T_{dec}) also thereby decreases. For example, at modest hydrogen pressures (a few bars) lanthanum nickel hydride, $LaNi_5H_6$, releases hydrogen at near room temperature [19]. However, scientists have found that in general, all reversible hydrides working under ambient temperature and pressure consist of transition metals. Therefore the gravimetric hydrogen density is limited below 3% by weight and this does not satisfy the on-board applications of hydrogen [5, 11, 17].

1.3.5 Complex Hydrides

Complex hydrides are compounds of light alkali metals with the complex anions such as $[BH_4]^-$, $[AlH_4]^-$ and $[NH_2]^-$. The usage of the complex hydrides as hydrogen storage material was proposed first by Bogdanovic and Schwickardi in 1997 when they

investigated the catalyzed hydrogenation of sodium alanate, $NaAlH_4$ [20, 21]. Beside the alanates, the hydrolysis reactions of $NaBH_4$ [22] and reversible reactions of lithium imides/amides ($Li_2NH/LiNH_2$) with hydrogen [23] have been reported in the following years. Due to their high theoretical energy density, (e.g. $NaAlH_4$: 7.4 wt% H_2 [24]) these complex hydrides are promising solid state hydrogen storage materials. But there are two major problems for on-board applications of complex hydrides: their slow kinetics and the high thermodynamic stability. Furthermore, hydrogen release occurs stepwise, due to the gradual decomposition of the complex hydride as observed in the case of $NaAlH_4$ (eq.1.1 and eq.1.2). This is the reason why a large difference between the theoretical and the practically attainable hydrogen capacities occurs [25].

However, recent studies showed that these difficulties can be overcome. If the problem is based on poor kinetics, using appropriate catalysts can be the solution. For the kinetically controlled $NaAlH_4$, different catalysts such as Ti, Zr, Ti_xAl_y and $TiCl_3$ were successfully applied [21, 26-31]. Another example is $LiAlH_4$, where Ti, Fe and some of their compounds were used to catalyze the dehydrogenation. [32-34].

Besides catalysis, the reaction kinetics of complex hydrides can be improved by mechanical milling [24, 31, 35-36]. Meisner *et al.* reported on the effects of ball-milling in the sodium alanate system. It was shown that diamond ball-milling of $NaAlH_4$ significantly decreases the decomposition temperatures. The reaction steps are presented in eq.1.1-1.2. The results of this study have revealed that the temperature of hydrogen release can be decreased from 523 K to 453 K when ball-milling was employed (eq.1.1). In the same manner, the dehydrogenation process completes at 508 K instead of 563 K (eq. 1.2) [36].

$$3NaAlH_{4(s)} \leftrightarrow Na_3AlH_{6(s)} + 2Al_{(s)} + 3H_{2(g)} \quad 3.70\ wt\%\ H_2 \quad (eq.\ 1.1)$$

$$Na_3AlH_{6(s)} + 2Al(s) \leftrightarrow 3NaH_{(s)} + 3Al_{(s)} + 1.5H_{2(g)} \quad 1.85\ wt\%\ H_2 \quad (eq.\ 1.2)$$

The improvement on the reaction kinetics by mechanical milling is based on reduced diffusion distances in solid hydrogen storage materials. This results in faster overall reaction kinetics.

On the other hand, if the barrier for the on-board application of the system is high thermodynamic stability, then the complex hydride can be destabilized by changing hydrogen bonding through substitution of the additive and the formation of new compounds during dehydrogenation [37-48].

Both thermal and kinetic destabilizations of complex hydrides are possible and these important properties make them promising candidates as hydrogen storage materials.

Recently, the theoretical and experimental investigations on hydrogen storage properties of Group I metal borohydrides, $LiBH_4$, $NaBH_4$ and KBH_4 [49-54] and amides, especially $LiNH_2$ [53, 55] attracted attention because of their high gravimetric density. However, none of them is capable to satisfy the DOE standards for on-board applications itself alone.

In 2005, two groups have reported a new quaternary hydride, $Li_3BN_2H_8$ with 11.9 wt% theoretical hydrogen capacity. The compound is formed by reaction of $LiNH_2$ and $LiBH_4$ mixtures in the molar ratio 2:1 (eq.1.3) [45, 56].

$$2LiNH_{2(s)} + LiBH_{4(s)} \xrightarrow{HEAT} Li_3BN_2H_{8(s)} \qquad \text{(eq.1.3)}$$

The destabilization of $LiNH_2$ with $LiBH_4$ promotes the formation of $Li_3BN_2H_8$ as intermediate compound. Figure 1.3 shows the predicted enthalpy changes for the dehydrogenation reactions of $LiBH_4$, $LiNH_2$ and LiH mixture, as well as destabilization of $LiBH_4$ on mixing with $LiNH_2$.

$LiBH_4$ is a stable salt and the dehydrogenation starts at quite elevated temperatures (~ 673 K) even in the presence of SiO_2 catalyst [49, 57]. According to the first-principle calculations, the enthalpy change for dehydrogenation of lithium borohydride decreases by 46 kJ/mol H_2, when destabilized with $LiNH_2$. The

experimental results confirmed the first-principle calculations: $Li_3BN_2H_8$ releases roughly more than 10 wt% hydrogen above 523 K.

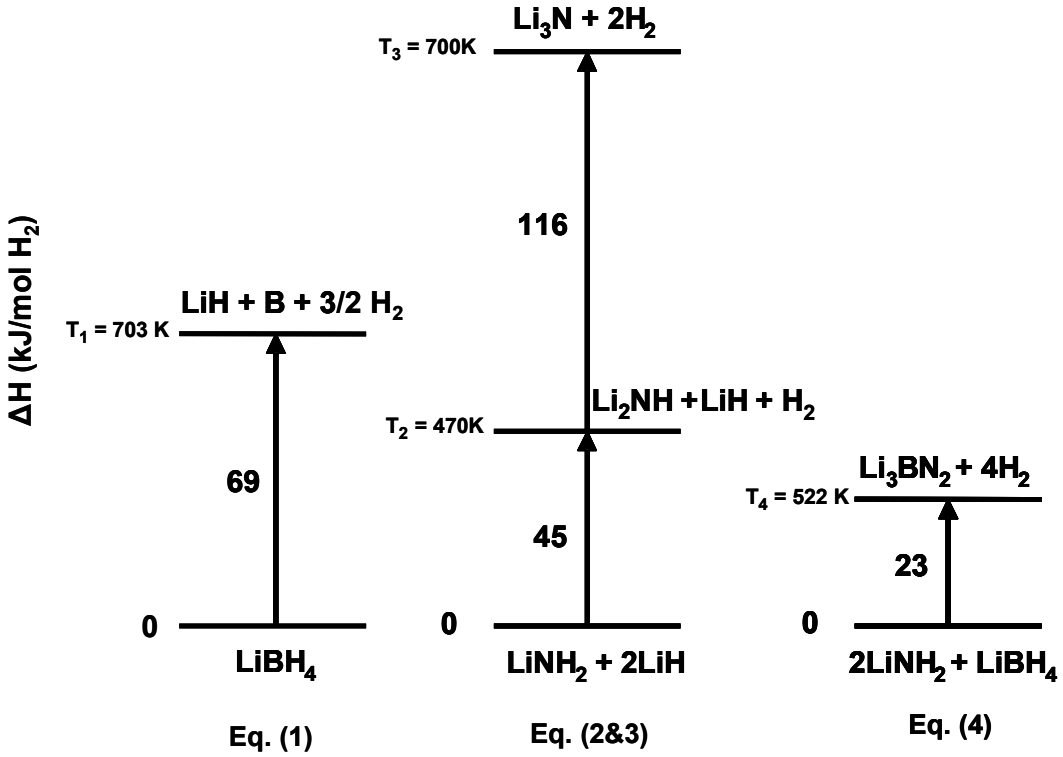

Figure 1.3: Predicted enthalpy changes, ΔH, for the dehydrogenation reactions of $LiBH_4$, $LiNH_2$ + 2LiH mixture and $2LiNH_2$ + $LiBH_4$ [46].

On the other hand, there are some disadvantages for its practical application as a hydrogen storage material. First of all, hydrogen release temperature is still too high for on-board applications. Secondly, the experimental studies on $LiNH_2$-$LiBH_4$ system showed that the hydrogen release of the system is an exothermic reaction and end product of ultimate dehydrogenation, Li_3BN_2, is thermodynamically favored. In order to overcome the first problem, small additions of transition metals such as Pt, Pd, Ni, and their chlorides, $PdCl_2$, $PtCl_2$ and $NiCl_2$ were used for kinetic destabilization. In the presence of small amount of additives, the hydrogen release behavior of $LiNH_2$-$LiBH_4$ system was successfully improved. For example, adding 11 wt% $NiCl_2$ to the system

reduces the midpoint temperature (at which temperature the hydrogen mass loss is 50 %) of hydrogen release by $\Delta T_{1/2}$ = 120 K compared to additive free system. Unfortunately, the high thermodynamic stability problem of the end product cannot be solved for the reversible reaction [58, 59].

The phase-analytical and thermal behavior of the $NaBH_4$- $NaNH_2$ system has been investigated since 2006 at Koc University under the leadership of Prof. Somer [60]. In the same year and independently, Charter *et al.* published an extended study focused on dehydrogenation behavior of the $LiNH_2$-$LiBH_4$ system, also mentioning the existence of a new compound Na_2BNH_6, obtained from the reaction of equimolar amounts of $NaNH_2$ and $NaBH_4$ [61]. Different from its Li analogue (Li_2BNH_6), the sodium compound hydrogen release mechanism follows the reaction:

$$Na_2BNH_{6(s)} \xrightarrow{HEAT} 2NaH_{(s)} + B_{(s)} + \tfrac{1}{2} N_{2(g)} + 2H_{2(g)} \qquad \text{(eq. 1.4)}$$

$NaBH_4$ has a theoretical hydrogen capacity of 14 wt%, decomposing over 838 K. It was shown that after the addition of $NaNH_2$, the decomposition temperature decreases to 563 K [60], which is, however, still too high for the on-board applications.

Our pervious investigations concentrated on the $NaNH_2$-$NaBH_4$ system and the phase and thermal analyses of molten mixtures in the mol range 1:1- 4:1 ($NaNH_2$: $NaBH_4$), as well as their Vibrational and Mass Spectroscopy analyses. The results can be summarized as follows [60, 62]:

$Na_2BNH_6 \equiv Na_2[BH_4][NH_2]$ is the only stable phase which could be detected in the quasi-binary $NaNH_2$: $NaBH_4$ system existing in two different modifications: the low temperature (LT) β- and the high temperature (HT) α-phase. The latter corresponds to the compound reported by Charter et al. [61].

α-Na_2BNH_6 can be obtained by heating the starting binaries (molar ratio = 1:1) to 502 K for 1 h. On longer annealing (T = 342 K, 10 day), HT α-phase converts completely to LT β-phase. The cubic α-Na_2BNH_6 crystallizes in the K_3SO_4F-type of

structure (Space group: $Pm\bar{3}m$; Z = 1) with a = 4.7111(2) Å. β-Na_2BNH_6 is orthorhombic (Space group: *Pbcm*; Z = 4) with *a* = 6.5384(2), *b* = 6.4960(1), *c* = 9.8512(2) Å. The two crystal structures can be considered as an order-disorder derivative of the perovskite type structure (ABO_3), with $[BH_4]^-$ and $[NH_2]^-$ at A and B sites, respectively. Na ions center $^2/_3$ of the O positions. The presence of the two different anions - $[BH_4]^-$ and $[NH_2]^-$ - in the solids was also confirmed by the vibrational spectra.

According to the results of the differential thermal analysis (DTA) and high temperature X-ray diffraction (HT-XRD) measurements, the $NaNH_2$ and $NaBH_4$ react at 430 K to form α-Na_2BH_6 which remains stable until the melting point of 492 K. Between 492-573 K, no significant effects were detected both on DTA and thermal gravimetric (TG) curves. Above 573 K, however, a sudden decomposition takes place in two steps (559 K, 689 K) causing a total mass loss of 8 %. The gaseous species formed during the decomposition process were followed by mass spectrometer (MS). The mass spectra obtained from 1:1 and 2:1 mixtures of $NaNH_2$ and $NaBH_4$ in the range 773 K > T > 492 K prove that the main gaseous product evolved during the thermal decomposition is H_2. NH_3 and H_2O were also detected, but their concentration is quite low. These findings confirm that the mixture of the complex hydrides $NaNH_2$–$NaBH_4$ (molar ratio ≥ 1:1) - likewise the $LiNH_2$–$LiBH_4$ system - are potential candidates for solid hydrogen storage materials. The composition of the solid residues after the thermal treatment depends on the molar ratio of the starting binaries $NaNH_2$ and $NaBH_4$. While Na_2BNH_6 (1:1) decomposes to a mixture of NaH, Na and an unidentified amorphous solid, mixtures ≥ 2:1 yielded exclusively Na_3BN_2.

Our differential scanning calorimeter (DSC) measurements showed that the formation of end product, Na_3BN_2, from the mixture of $NaBH_4$ and $NaNH_2$ is an endothermic reaction. It means that unlike Li_3BN_2, the hydrogen uptake of Na_3BN_2 might be thermodynamically more favored [60].

$$2NaNH_{2(s)} + NaBH_{4(s)} \xrightarrow{HEAT} Na_3BN_{2(s)} + 4H_{2(g)} \qquad \text{(eq. 1.5)}$$

Concerning the possible on-board application, the above mentioned investigations on the $NaNH_2$-$NaBH_4$ system left some questions open. These were:

- How does ball-milling - i.e. particle size - affect the hydrogen release and uptake behavior of the mixed $NaNH_2$-$NaBH_4$ samples?
- Is it possible to decrease the temperature of dehydrogenation by addition of catalysts as it was shown for other similar systems [58, 59]?
- How can the reversibility of the hydrogen release for this system be improved and how can be rehydrogenation enhanced? What is the role of catalysts in the hydrogen uptake process?
- How is the thermal behavior of mixed complex hydride systems, e.g. $LiNH_2$-$NaBH_4$?

The aim of the present thesis is to find the answer to these questions and propose a possible complex hydride mixture for on-board application. *The first part* of the thesis reports on the investigation of the Na_2BNH_6 synthesis from *$NaNH_2$-$NaBH_4$* mixture using ball-milling method. The reactants were ball-milled for different duration time and speed with different catalysts. The optimum parameters for the end product (*Na_2BNH_6*) formation were determined. Following the *Na_2BNH_6* synthesis, the catalytic effects of Pd, Pt, their chlorides and carbon black compounds on the thermal decomposition behavior of *$NaNH_2$-$NaBH_4$* (2:1 molar ratio) were examined by DTA/TG complemented with Mass Spectroscopy. The components and the possible reaction mechanism were followed by phase-analytical, thermal and mass spectroscopic measurements. As the final step, the hydrogen uptake possibility after hydrogen release of the end products - with and without additives- was studied by using an autoclave with H_2 gas loading at elevated temperatures.

The second part of the thesis is dedicated to the investigations of the phase-analysis and thermal behavior of mixed complex hydride systems of

i) $LiNH_2$-$NaBH_4$,
ii) $LiNH_2$-KBH_4, and
iii) $NaNH_2$-KBH_4.

The hydrogen release temperature and the compounds in the gas phase were determined at different molar ratio of the mixtures. The resulting end products and the crystalline structure of the new compounds were investigated and clarified by phase-analytical, thermal, vibrational and mass spectroscopic measurements. Depending on the gravimetric capacity and possible operating ambient temperature the three systems was compared and classified. The results are reported below.

Chapter 2

SYNTHESIS & CHARACTERIZATION

2.1 SYNTHESIS

Due to the sensitivity to air and moisture, the entire manipulation of starting materials and products, such as weighing, loading and unloading were carried out in a glove box under inert atmosphere (N_2; O_2 < 1ppm, H_2O < 1ppm).

2.1.1 Mechanochemical Synthesis

2.1.1.1 Theory

The different fields of chemistry were classified according to the type of energy supplied to the system by W. Nernst. Some of these fields are thermochemistry, electrochemistry, photochemistry, and mechanochemistry. The name of mechanochemistry is used for the field of reactions caused by mechanical energy. The mechanochemical processing in a mill – tribochemistry – is the most common operation in this area [63].

Until very recently, it has been recognized that the cause of chemical reactions during the mechanical milling is the thermal load due to the friction. However, the recent studies indicated that the reason of the reactions is not only the thermal load. Generation of clean and fresh surfaces and new contact zones between solid reagents, increase in surface area and the defect density are some of the reasons for the chemical reactions during mechanical milling [64-68].

Recently, mechanochemically initiated solid state processes have become popular in many studies, especially synthesis of complex metal hydrides as hydrogen storage materials [16, 24, 31, 35-36]. Probably, this is due to the potential applications

of such reactions in technology, particularly for the development of the so called dry processes. These are cost effective and more environmental friendly methods with minimum energy consumption.

In our study, mechanochemical synthesis was chosen as a synthesis method because of three reasons. First of all, the compound Na_2BNH_6 had already been synthesized by thermal process, but the route via "planetary ball-milling" was not investigated until our study.

Secondly, in contrast to conventional thermally activated process, the surface area of the reactants increases as a result of progressive dispersion and fine mechanical mixing of the powders. The studies on $NaAlH_4$ indicate that ball-milled sodium alanate has lower decomposition temperature than that of the non-treated sodium alanate [16, 24, 36].

Finally, the main reason for choosing the ball-milling method in our system is the "dry" catalysts application. In our case the catalyst has to be maintained in solid state and ball-milling is one of the most efficient methods for this purpose. As a known fact, the efficiency of the catalyst depends critically on the surface area (or particle size) and how well dispersed through the system [16]. Ball-milling can fulfill all these requirements to disperse catalysts homogenously in $NaNH_2$-$NaBH_4$ solid state system.

2.1.1.2 Planetary Ball-mill

A popular mill for performing mechanochemical solid state reactions is the planetary ball-mill. The name of the planetary ball-mill comes from the planet-like movement of its pots. The planetary ball-mill can be described as installed pots on a disk. The pots and the disk are simultaneously and separately rotated around their own axes at a high speed (Figure 2.1).

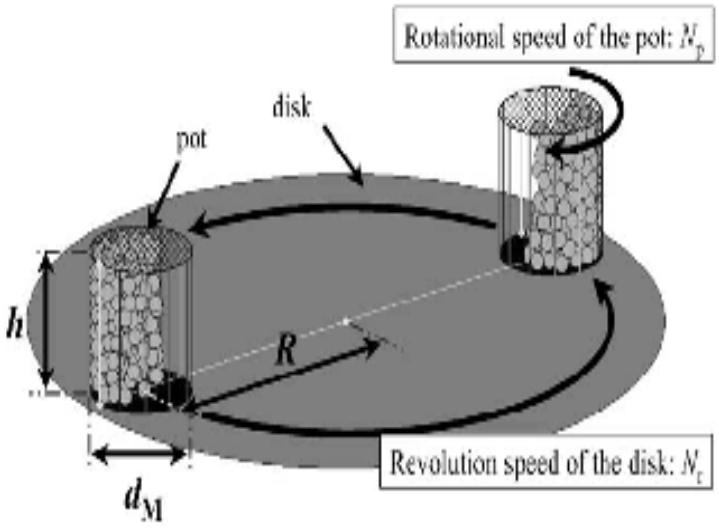

Figure 2.1: Schematic diagram of the planetary ball-mill. [69]

The centrifugal force produced by the pots rotating around their own axes and that produced by the rotating support disk both act on the pot contents, consisting of material to be ground and the grinding balls. Since the pots and the supporting disk rotate in opposite directions, the centrifugal forces alternately act in like and opposite directions (Figure 2.2). This causes the grinding balls to run down the inside wall of the pots. This process is followed by the material being ground and grinding balls lifting off and traveling freely through the inner chamber of the pot and colliding against the opposing inside wall. During these processes the friction and impact effects, which cause the thermal load, occur on the grinding material. The impact energy of grinding balls is a key factor to control grinding performance and it depends on operating parameters, especially rotation speed and its direction of the pot to that of the revolution of the disk [69-71].

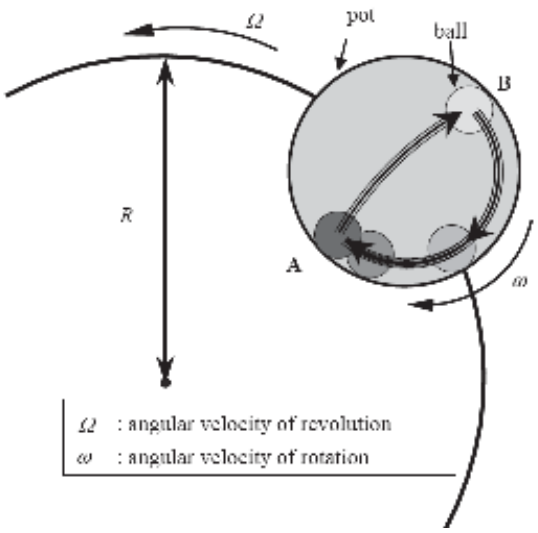

Figure 2.2: The movement of a ball in the pot. [69]

2.1.1.3 Experimental Procedure

For the mechanochemical synthesis of samples, Fritsch Pulverisette 7 premium line Planetary Mill was used. The synthesis process consists of two steps: loading powder mixture and grinding medium (45 zirconia balls with 5 mm in diameter) in a zirconia bowl under an inert gas atmosphere (to protect the mixture from the hydroxylation during the milling); and milling for the desired length of time and milling speed.

In our studies, the optimum milling speed and time were determined as 1000 rpm and 4.5 hours, respectively. Usually, 1.0 g of the $NaNH_2$:$NaBH_4$ (2:1 molar ratio) powder mixture with intended weight fraction of additives, were prepared for synthesis. Weight percentages of the used additives (Table 2.1) were calculated with the following formula.

$$\frac{weight\ \ of\ \ additive}{weight\ \ of\ \ NaNH_2 - NaBH_4\ \ mixture} x100\ \ (in\ \ \%) \qquad \text{(eq. 2.1)}$$

Table 2.1: Additives used as catalysts for the $NaNH_2$:$NaBH_4$ mixtures.

Transition metals	Chlorides of transition metals	Supported Transition metals on carbon*
Pd, Pt, Ni, Ti.	$PdCl_2$, $PtCl_2$, $TiCl_3$,	50 % Pt/Vulcan carbon (commercial), 20 % Pt/Vulcan carbon (commercial), 20 % Pd/Black Pearl(synthesized) 12 % Pd/Black Pearl(synthesized)

* Pt and Pd loadings on carbon blacks are given in weight percentage.

2.1.2 Thermal Decomposition and Synthesis

The equipment to study the decomposition reactions is given in Figure 2.3. Thermal decomposition reactions were performed in silica tubes with a vertical oven under N_2 gas. Approximately 500 mg sample was loaded into alumina crucible which was in turn placed in a silica ampoule. For the decomposition of the Na_2BNH_6 samples synthesized from different $NaNH_2$:$NaBH_4$ mixtures – with and without additive – the following temperature program was adjusted.

Step 1: 298 K → 663 K in 2 hours
Step 2: 663 K – 663 K for 2 hours
Step 3: 663 K → 298 K in 2 hours

The same set up was used for the synthesis of new alkali metal amide-borohydrides as well (Figure 2.3). The molar ratios of the starting mixtures $LiNH_2$:$NaBH_4$, $LiNH_2$:KBH_4 and $NaNH_2$:KBH_4 were 1:1 and 2:1. In a typical experiment, 500 mg of a sample was heated to target temperature and the products were monitored with powder X-ray diffraction (XRPD) measurements.

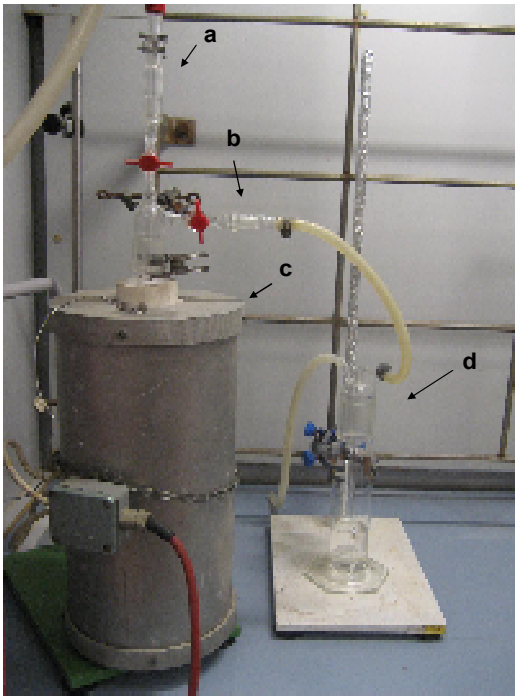

Figure 2.3: The experimental setup for decomposition reactions a) Inert gas inlet, b) Inert gas outlet, c) Vertical tubular oven, d) Silicon oil bubbler.

2.1.3 Hydrogen Uptake Experiments

Roth high-pressure laboratory autoclave (Model II) with 250 ml cylinder, which is designed for max. 200 bar working pressure and max. 573 K, was used for performing rehydrogenation experiments (Figure 2.4).

Several experiments were conducted on additive free Na_3BN_2 and 5 wt% Pt/Vulcan carbon added Na_3BN_2 samples. Pressure range between 85-170 bars H_2 load and temperature range between 363-423 K were selected for the experiments. Samples were exposed to H_2 under these conditions approximately for 10 hours. After the high-pressure experiments the changes were monitored by XRPD.

Figure 2.4: The basic equipment of Roth high pressure laboratory autoclave Model II 1) autoclave cylinder, 2) autoclave head, 3) fine control valve, 4) pressure gauge and 5) temperature sensor.

2.2 CHARACTERIZATION

2.2.1. X-ray Diffractometry (XRD)

2.2.1.1 Theory

X-ray diffractometry, using single crystals or powder is mainly related to structure analysis.

X-ray diffraction is based on the interaction of monochromatic X-rays and the sample's crystalline lattice. When X-radiation scatters from electron density of the matter it provides information about the atomic spacing parameters of the lattice. The X-radiation is generated by a cathode X-ray tube, filtered to produce monochromatic radiation, collimated to concentrate, and directed toward the sample. The interaction of the incident X-rays with the electrons in the crystal lattice produces constructive

interference and a diffracted X-ray when conditions satisfy Bragg's Law. The geometrical explanation of Bragg's Law is shown in Figure 2.5. The general relationship between the known wavelength of the incident X-rays, λ, the angle of incidence, θ, and spacing between the crystal lattice planes of atoms, d, is known as Bragg's Law, expressed as the following

$$n\lambda = 2d\sin\theta \qquad \text{(eq. 2.2)}$$

where n (an integer) is the "order" of reflection [72].

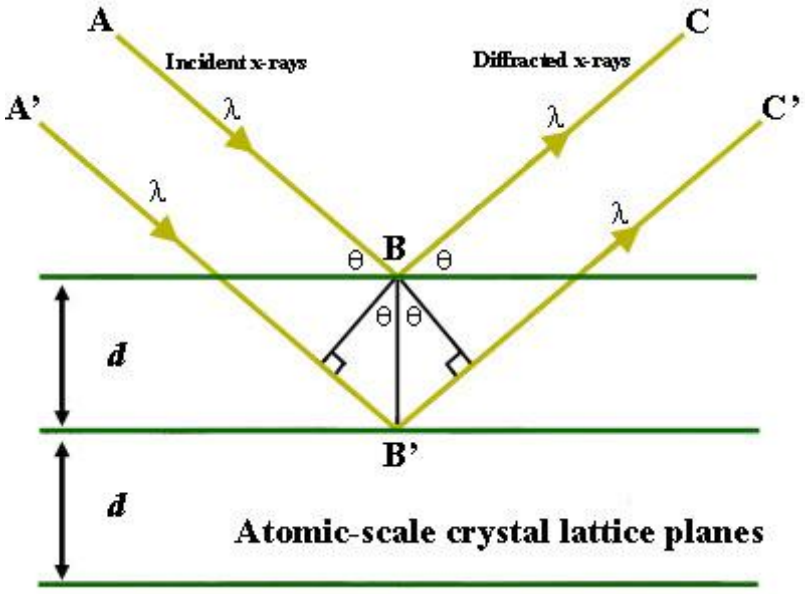

Figure 2.5: The geometrical explanation of the Bragg's Equation [73].

The simple mechanism of an X-ray Diffractometer is shown in Figure 2.6. X-rays from the tube (T) are incident on a crystal or powder sample (C) which may be set at any desired angle to the incident beam by rotation about an axis through (O), the center of the spectrometer circle. When the geometry of the incident X-rays impinging the sample satisfies the Bragg Equation (eq. 2.2), constructive interference occurs and a

peak is detected. The detector (D) measures the intensity of the diffracted X-rays for various angles θ. After a scan, the scattered X-ray intensity is plotted against the angle 2θ to produce a diffractogram [74].

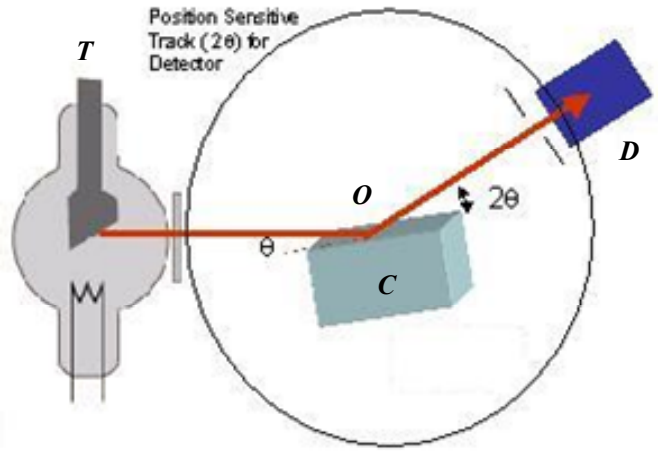

Figure 2.6: The schematic diagram of X-ray Diffractometry

X-ray powder diffractometry (XRPD) is mainly used for the identification of compounds, determination of crystal structure using Rietveld refinement, crystalline state, unit cell dimensions and internal strain. In addition, the information about particle size and surface area of nanocrystals can be gained from XRPD measurements.

2.2.1.2 Rietveld Analysis

The Rietveld method is used to obtain detailed crystal structural information from the powder diffraction data of the materials which are not available as single crystals. In Rietveld method, the least-squares refinements are carried out until the best fit is obtained between the entire observed powder diffraction pattern and the entire calculated pattern based on the simultaneously refined models for crystal structures [75]. In our study, the Rietveld analysis of the phases was performed by WinCSD program [76].

2.2.1.3 Particle Size and Surface Area Calculations

The crystallite size, *D*, can be estimated from the peak width with the Scherrer's formula

$$D = \frac{K\lambda}{B\cos\theta_B} \qquad \text{(eq. 2.3)}$$

where λ is the X-ray wavelength (in Å), B is the full width of height maximum (FWHM) of a diffraction peak (in degree), θ_B is the diffraction angle (in degree), and K is the Scherrer constant ($K = 0.9$) [77].

Assuming that the nanocrystals are spherical and have uniform size, the surface area (or roughness factor) can be expressed by the following equation where ρ is the density of the particles and d is the diameter of the particles [78].

$$S = \frac{6}{d\rho} \qquad \text{(eq. 2.4)}$$

2.2.1.4 Experimental Procedure

During our study, all samples were obtained only as microcrystalline powders. Therefore, X-ray powder diffraction method was used for the characterization of the structures. The XRPD measurements of the samples were performed with an Imaging Plate Guinier Diffractometer 670 using Cu$K\alpha_1$ (λ = 1.5405 Å) radiation with a germanium monochromator. Rietveld analysis, particle size and surface area calculations of samples were done by using the XRPD results.

2.2.2 Differential Thermal Analysis/Thermal Gravimetry

2.2.2.1 Theory

Differential Thermal Analysis (DTA) is a technique in which the temperature difference between a sample and a non reactive reference is measured as a function of temperature, when the sample and reference are exposed to the same heating program. The sample and the reference sample are placed symmetrical with respect to the furnace. The temperature difference between sample and reference is measured by "differential" thermocouples [79].

Using differential thermal analysis method, we can gain information about the temperature range where possible reactions and phase transformation appear due to thermal treatment [80]. When the sample undergoes a transformation, it will either absorb (endothermic) or release (exothermic) heat. Besides, the temperatures of transformations, the thermodynamics (enthalpy) and kinetics of a process may be determined using DTA.

Thermogravimetry (TG) is a method in which the mass of a substance is measured as a function of temperature while the substance is subjected to a controlled temperature program. This method is useful for determination of the weight gain or loss of a condensed phase due to gas release or absorption as a function of temperature.

Different thermal analysis techniques can be combined into one single device. The total information about the sample obtained with the combination of DTA/TG technique provides many advantages. Because TG cannot be used to detect melting, while melting and decomposition cannot be distinguished unambiguously using DTA performing measurements, both techniques is necessary. A substance which melts with accompanying decomposition must be studied using both DTA and TG simultaneously. Simultaneous Thermal Analysis (STA) technique, involves measurements of both thermal and mass change concurrently on the same sample [79]. A schematic diagram of STA device which is combined DTA/TG system is given in Figure 2.7.

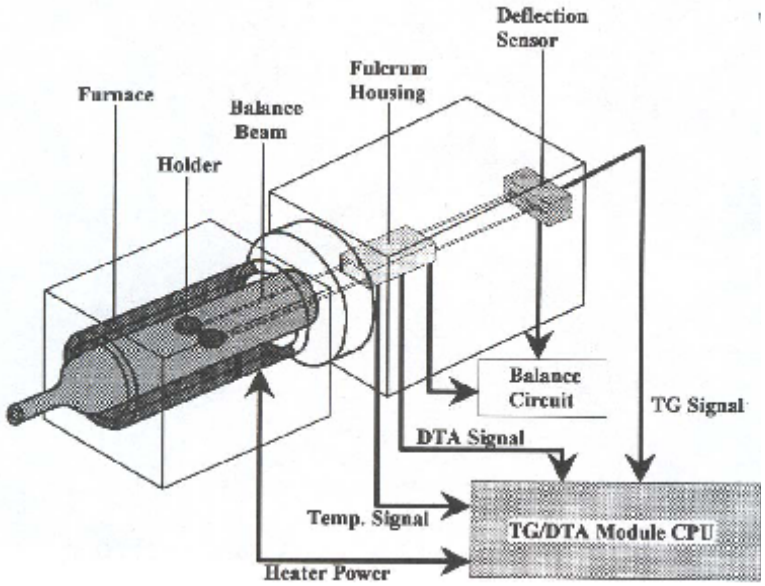

Figure 2.7: Schematic diagram of DTA/TG (STA) Seiko SSC 5200 model. [80]

2.2.2.2 Experimental Procedure

Thermal Analysis measurements were conducted in DTA/TG (STA) Seiko SSC 5200 model apparatus. Approximately 10 mg of sample was loaded into Al crucible. The endothermic and exothermic changes were monitored during heat treatment. The temperature program was set to heat the samples from room temperature to 873 K with 10 K/min heating rate. The experiments were carried out in inert atmosphere under 200 NmL/min Ar flow.

Temperature calibration of the STA was done by auto correction program of the system software and measuring the melting points for known metals such as Indium ($T_{melting}$ = 429.6 K) and Tin ($T_{melting}$ = 505 K).

2.2.3 Mass Spectroscopy

2.2.3.1 Theory

During the heating, many samples release gases or vapor through desorption or decomposition. This release is accompanied by thermal effects and mass-losses which can be detected by appropriate thermal analysis technique e.g. DTA and TG, respectively. One possible solution for the identification of the gases evolved from a thermal analysis instrument is to connect the thermal analysis equipment to mass spectrometer via capillary inlet as shown in Figure 2.8.

The mass spectrometer (MS) is an instrument, which separates rapidly moving ions on the basis of their mass to charge ratios. The mass spectrometer principle consists of generating gas-phase ions, separating them according to their mass-to-charge ratio using electric fields (sometimes magnetic fields as well) in an evacuated volume, and counting the number of ions. [81]

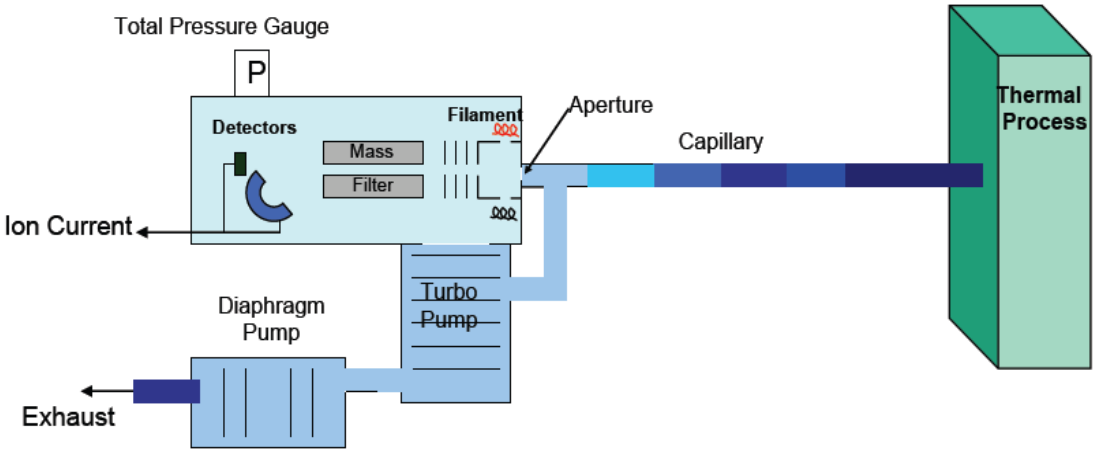

Figure 2.8: Schematic diagram of simultaneous DTA/TG and Mass Spectroscopy. [82]

Usually, mass spectrometers are named with the mass filter (or analyzer) which is used in the equipment. A quadrupole mass spectrometer intended for partial pressure

measurements is in principle an ionization vacuum gauge equipped with an additional device, the rod system. As the name implies, quadrupole mass analyzers consist of four parallel rods arranged as it is shown in Figure 2.9. The quadrupole instrument is built up from four parallel cylindrical rods. The opposite rods are connected electrically, one pair is attached to the positive pole of the variable direct current source while the other pair to the negative pole. In addition, a high frequency alternating voltage is applied to each pair. After ionization, a positive ion entering the quadrupole will be drawn towards a negatively charged rod. Under the influence of the combination of fields the ions undergo complex trajectories. Within certain limits these trajectories are stable and so ions of a certain m/z are transmitted by the device, whereas ions with different m/z values will have an unstable trajectory and be lost by collision with the rods [80-85].

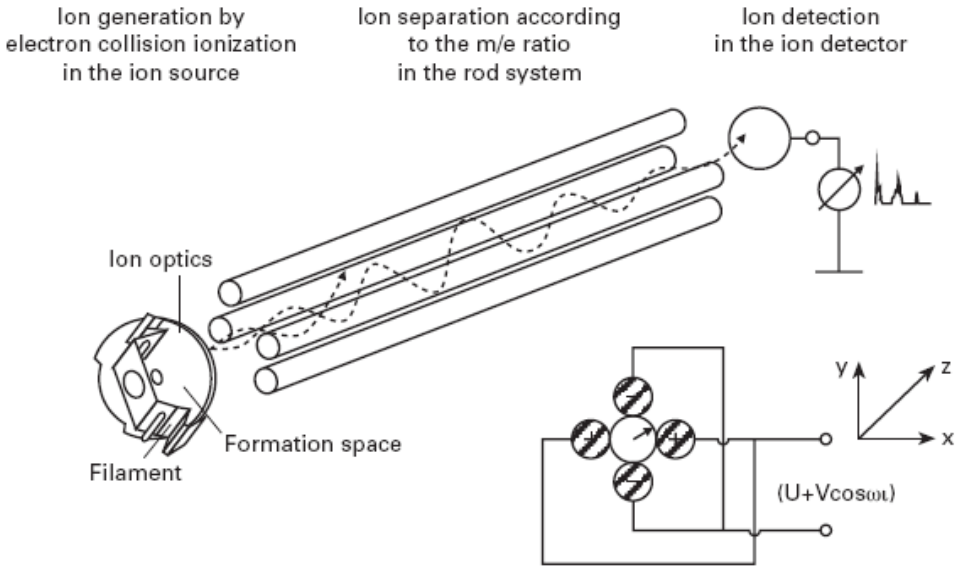

Figure 2.9: Schematic diagram of quadrupole mass filter. [82]

2.2.3.2 Experimental Procedure

A quadrupole mass spectrometer (ThermoStar^{TM} GSD 301 T) was used for the characterization of released gases during the decomposition of the samples with thermal

process. Once sample loaded into DTA/TG instrument, a flow of Ar passed over the sample with 200 NmL/min. DTA/TG and mass spectrometer connected via a capillary and worked in tandem. Multiple Ion Detection (MID) mode was used with the chosen mass channels of 2 ($H_2^{\bullet+}$), 16 ($NH_2^{\bullet+}$), 17 ($NH_3^{\bullet+}$/$OH^{\bullet+}$), 18 ($H_2O^{\bullet+}$), 28 ($N_2^{\bullet+}$), 32 ($O_2^{\bullet+}$), 36 ($HCl^{\bullet+}$) and 40 ($Ar^{\bullet+}$). For each mass channel auto gain factor was used. Ion currents of the selected mass channels were recorded versus time during the mass spectrometer measurements.

2.2.4 Vibrational Spectroscopy

Vibrational spectroscopy measurements were done for the characterization of the new product, Na_2KBN_2.

2.2.4.1 Infrared Spectroscopy

The Infrared measurements were performed by using KBr pellets with JASCO FT-IR 600 Spectrometer in the range of 4000-400 cm^{-1} and under nitrogen gas. All data manipulations were done by using JASCO Spectra Manager Software [86].

2.2.4.2 Raman Spectroscopy

The FT-Raman measurements were conducted on powdered samples sealed in Pyrex tubes (∅ = 4 mm) with a Bruker RFS 100/S spectrometer (Nd: YAG-Laser, 1064 nm, 200 mW) and the data manipulations were done by using OPUS^{TM} software [87].

Chapter 3

3. Kinetic Destabilization of Sodium Amide-Sodium Borohydride System

In previous studies, Na_2BNH_6 was synthesized by thermal treatment from $NaNH_2$ and $NaBH_4$ mixtures. As a result of the thermal treatment, two phases of Na_2BNH_6, cubic (high temperature) form and orthorhombic (low temperature) form were reported [60, 61].

The first part of our study concentrated on the synthesis of Na_2BNH_6 by ball-milling method. A new route was elaborated with the optimization of the ball-milling technique. After the mechanochemical synthesis, the kinetic destabilization of 2:1 molar ratio $NaNH_2$-$NaBH_4$ system in the presence of transition metals and their chlorides was investigated in detail. In the following part, the effects of the additives on hydrogen release behavior of the Na_2BNH_6 system will be presented.

3.1 Synthesis of α-Na_2BNH_6 with the Ball-milling Method and Thermal Decomposition Analysis of the Product

According to the reaction stoichiometry, 2:1 molar ratio of $NaNH_2$ - $NaBH_4$ mixture is the most preferred for maximum theoretical H_2 concentration and Na_3BN_2 formation (eq.3.1). Therefore, my work concentrates mainly on the synthesis of Na_2BNH_6 from the theoretical $NaNH_2$ and $NaBH_4$ mixture at 2:1 molar ratio.

$$2NaNH_{2(s)}+NaBH_{4(s)} \xrightarrow{HEAT} Na_2BNH_{6(s)}+NaNH_{2(s)} \xrightarrow{HEAT} Na_3BN_{2(s)}+4H_{2(g)} \quad \text{(eq. 3.1)}$$

The optimum ball-milling time and speed was determined at 2:1 molar ratio of $NaNH_2$–$NaBH_4$ mixture. The reactants were loaded to the reaction chamber together with the grinding medium and ball-milled for 1, 2, 3, 4 or 4.5 hours. The milling speed was altered between 300 rpm, 500 rpm and 1000 rpm at different ball-milling time.

After each ball-milling time and speed, the reaction mixture was removed completely and the phase analysis was conducted based on the XRPD results. The characteristic peaks of the end product, α-Na_2BNH_6, appeared on the X-ray diffractogram after 1 hour of ball-milling time at 1000 rpm and after 2 hours at 500 rpm. Fig. 3.1 shows XRD diagram of $NaNH_2$-$NaBH_4$ mixture (molar ratio 2:1) before and after ball-milling. Having ball-milled for 4.5 hours, the mixture was converted to α-Na_2BNH_6 and unreacted $NaNH_2$ was in presence. The optimum milling speed and time were determined as 1000 rpm and 4.5 hours, respectively. Unless it is mentioned differently, the samples in this chapter were ball-milled with these conditions.

Similar to the work of S. Acar [60], the main end product was α-Na_2BNH_6 but no β-phase was detected. The effect of the reactant's molar ratio on the formation of Na_2BNH_6 phase was also investigated at 1:1, 2:1, 3:1 and 4:1 $NaNH_2$ and $NaBH_4$ mixture. The mixtures of $NaNH_2$ and $NaBH_4$ in different molar ratios (i.e. 1:1 to 4:1) were ball-milled in time intervals of 1-5 hours and the products were monitored by XRPD. The results are not shown here but it is worth mentioning that no β-phase formation was observed under these conditions as well. We assume that the "thermal loading" during the ball-milling was much more than the needed energy for α → β transformation.

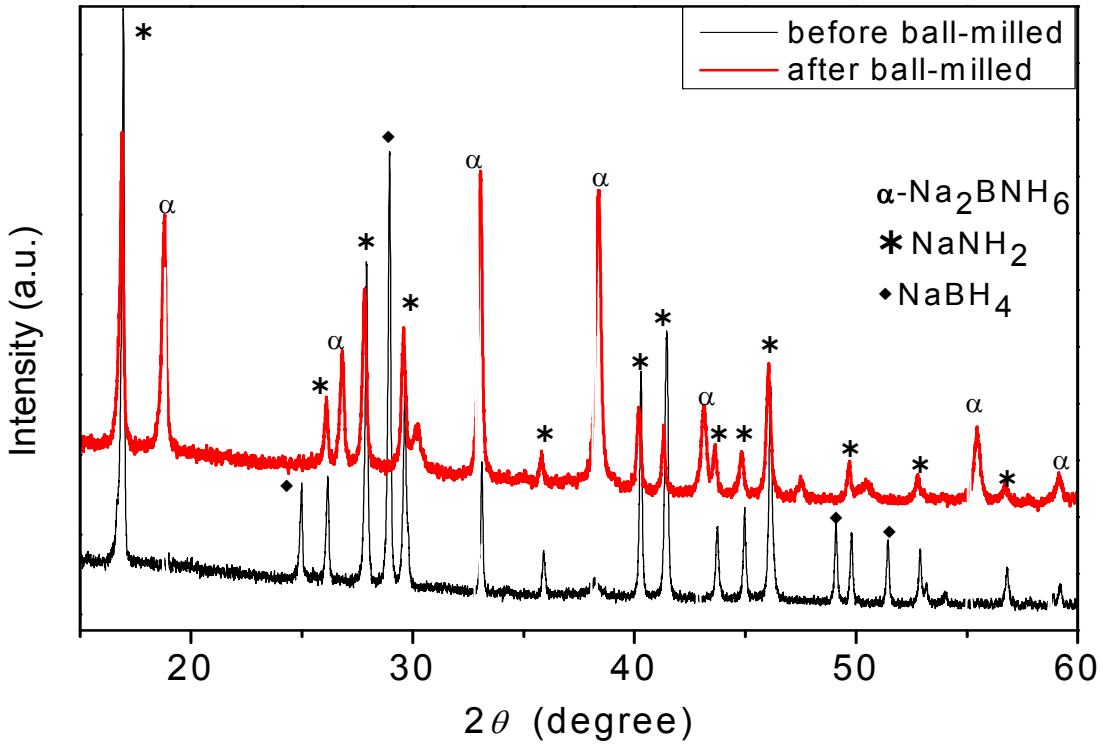

Figure 3.1: XRD diagram of $NaNH_2$-$NaBH_4$ (2:1 molar ratio) before and after ball-milling 4.5 hours with 1000 rpm.

The hydrogen release temperature of α-Na_2BNH_6 sample synthesized by ball-milling method under the optimized conditions was investigated by DTA/TG measurements. The components in the gas phase were identified by Mass spectroscopy. Fig. 3.2 depicts the thermal decomposition data of the ball-milled sample. Results of the TG and Mass spectra were combined into one graph for better visualization. As the graph shows the hydrogen release started at around 553 K [60, 61] and did not peak until ~663 K. During the dehydrogenation, NH_2, NH_3 and N_2 gases were also observed in trace amounts with respect to hydrogen in mass spectrum. The amount of released hydrogen was approximately 6.8 wt% of the total mass which was in line with the theoretical value (6.9 wt% for the 2:1 mixture).

The DTA/TG Mass Spectroscopy results of α-Na_2BNH_6 compound synthesized by the ball milling and thermal method was compared. The thermal decomposition

analysis indicates that the synthesis method does not affect the hydrogen release temperature, since hydrogen release starts in molten state. In other words, the decreased particle size (from 54 nm to 32 nm) of the sample achieved by ball-milling does not affect hydrogen release temperature of the system.

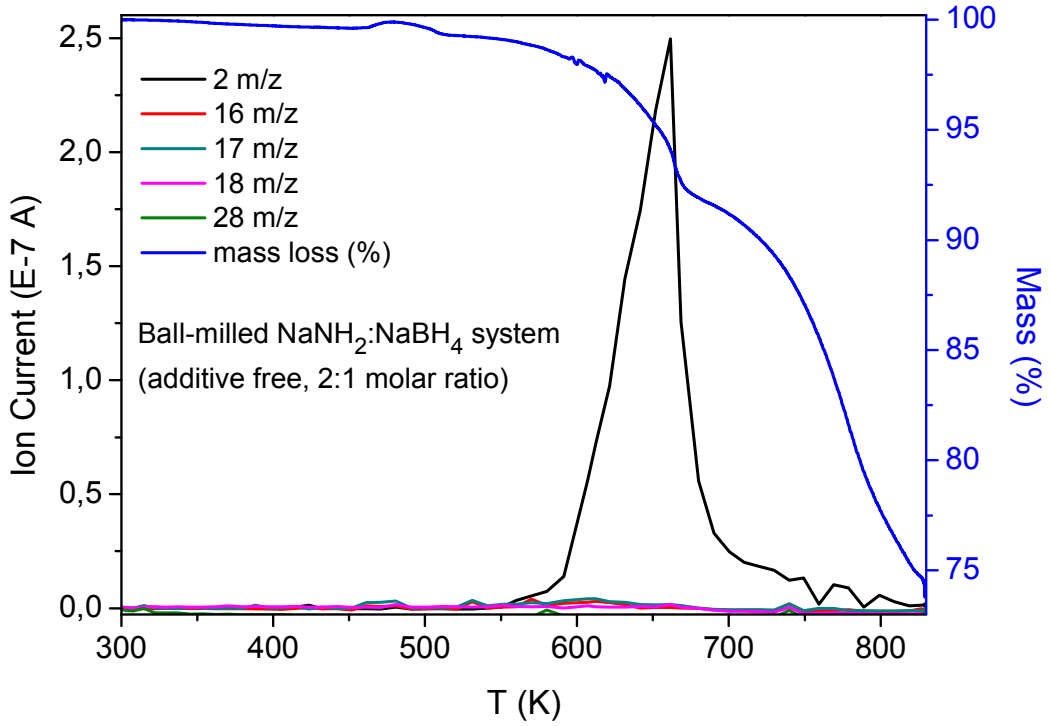

Figure 3.2: Thermal decomposition graph of α-Na_2BNH_6 synthesized by ball-milling of $NaNH_2$-$NaBH_4$ (2:1 molar ratio) mixture for 4.5 hours with 1000 rpm.

3.2 XRD Analyses of the Ball-milled $NaNH_2$-$NaBH_4$ Mixtures (molar ratio 2:1) with Additives

The $NaNH_2$-$NaBH_4$ samples were ball-milled with different additives and XRPD measurements were performed to identify the end products. In this part, we will present and discuss the XRD and DTA/TG-Mass spectroscopic results of the ball-milled $NaNH_2$-$NaBH_4$ samples with different catalysts. Powdered Pd, Pt metals, and their

chlorides; Ni, Pt/Vulcan carbon and Pd/Black Pearls®2000 were selected as catalyst based on the literature data and were expected as the most promising additives for decreasing hydrogen release temperature. The particle size of the catalysts was calculated based on XRPD investigations and compared with literature data. The detailed values are listed in Table 3.1.

Table 3.1: Calculated particle size and surface area of the additives.

Additive	Particle size (nm)	Surface area (m^2/g)
Pd	< 300	
Pt	< 600	
Ni	< 1000	
$PdCl_2$	89 ($PdCl_2$)	
$PtCl_2$	72 ($PtCl_2$)	
20 % Pt/Vulcan	3 (Pt)	82
20 % Pt/Vulcan [94]	2.2 (Pt)	128
50 % Pt/Vulcan	3 (Pt)	86
12 % Pd/Black Pearls	12 (Pd)	41
20 % Pd/Black Pearls	14 (Pd)	36
Vulcan XC-72 [94]	30	254
Black Pearls®2000 [94]	30	1475

According to XRPD results, all additive containing samples were converted to α-phase after ball-milled with the optimum parameters determined for additive free samples. Again, similar to the additive free samples $NaNH_2$ was present as the X-ray powder diffractograms shows. The powder patterns of the samples containing the metal additives (e.g. Pd, Pt and Ni) reveal only the characteristic reflections of the metals, while those of the chlorides undergo drastic changes.

Figure 3.3 is given as the characteristic XRD diffractogram of the samples with neat metal (5.3 wt% Pd) additions. In the XRD diagrams of these samples containing

Pd, Pt or Ni catalysts, no new phase formation was observed. The metal additives stayed still without any reaction after ball-milling.

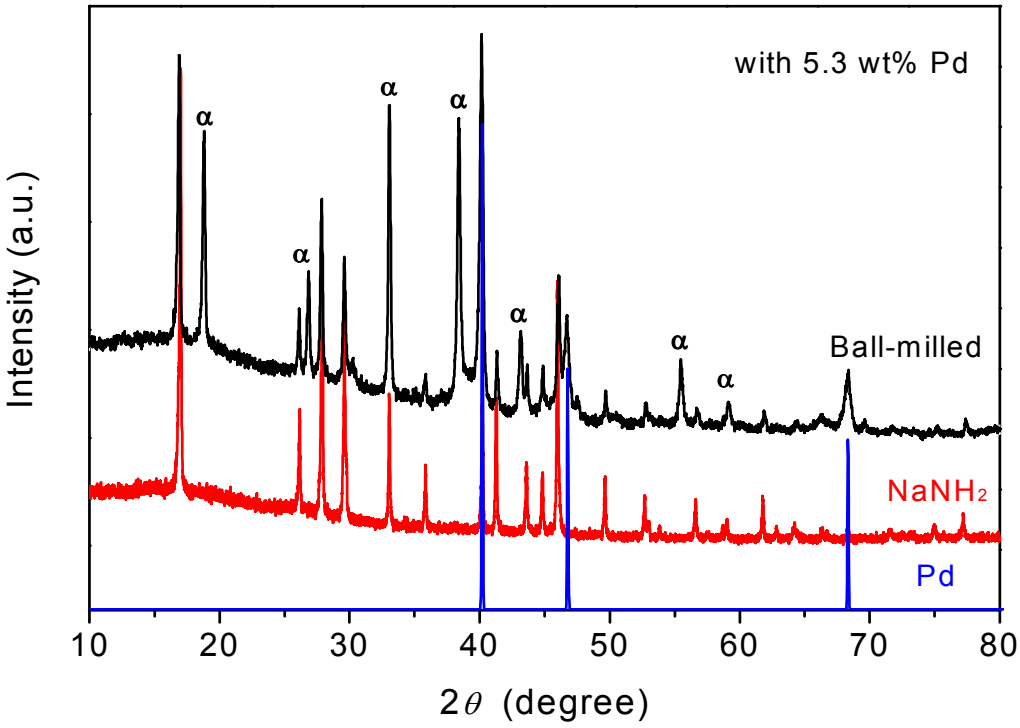

Figure 3.3: XRD diagram of ball-milled $NaNH_2$-$NaBH_4$ (2:1 molar ratio) mixture with 5.3 wt% Pd addition.

As depicted in Figure 3.4(a), the ball-milled sample containing 5.6 wt% $PdCl_2$ shows only peaks representing Pd and $PdH_{0.706}$. The result indicates that during the ball-milling, $PdCl_2$ decomposed and elemental palladium formed. The presence of $PdH_{0.706}$ indicates that small amount of Pd reacted with hydrogen from Na_2BNH_6 or $NaNH_2$ while the rest of the Pd remained unreacted. In addition, there are some extra peaks labeled as "?" which could not be indexed to any of the known phases, yet.

The sample with 5.4 wt% $PtCl_2$ shows the similar behavior to the $PdCl_2$ added sample. The XRD reflections corresponding to $PtCl_2$ were completely disappeared after ball-milling. Most probably, $PtCl_2$ decomposed during the ball-milling and a new phase

or phases formed. However, the observed patterns do not match with any of the known Pt compounds.

A possible explanation for this phenomenon is, that instead of $PdCl_2$ and $PtCl_2$ the neat metals are more favored because their halides – i.e. Pd^{2+} and Pt^{2+} - are easily reduced during ball-milling in presence of $NaBH_4$, yielding:

$$Pd^{2+} + 2BH_4^- \rightarrow Pd_{(s)} + H_{2(g)} + 2BH_{3(g)} \qquad \text{(eq. 3.2)}$$

This means the halides initialize the partial hydrogen release of the α-phase already through ball-milling. Part of the hydrogen released reacts with the reduced Pd metal to form $PdH_{0.706}$. In the case of $PtCl_2$, the XRD results indicate also a formation of a new phase which does not match with patterns of any known Pt hydride.

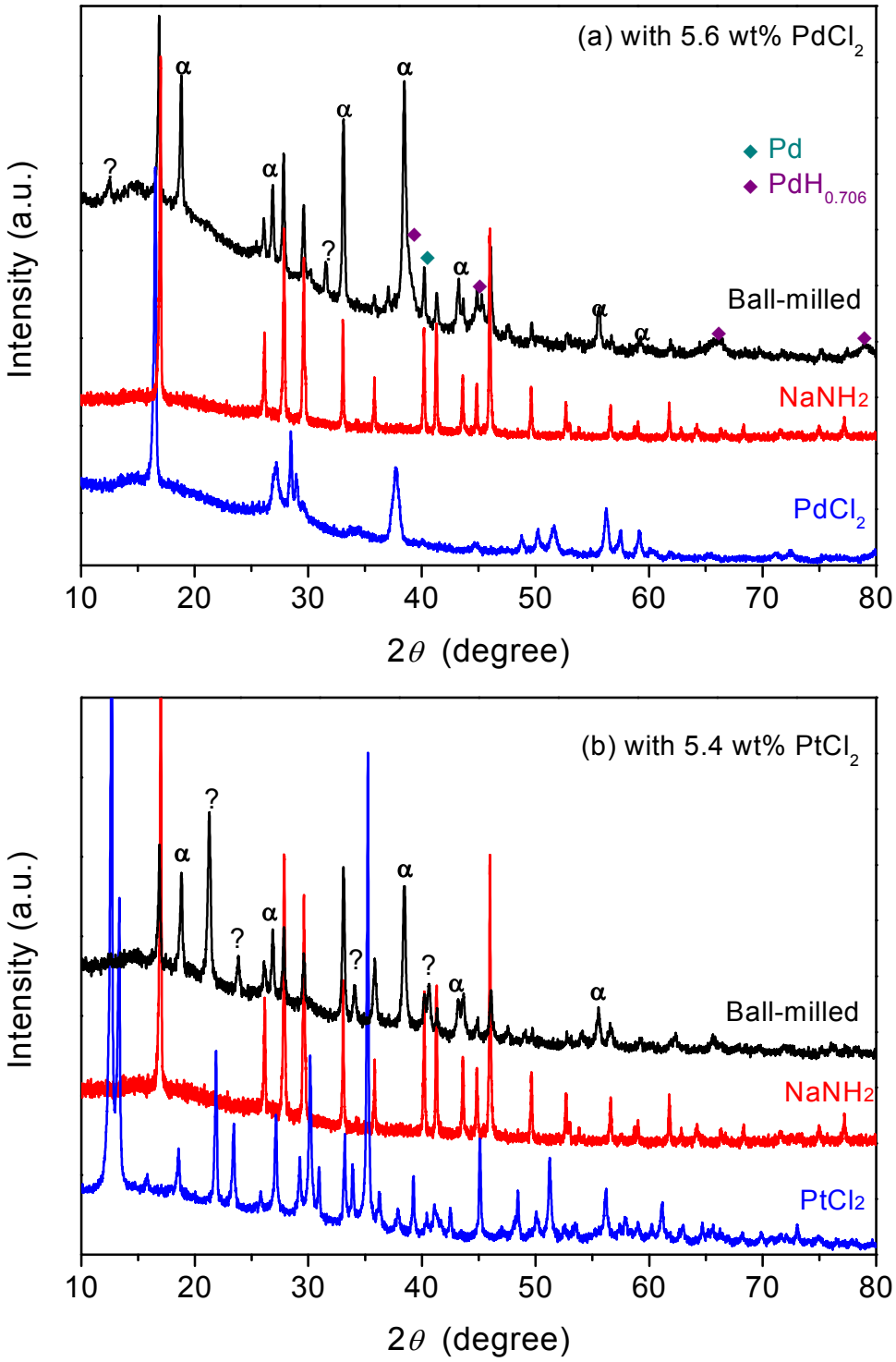

Figure 3.4: XRD diagram of ball-milled $NaNH_2$-$NaBH_4$ (2:1 molar ratio) mixture with; (a) 5.6 wt% $PdCl_2$ and (b) 5.4 wt% $PtCl_2$ additions.

The XRD diagram of 5.3 wt% Pt/Vulcan carbon (Pt content 50 wt%) sample have very broad peaks at $2\theta = 40.080$, 46.955 and 68.73 which are referred to the very small particle size of Pt metal (~ 3 nm) on the Vulcan carbon (Figure 3.5). After ball-milling, the characteristic reflections of Pt and $NaNH_2$ were overlapped at these 2θ values. The XRD diffractogram of Pd/Black Pearls®2000 samples (Pd content 20 wt%) are similar to those of 5.3 wt% Pt/Vulcan carbon added specimens.

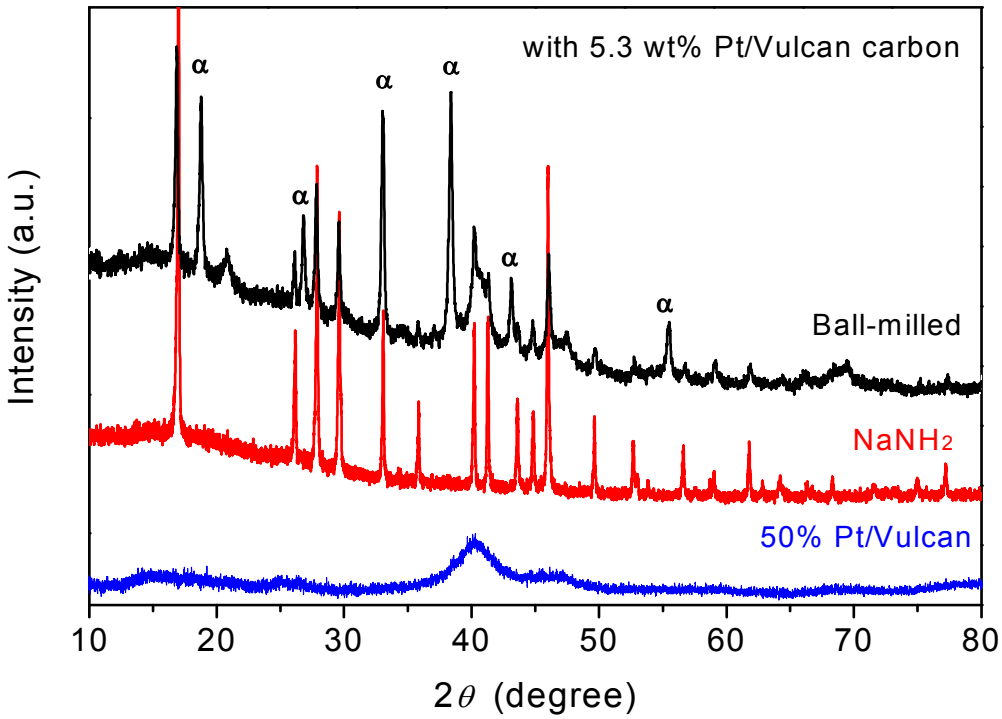

Figure 3.5: XRD diagram of ball-milled $NaNH_2$-$NaBH_4$ (2:1 molar ratio) mixture with 5.3 wt% Pt/Vulcan carbon addition.

3.3 Thermal Decomposition Analyses of the Samples with Additives

In this study, several other transition metals and their chlorides were used for the kinetic destabilization of the 2:1 $NaNH_2$-$NaBH_4$ system, but only a few of them achieved to decrease the hydrogen release temperature.

Ti and $TiCl_3$ were reported as breakthrough additives for decreasing dehydrogenation temperature and the reversibility of $NaAlH_4$ [20, 21]. These substances were also studied for their catalytic effect, but showed no noticeable influence on the kinetic destabilization of $NaNH_2$-$NaBH_4$ system. The results are depicted in Appendix C.

The thermal decomposition analysis showed that Pd, Pt, Ni, $PdCl_2$, and $PtCl_2$ successfully decreased the dehydrogenation temperature with 20-60 K. These results are in line with the reported literature data [78, 88-93]. The effects of these additives on the hydrogen release temperature are given in Figure 3.6 and 3.8.

From the mass spectroscopy measurement, trace amount of NH_3, NH_2 and N_2 gas release were observed in the presence of Pd and Pt catalysts. When their chloride salts and Ni were used as a catalyst, the amount of NH_2, NH_3 and N_2 gases increased and H_2O signal was also detected. Probably, they catalyze the decomposition of nitrogen containing compounds. The increase in the amount of water and ammonia during dehydrogenation is most probably related to short contact with air during the sample transfer into DTA/TG instrument. Most likely, the Ni and the fine particles of the $PtCl_2$ and $PdCl_2$ can adsorb higher amount from the components of the air.

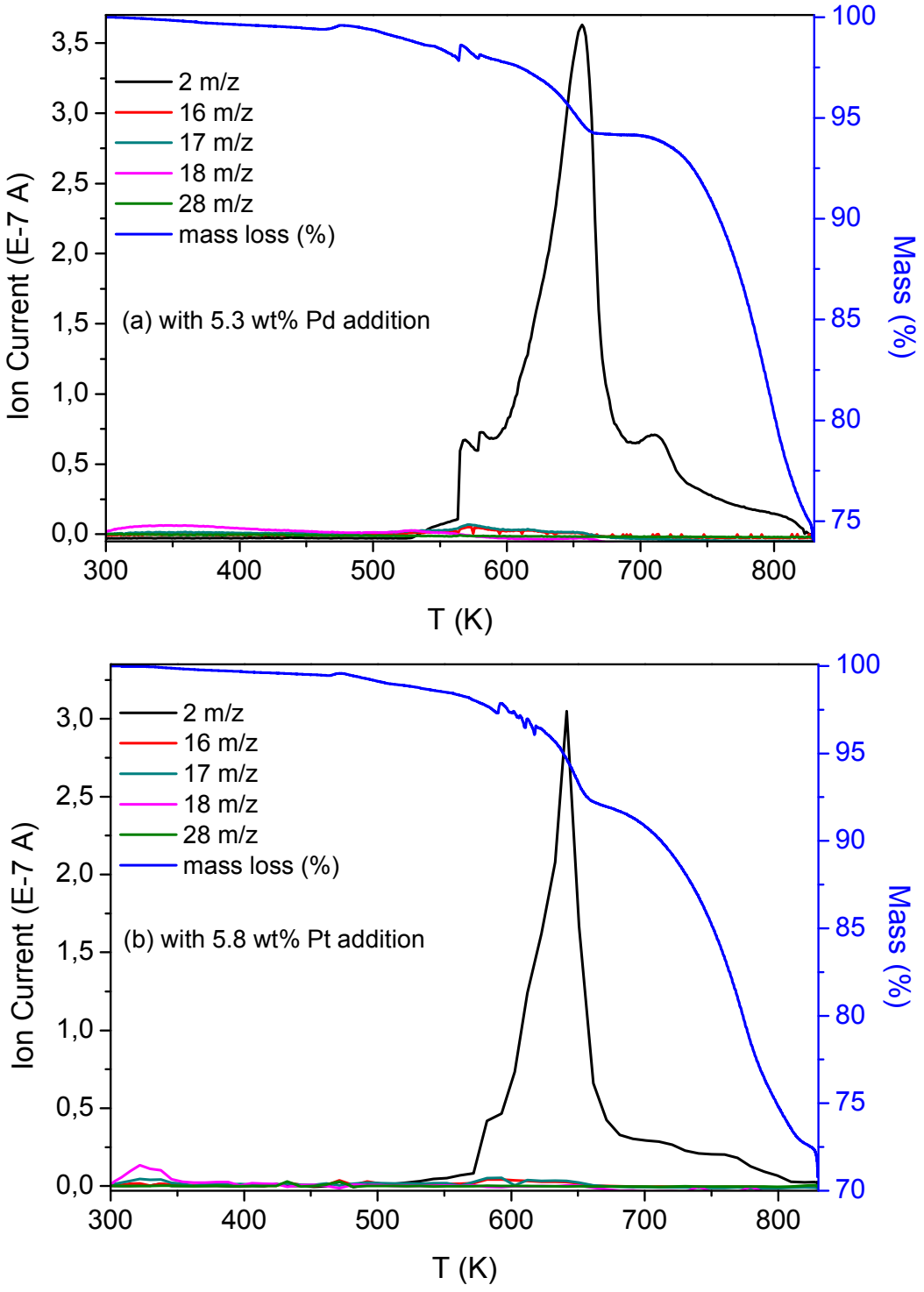

Figure 3.6: Thermal decomposition graph of ball-milled $NaNH_2$-$NaBH_4$ (2:1 molar ratio) mixture (a) 5.3 wt% Pd, (b) 5.8 wt% Pt additions.

For Pd, Pt, $PdCl_2$, $PtCl_2$ and Pt/Vulcan carbon additives, we prepared sample series with different weight percentages in order to show the effect of additive concentration on hydrogen release temperature and optimize the reaction conditions. However, we could not find a general trend for the additive amount as shown in Figure 3.7. For instance, when the amount of Pd increases, the hydrogen release temperature decreases however for $PdCl_2$ and $PtCl_2$ additions, further additions cause increase in the onset temperature.

Samples were prepared via ball-milling, which is a complex stochastic process, and the number of variables involved is great. Although each sample was prepared under the same conditions, the starting size of the additives, their hardness, weight of grinding medium, and ball-to-powder weight ratio, and many other factors might affect the particle dispersion in the system, consequently the efficiency of the additive.

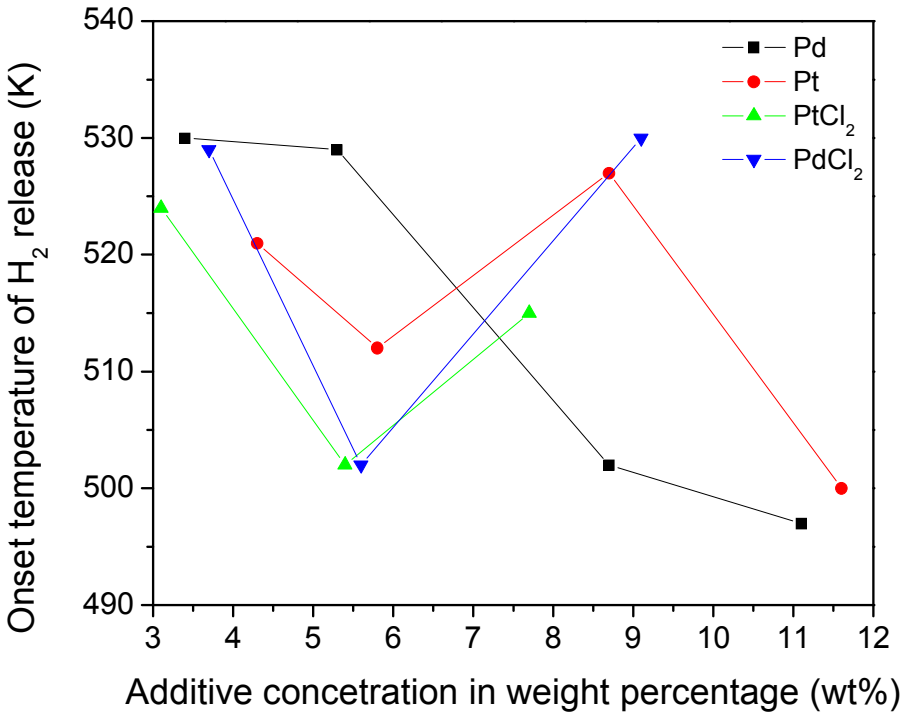

Figure 3.7: Hydrogen release onset temperatures of samples which were prepared with Pd, Pt, $PdCl_2$ and $PtCl_2$ additions at different weight percentages.

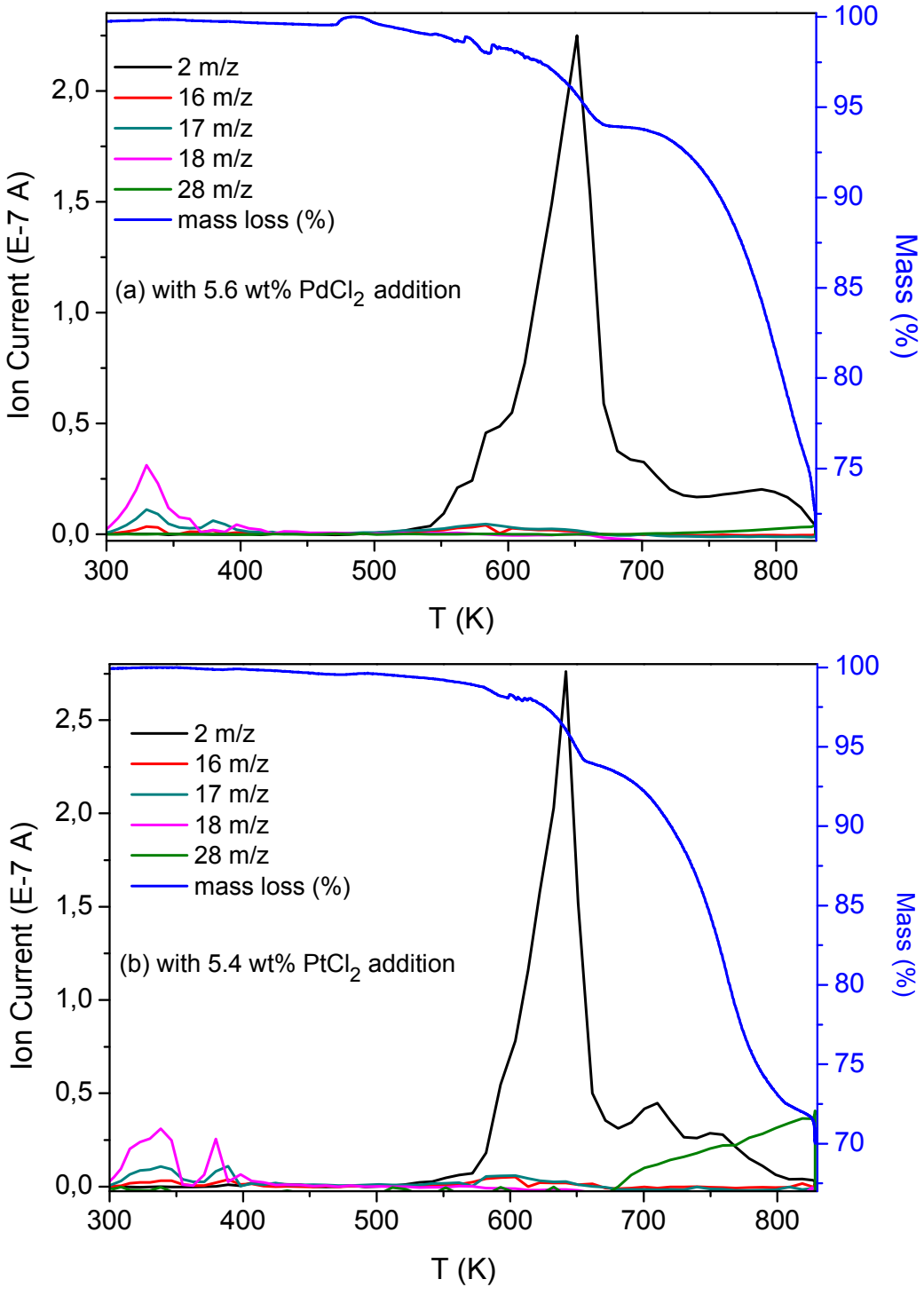

Figure 3.8: Thermal decomposition graph of ball-milled $NaNH_2$-$NaBH_4$ (2:1 molar ratio) mixture (a) 5.3 wt% $PdCl_2$, and (b) 5.8 wt% $PtCl_2$ additions.

It is well-known that the efficiency of the catalyst depends critically on how well it is dispersed in the system and on its surface area. Because of the small particle size and large surface area of Pt or Pd supported carbon black (CB) materials (Table 3.1), they were chosen as appropriate additives for decreasing the temperature of dehydrogenation.

As shown in Figure 3.9, the most remarkable improvement for the hydrogen release temperature was observed when Pt/Vulcan carbon and Pd/Black Pearls®2000 were used. With the addition of 5.6 wt% Pt/Vulcan carbon (50 wt% Pt) hydrogen release temperature decreased from ~553 to 404 K. A marked shift to 392 K has also been observed for the addition of 2.9 wt% Pd/Black Pearls (12 wt% Pd). Nevertheless, these additives did not affect the hydrogen peak temperature (T_{max}) at which the maximum amount of hydrogen release was registered. They only shifted down the starting temperature of the dehydrogenation process. The results for Pt/Vulcan carbon and Pd/Black Pearl system is summarized in Table 3.2.

The effect of Pt/Vulcan carbon addition was different than the other catalysts. When Pt/Vulcan carbon was used, the release of hydrogen spread in a wide temperature range while the mass spectra revealed two characteristic peaks instead of one. This speaks for a two step reaction which is not studied further.

In order to investigate the effects of carbon black, pure Vulcan XC-72 and Black Pearls®2000 were added to $NaNH_2$-NaBH4 system. Different from the Pd and Pt metals, the addition of supporting carbon increases the hydrogen release temperature to ~ 570 K (Table 3.2).

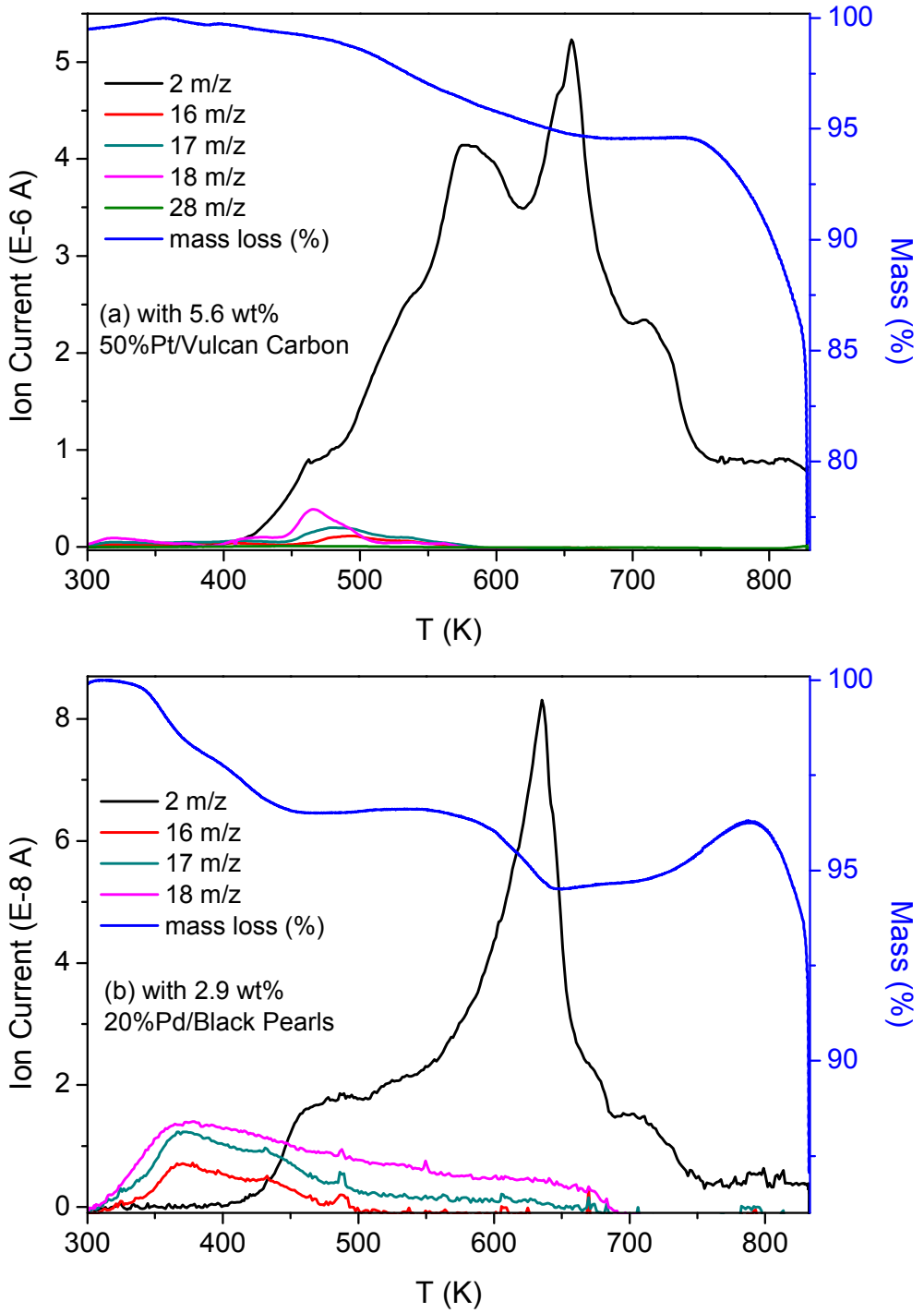

Figure 3.9: Thermal decomposition graphs of the ball-milled $NaNH_2$-$NaBH_4$ (2:1 molar ratio) mixture; (a) 5.6 wt% Pt/Vulcan carbon and (b) 2.9 wt% Pd/Black Pearls®2000 additions.

To study the effect of concentration and the surface area of the used additives, Pt/Vulcan carbon and Pd/Black Pearls with different weight percentage were prepared. The particle size and surface area of the commercially available 20 and 50 wt% Pt/Vulcan were reported as 2.2 nm, 128 m^2/g, and 3.0 nm, 86 m^2/g, respectively [94]. However, the XRD results proved that the particle size and surface area of both additives are similar (3 nm, 86m^2/g). The samples with 2.1 wt% (50 wt% Pt/Vulcan carbon) and 2.0 wt% (20 wt% Pt/Vulcan carbon) - having almost the same weight percentage of the catalyst (Pt) were compared. Figure 3.10 shows the effect of metal catalyst content on the onset and maximum hydrogen release temperature for 20 wt% and 50 wt% Pt containing Vulcan carbon. It was found that the specimens with 20 wt% Pt/Vulcan carbon are less effective in decreasing the starting and peak temperature of dehydrogenation than those with 50 wt% Pt/Vulcan carbon because of the higher amount of carbon black content in it. Figure 3.10 also indicates that with increasing metal content the first peak of maximum hydrogen release was successfully decreased by ~100 K. While the starting temperature of hydrogen release suddenly decreases by ~150 K in the presence of Pt metal but further addition of the metal (more than 2 wt% Pt) does not decrease further this temperature.

For Pd/Black Pearls added samples where the Pd content was 12 and 20 wt%, a slight but a significant change in the dehydrogenation temperature was measured.

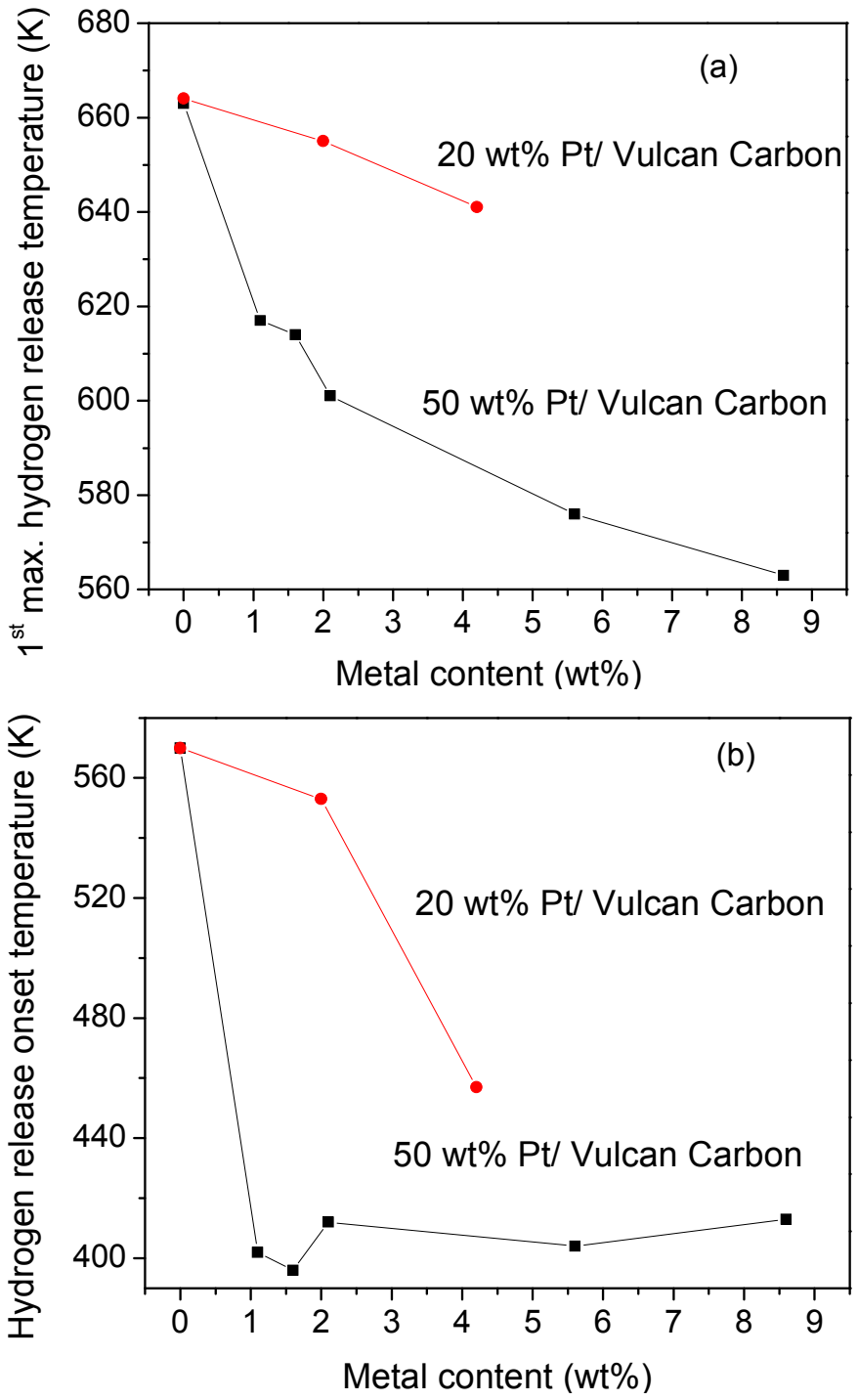

Figure 3.10: The effect of metal catalyst content on the a) maximum (first peak) and b) onset hydrogen release temperature for 20 wt% and 50 wt% Pt containing Vulcan carbon.

Table 3.2: Hydrogen release temperatures of samples prepared with Pt/Vulcan carbon, Pd/Black Pearls®2000, Vulcan carbon XC-72, and Black Pearls®2000 additions at different weight percentages.

Additive	Weight percentage of metal (%)	Hydrogen release onset temperature (K)	Maximum hydrogen release temperature (K)	End of hydrogen release temperature (K)
Additive free	-	553	663	789
50 % Pt/Vulcan	1.1	402	617/722	834
50 % Pt/Vulcan	1.6	396	614/691	835
50 % Pt/Vulcan	2.1	412	601/650	838
50 % Pt/Vulcan	5.6	404	576/655	830
50 % Pt/Vulcan	8.6	413	563/606/647	830
20 % Pt/Vulcan	2.0	553	655	834
20 % Pt/Vulcan	4.2	457	641	835
Vulcan carbon	5.3*	563	665	831
Vulcan carbon	7.1*	588	665	834
20 % Pd/Black Pearls 2000	2.9	405	635	833
12 % Pd/Black Pearls 2000	2.9	392	630	835
Black Pearls 2000	3.3*	562	664	834
Black Pearls 2000	5.4*	570	656	835

* The weight percentage of carbon blacks without metal supported.

3.4 XRD Analyses of 2:1 $NaNH_2$-$NaBH_4$ Mixture with Additives after Dehydrogenation

The final product after the dehydrogenation is important to understand and design the rehydrogenation and recycling process. In order to determine the end products of samples with additives, XRPD measurements were carried out after sample dehydrogenation at target temperature for 2 hours.

The XRD analysis showed that the end product of $NaNH_2$-$NaBH_4$ (2:1 molar ratio) mixture after complete hydrogen release is Na_3BN_2 and Na.

The XRD diffractograms of samples with metal additives (Pd, Pt, and Ni) are given in Figure 3.11. After dehydrogenation, no Pd metal or Pd-containing phases are detectable in the sample with 5.3 wt% Pd addition (Figure 3.11a). Similar observations have been reported for the related $LiNH_2$-$LiBH_4$ system. The lack of Pd and new foreign reflections in the powder diagram in Fig. 3.11a indicates that the Pd metal undergoes a chemical reaction during the decomposition process and the phases formed are amorphous. Unlike Pd, Pt and Ni metals remain unreacted and can be detected in the XRD (Figure 3.11b) by their characteristic peaks.

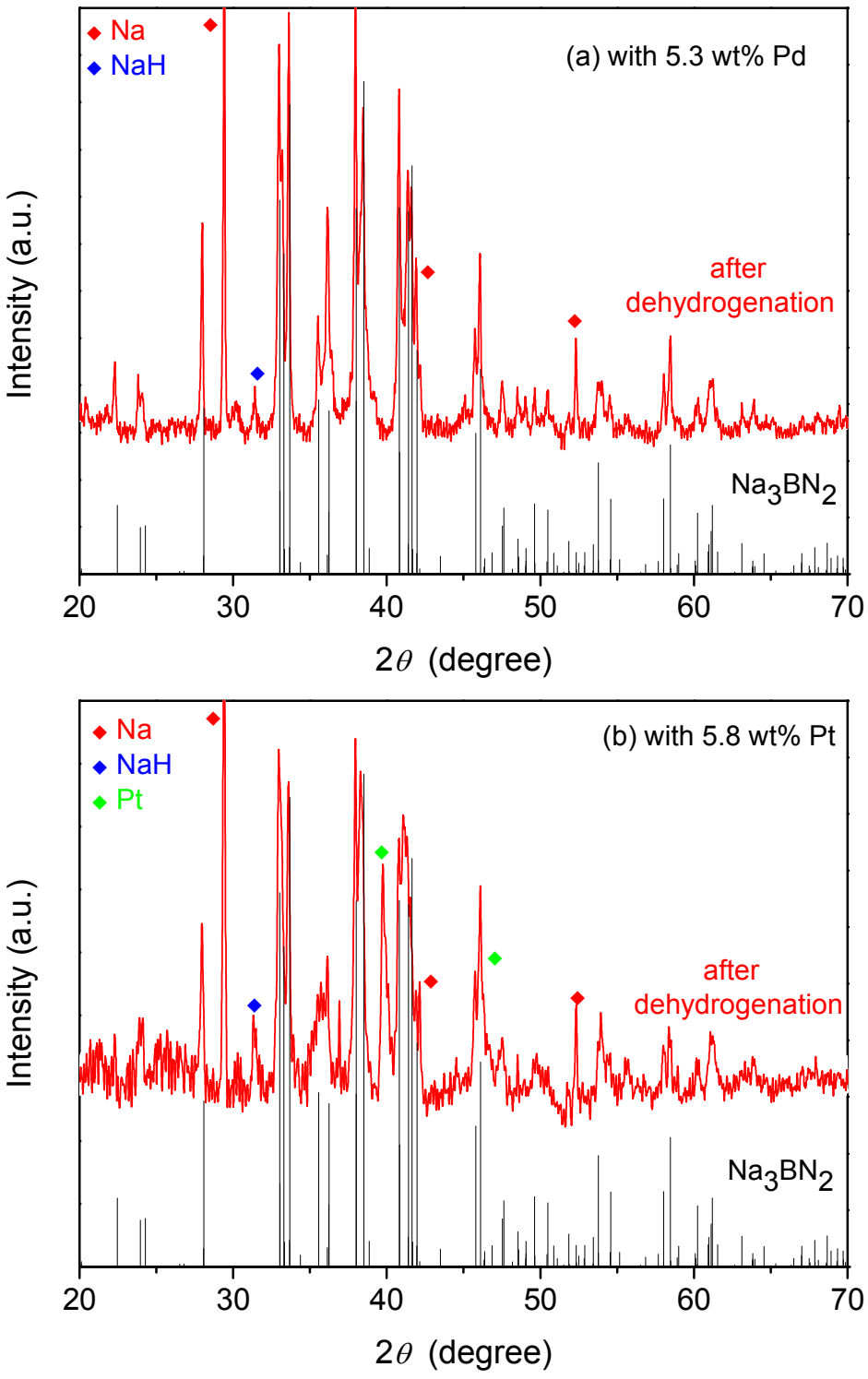

Figure 3.11: XRD diagram of ball-milled $NaNH_2$-$NaBH_4$ (2:1 molar ratio) mixture with; (a) 5.3 wt% Pd, and (b) 5.8 wt% Pt additions after dehydrogenation.

As mentioned before, the samples with $PdCl_2$ addition were reduced in the presence of $NaBH_4$ already to Pd and $PdH_{0.706}$ during the ball-milling. Because of this reason the XRD result of the sample with $PdCl_2$ additive is very similar with that of Pd metal additive. Again, there is no indication of Pd or any Pd-containing phases in the XRD diagram after the dehydrogenation (Figure 3.12a).

Fig. 3.12b shows XRD of the $PtCl_2$ added sample after the decomposition process. After ball-milling of the sample containing $PtCl_2$, the formation of a new, -probably - Pt-containing unknown phase was observed- , which decomposed during the heating process and yielded Pt metal. Chemical analysis of the unknown phase showed a positive test on chloride anions. That means after decomposition of the samples with Pt and Pd chloride additions, chloride remains in the system and does not form HCl. Indeed, the mass spectra showed no increase for 36 amu which is characteristic key fragment for HCl^+. In conclusion, both chemical analysis and mass spectroscopy results verify the absence of HCl release during dehydrogenation.

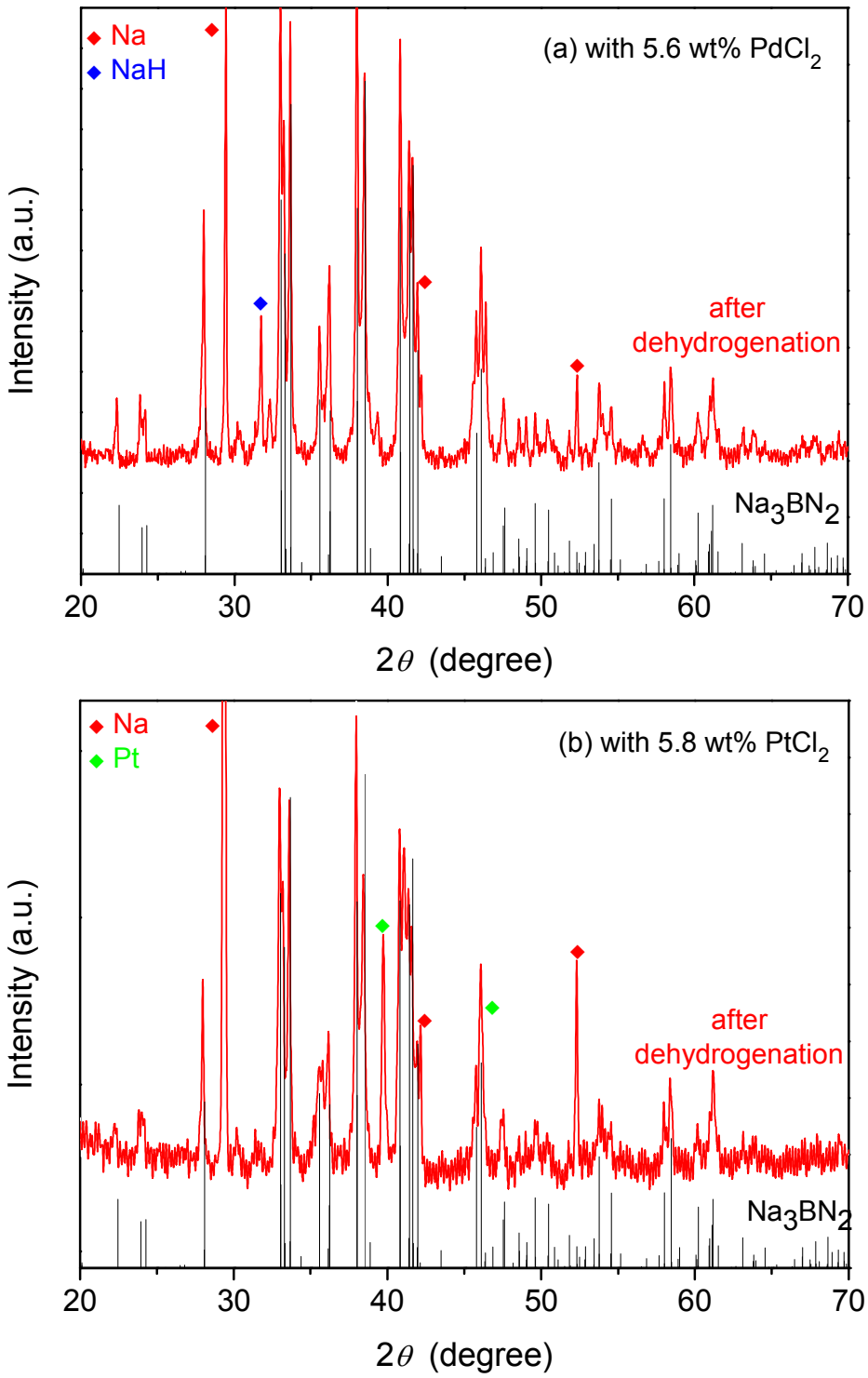

Figure 3.12: XRD diagram of ball-milled $NaNH_2$-$NaBH_4$ (2:1 molar ratio) mixture with (a) 5.6 wt% $PdCl_2$ and (b) 5.4 wt% $PtCl_2$ additions after dehydrogenation.

The XRD result of Pt/Vulcan carbon added sample after the complete hydrogen release can be seen in Figure 3.13. Beside the intense Pt reflections a broad peak was observed at 2θ = 43.69, which could not be identified, yet. In our case, the agglomeration or crystal growth of the metal particles is expected to reduce the effective surface area and cause a loss of catalytic activity. The main role of the support (carbon black) is to prevent recrystallization of metal particles which usually proceeds via sintering [78]. As observed, catalysts supported with carbon black are more effective than using neat metals as catalyst.

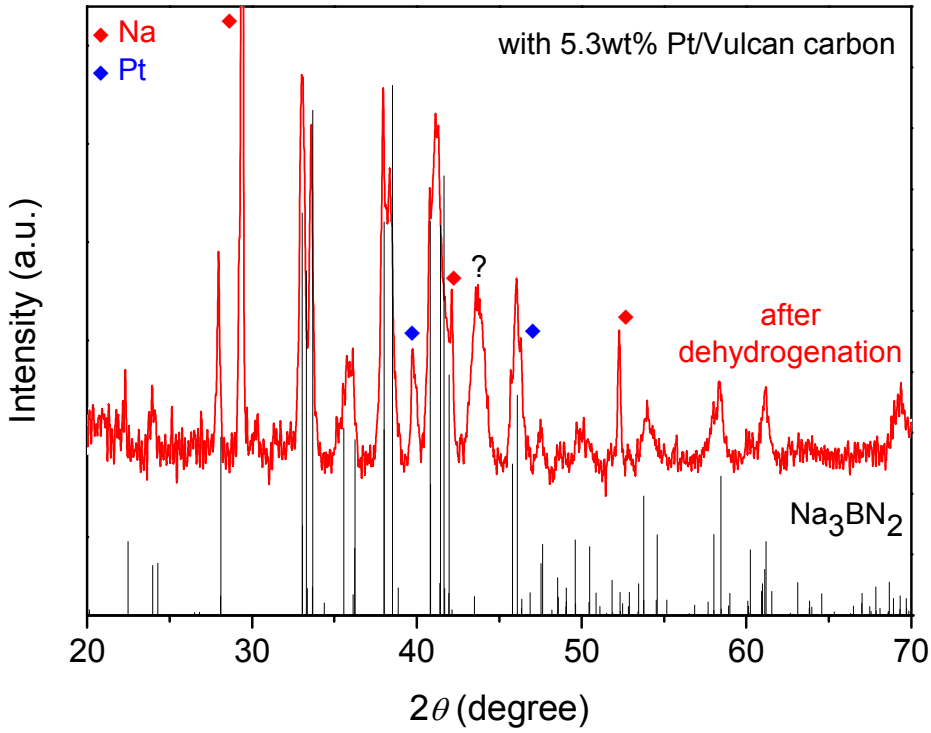

Figure 3.13: XRD diagram of ball-milled $NaNH_2$-$NaBH_4$ (2:1 molar ratio) mixture with 5.3 wt% Pt/Vulcan carbon addition after dehydrogenation.

As summary, the components of the ball-milled samples with additives before and after dehydrogenation are given in the Table 3.3. The reason for the presence of metallic Na in the final product is the thermal decomposition of Na_3BN_2 to unstable

Na_3N and amorphous BN at elevated temperatures. Na_3N is only intermediate decomposing above 360 K and releases N_2 and elemental Na is formed [95]:

$$Na_3N_{(s)} \rightarrow 3Na_{(s)} + 1/2N_{2(g)} \qquad \text{(eq. 3.3)}$$

The further investigations showed that between 2:1 – 3:1 molar ratio of $NaNH_2$:$NaBH_4$, the main product is still the phase Na_3BN_2 accompanied by small traces of metallic sodium. The latter disappears completely in the samples with a $NaNH_2$ – $NaBH_4$ ratio > 3:1.

Table 3.3: The compositions of the ball-milled samples with additives before and after dehydrogenation.

Condition	**Without additive**	**5.3 wt% Pd**	**5.8 wt% Pt**	**5.6 wt% $PdCl_2$**	**5.4 wt% $PtCl_2$**	**5.6 wt% Pt/Vulcan**
After ball-milling	α $NaNH_2$	α $NaNH_2$ Pd	α $NaNH_2$ Pt	α $NaNH_2$ Pd $PdH_{0.706}$?	α $NaNH_2$?	α $NaNH_2$ Pt/Vulcan
After dehydrogenation	Na_3BN_2 Na	Na_3BN_2 Na NaH	Na_3BN_2 Na NaH Pt	Na_3BN_2 Na NaH	Na_3BN_2 Na Pt	Na_3BN_2 Na Pt ?

3.5 Hydrogen Uptake Experiments of Additive Free and 5.6 wt% Pt/Vulcan Carbon Containing Na_3BN_2

First, the rehydrogenation experiments of Na_3BN_2 without additive and Na_3BN_2 with 5.6wt% Pt/Vulcan carbon samples were performed with Roth high-pressure

laboratory autoclave (Model II), which is designed for max. 200 bar working pressure and maximum 573 K temperature. The experiments with this equipment were conducted with the pressure range between 85-170 bars H_2 load and temperature range 363-423 K for 10 hours. However, under these conditions no change was observed in the XRD diagram of both two samples, Na_3BN_2 without additive and Na_3BN_2 with 5.6 wt% Pt/Vulcan carbon.

The same experiments were carried on with another autoclave system in Max Planck Institute Chemical Physics of Solids, Dresden. With the new autoclave system, Na_3BN_2 was exposed to 400 bar H_2 gas loading at 473 K for 10 hours. As shown in XRD diagram, only NaH formation was observed after rehydrogenation of Na_3BN_2 without additive (Figure 3.14). The formation of NaH might have two reasons. First of all, synthesized Na_3BN_2 already contains small amount of elemental Na. The characteristic reflections of Na at $2\theta = 29.55^o$ and 52.23^o in the XRD diagram of Na_3BN_2 (before rehydrogenation) indicate the presence of Na. Under H_2 loading, elemental Na in Na_3BN_2 can form NaH. Still, after rehydrogenation the same reflections characteristic for elemental sodium was observed. This means that there can be another reason for the NaH formation. We hypothesize that Na_3BN_2 reacts with hydrogen under these experiment conditions and gives the following reaction. Due to the technical difficulties of the experimental set up, we cannot verify the reaction.

$$2Na_3BN_{2(s)} + xH_{2(g)} \xrightarrow{?} 3NaH_{(s)} + BH_{3(g)} + 2NH_{3(g)} + Na_3BN_{2(s)} \quad \text{(eq.3.4)}$$

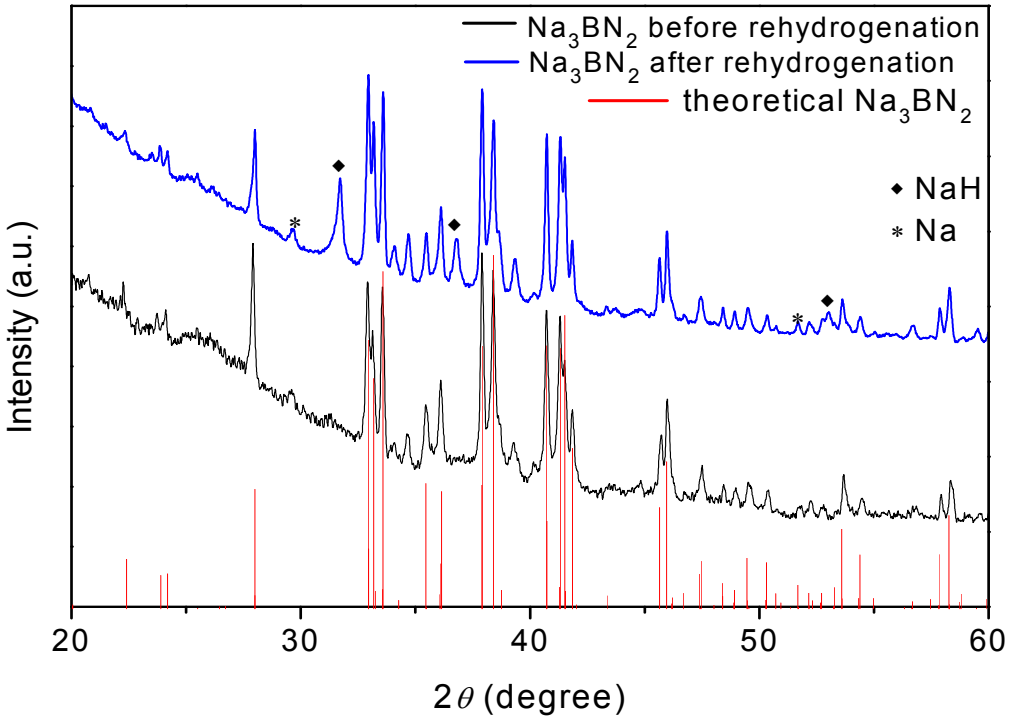

Figure 3.14: XRD diagram of synthesized Na_3BN_2 without additive before and after rehydrogenation under 400 bar H_2 at 473 K for 10 hours.

On the other hand, the hydrogen uptake experiments of Na_3BN_2 with 5.6wt% Pt/Vulcan carbon sample was performed with 350 bar H_2 load at 373 K for 10 hours. The reason for choosing the relatively low temperature is the decomposition temperature of this sample. As mentioned above, hydrogen release of $NaNH_2$-$NaBH_4$ (2:1 molar ratio) mixture with 5.6 wt% Pt/Vulcan carbon starts at 397 K.

As Figure 3.15 depicts, at the end of the rehydrogenation process for 10 hours, the formation reaction of Na_3BN_2 was not reversed by H_2 loading. But only characteristic reflections of NaH and NaOH formed in the XRD diagram. The reasons for the formation of NaH, which were mentioned for Na_3BN_2, are acceptable for this sample too. In addition, elemental sodium and moisture in the air react and cause the formation of NaOH during handling the sample. Furthermore, the unidentified broad peak at 2θ = 43.69° in the XRD diagram remained same after rehydrogenation. It is

noteworthy that the intensity of characteristic Pt metal reflection at 2θ = 39.69° decreased after hydrogenation and the peak become broader.

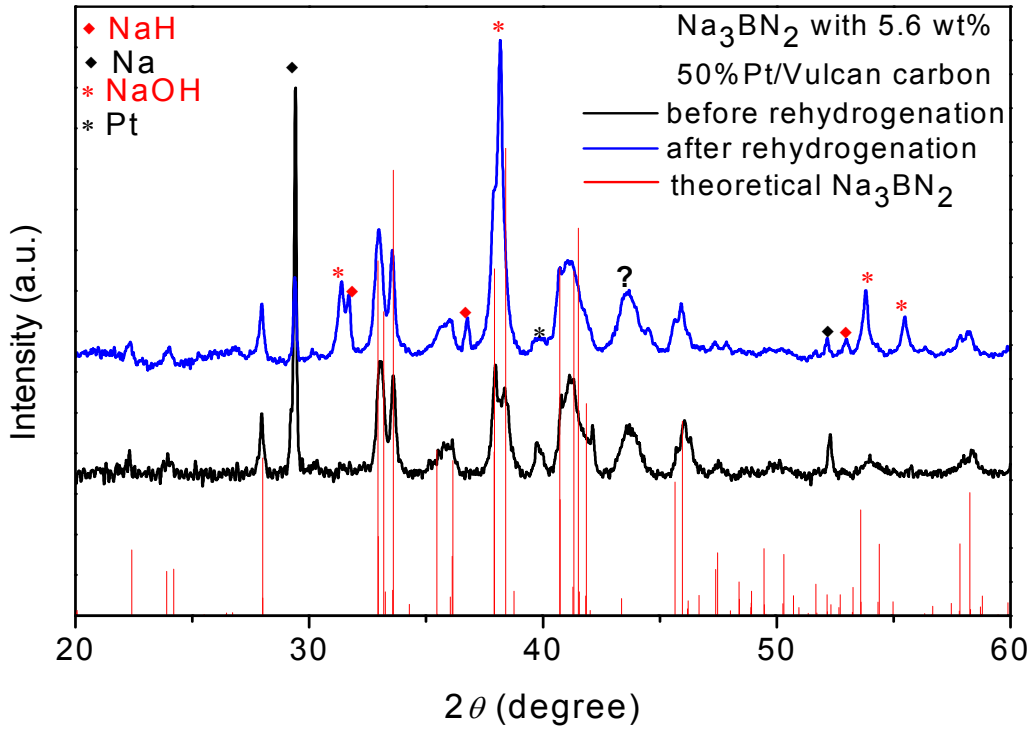

Figure 3.15: XRD diagram of Na_3BN_2 with 5.6 wt% Pt/Vulcan carbon addition before and after rehydrogenation under 350 bar H_2 at 373 K for 10 hours.

As a future investigation the hydrogenation time and temperature can be increased in order to make reversible the reaction. The experiments will be continued in the presence of other catalysts as well.

Chapter 4

4. Investigation of New Amide-Borohydride Systems for Hydrogen Storage Materials

It was recently reported that mixture of $LiNH_2$-$LiBH_4$ and $NaNH_2$-$NaBH_4$ can be possible candidates as H_2 storage material [45, 56, 60-61]. In general, the direct decomposition of amides generates mostly NH_3 and not hydrogen. However, the mixtures of borohydrides and amides have proved to release H_2 during decomposition. This can be explained with the partial charge difference of the hydrogen atoms in borohydrides ($H^{\delta -}$) and amides ($H^{\delta +}$). Most probably, the reaction between $H^{\delta-}$ and $H^{\delta+}$ leads to the formation of H_2. There are still many open questions and experimental verification of the theoretical H_2 formation is needed on other systems as well.

According to the reaction equations given below, borohydride and amide mixtures with 2:1 molar ratio are the most suitable composition to achieve the highest H_2 yield.

$$2LiNH_{2(s)} + LiBH_{4(s)} \xrightarrow{HEAT} Li_3BN_{2(s)} + 4H_{2\,(g)} \qquad \text{(eq. 4.1)}$$

$$2NaNH_{2(s)} + NaBH_{4(s)} \xrightarrow{HEAT} Na_3BN_{2(s)} + 4H_{2\,(g)} \qquad \text{(eq. 4.2)}$$

Several mixtures, such as $LiBH_4$-$NaNH_2$, $LiBH_4$-KNH_2 and $NaBH_4$-KNH_2 are not suitable for H_2 system because of their chemical nature. Based on Pearson's Hard and Soft Acid Base principle (HSAB) [96], $LiBH_4$-$NaNH_2$ mixture undergoes a metathesis reaction and results $LiNH_2$ and $NaBH_4$ mixture as final products. The model systems for further investigations were selected considering the Pearson's theory.

In order to clarify at which temperature the hydrogen is released and identify the compounds, the thermal decomposition behaviors of $LiNH_2$-$NaBH_4$, $LiNH_2$-KBH_4 and

$NaNH_2$-KBH_4 mixtures were investigated by DTA/TG, Mass Spectroscopy and XRD measurements.

4.1 Thermal Decomposition Analyses of $LiNH_2$-$NaBH_4$ Mixtures

As reported by Ichikawa *et al.*, the decomposition of $LiNH_2$ is irreversibly accompanied by release of NH_3 (eq. 4.3). The ammonia release starts at ~573 K and continues up to 773 K [39, 97].

$$2LiNH_{2(s)} \rightarrow Li_2NH_{(s)} + NH_{3(g)} \qquad \text{(eq. 4.3)}$$

The other component of the mixture, $NaBH_4$, is reported not to decompose before 673 K [52, 61], and the products of the decomposition reaction are NaH, Boron and H_2 similar to $LiBH_4$ (Figure 1.3).

Our investigations on the thermal decomposition behavior of $LiNH_2$-$NaBH_4$ (2:1 molar ratio) mixture showed that the amount of the released H_2 is significantly higher than that of NH_3 or NH_2. According to DTA/TG diagram, the decomposition starts at 621 K. The result of the thermal investigations and the related mass spectra are shown in Fig 4.1.

The appearance of double peak in DTA/TG and the corresponding H_2 mass spectrum clearly indicates that dehydrogenation occurs in two steps. In the first step, H_2 release starts at 621 K reaching its maximum at 667 K. The second hydrogen release initiates at 724 K peaking out at 753 K. The quantity of ammonia release is smaller than hydrogen, starts at ~609 and has a maximum at 638 K.

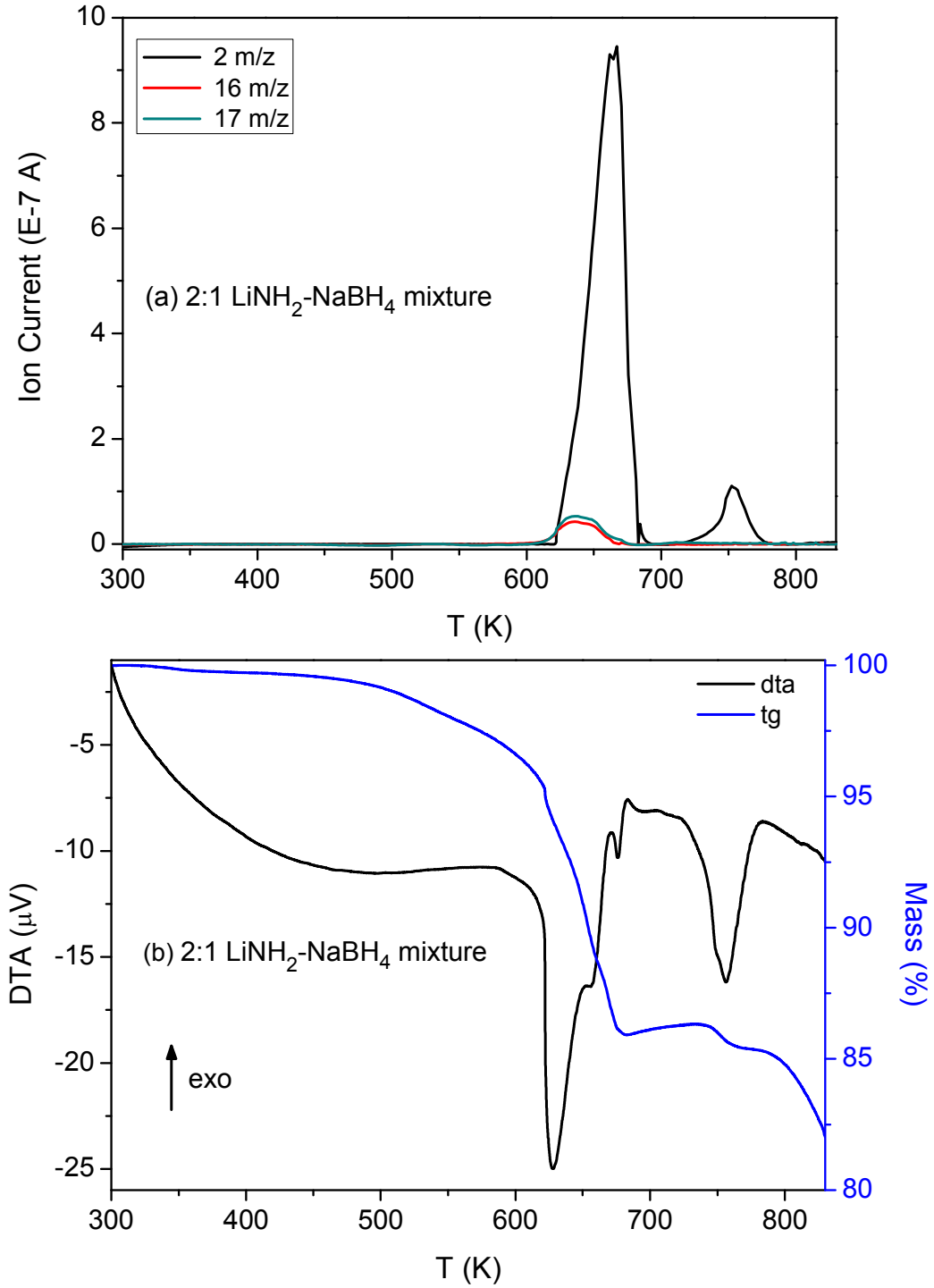

Figure 4.1: Thermal decomposition graphs of $LiNH_2$-$NaBH_4$ (2:1 molar ratio) mixture (a) Mass spectra, (b) DTA/TG graphs.

The two endothermic peaks on the DTA curve appear at 621 K and 723 K which are in line with the Mass Spectrum. The first endothermic effect corresponds to 10 % mass loss due to the H_2 release and small amount of NH_2 and NH_3 gas (Mass Spectrum). The DTA/TG and Mass Spectroscopy results point to NH_2 and NH_3 release, probably stemming from $LiNH_2$ decomposition.

The reaction of the reagents and the formation of new phases were followed by XRD method. For this purpose the reagents were heated to different temperatures under inert gas, N_2, and the resulting components were analyzed.

Figure 4.2 shows the XRD diagrams of $LiNH_2$-$NaBH_4$ (2:1 molar ratio) mixture at different temperatures. No significant changes are observed below 573 K on the XRD diffractogram.

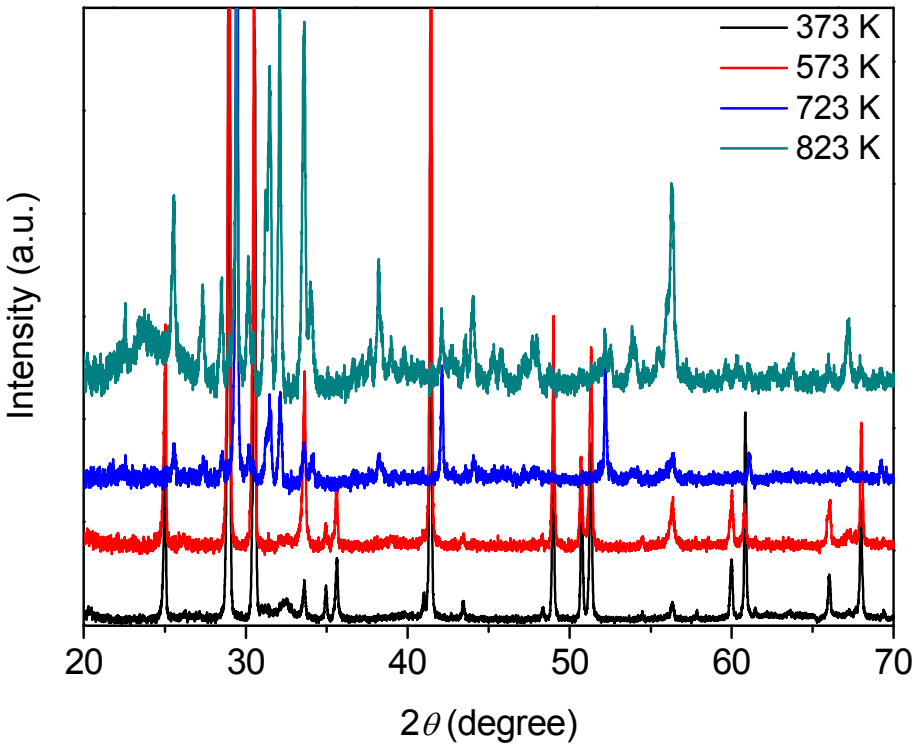

Figure 4.2: XRD diagrams of $LiNH_2$-$NaBH_4$ (2:1 molar ratio) mixture at different temperatures.

The XRD diagram of the mixture at 573 K has only characteristic reflections for $LiNH_2$ and $NaBH_4$ (Figure 4.3). At 723 K, the peaks of these components disappear and new peaks resulting from Li_3BN_2, Na and NaOH are observed instead. All results confirm that $LiNH_2$-$NaBH_4$ mixture releases hydrogen and trace amount of ammonia when Li_3BN_2 and sodium form during the heating process. The presence of NaOH after decomposition is due to reaction of elemental Na with moisture when placing the reaction tube in the glove box.

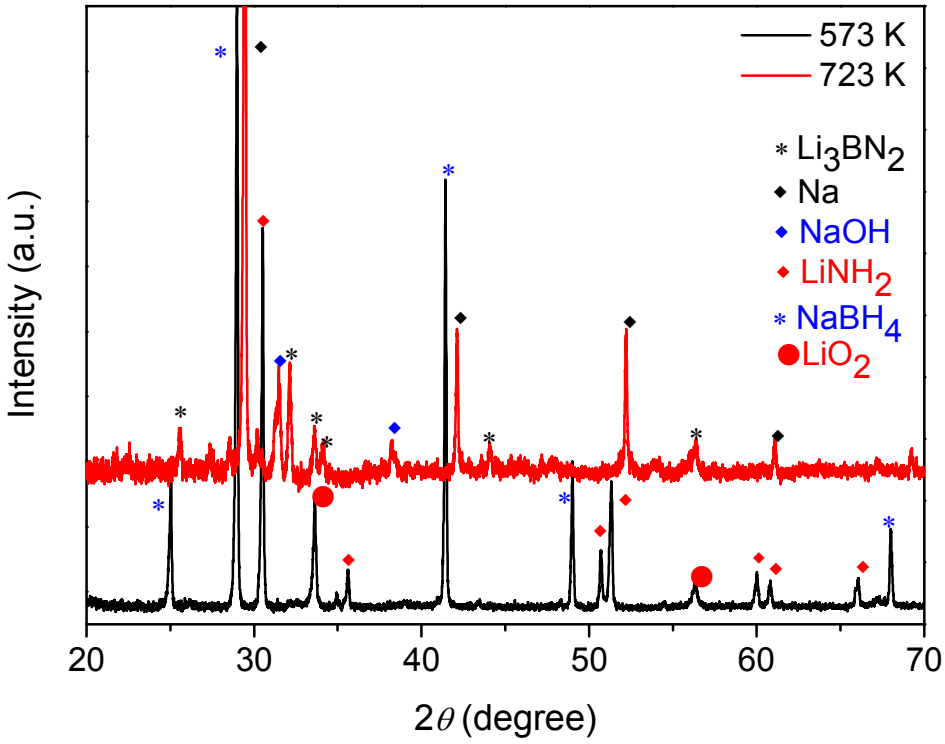

Figure 4.3: XRD diagram of $LiNH_2$-$NaBH_4$ (2:1 molar ratio) mixture at 573 K (◆ $LiNH_2$, * $NaBH_4$ and ● LiO_2) and 723 K.

It is important to note, that measurements performed for the 1:1 mixture yielded similar results. Unlike the 2:1 system, NH_3 release is much more dominant, as can be seen from the DTA/TG and Mass spectroscopic data given in Appendix B. This result confirmed that the NH_2 and NH_3 gases originated from the $LiNH_2$ decomposition. It

was also found that the XRD diagrams at 573 K and 698 K are directly comparable with those of 2:1 mixture (Appendix A).

4.2Thermal Decomposition Analyses of $LiNH_2$-KBH_4 Mixtures

During the investigations on 2:1 mixture of $LiNH_2$ and KBH_4, two endothermic peaks appeared on the DTA curve at 630 K and 800 K (Figure 4.4 b). The first endothermic effect at 630 K is assigned to the decomposition of $LiNH_2$, because the substantial amount of ammonia release is detected by Mass Spectroscopy at this temperature. No $LiNH_2$ peaks are observed in the XRD diagram at 723 K but peaks for Li_3BN_2 form (Figure 4.5).

The hydrogen release starts at 683 K and peaks out at 727 K, as observed in Mass Spectrum. Furthermore, the characteristic reflections for elemental potassium and KBH_4 in the XRD diffractogram, indicates that a small amount of KBH_4 decomposes already below 723 K (Figure 4.5).

The decomposition temperature of pure KBH_4 was reported in literature as 858 K [46, 50]. However, the main decomposition of KBH_4 in the mixture starts at approximately 800 K according to the XRD analysis. Probably, KBH_4 is decomposing in the presence of other compounds not as a pure material. The decomposition is coupled with hydrogen release as shown in DTA/TG graph and confirmed with the second hydrogen release peak which is observed at ~ 811 K in the Mass Spectrum.

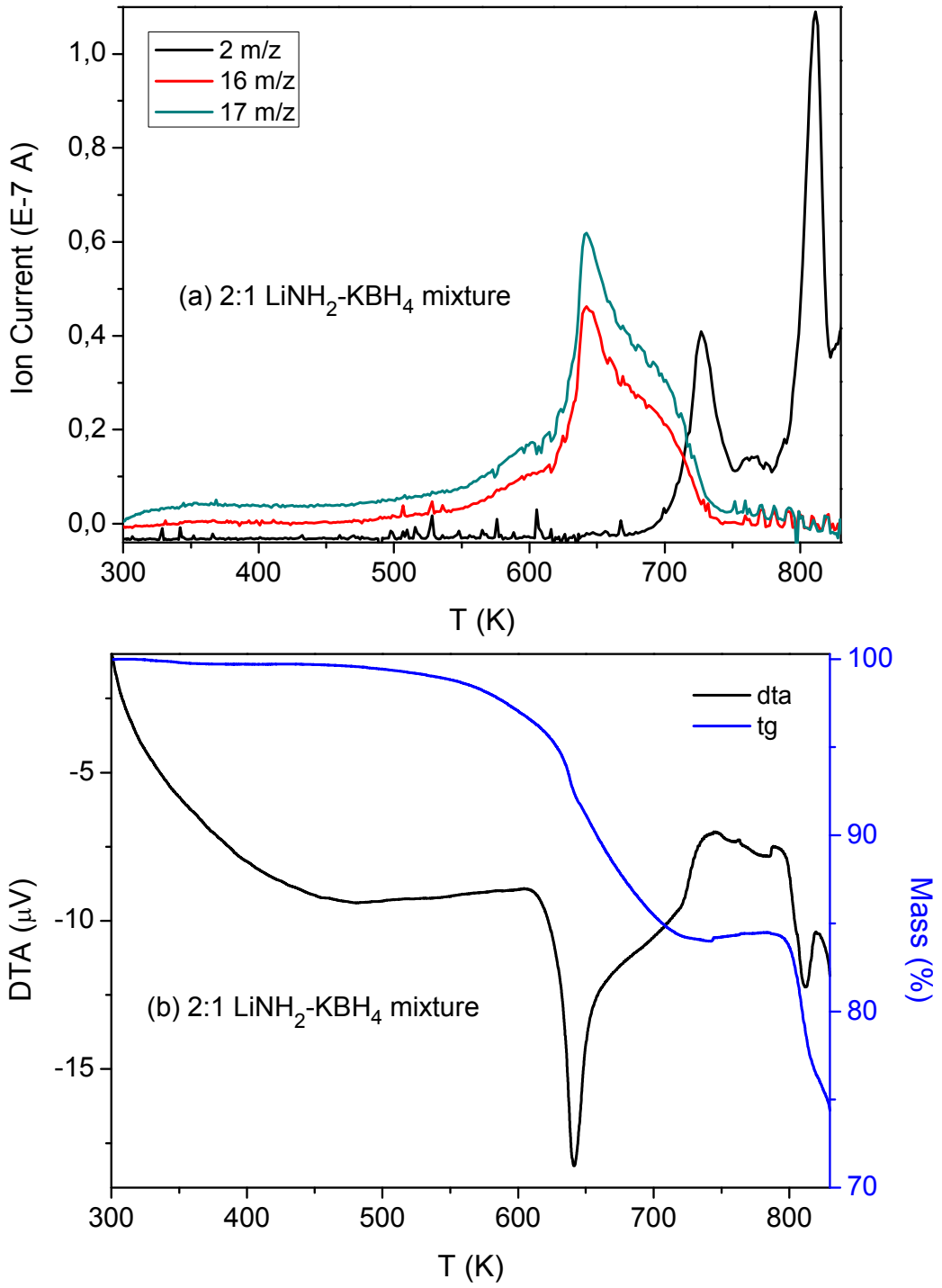

Figure 4.4: Thermal decomposition analysis of $LiNH_2$-KBH_4 (2:1 molar ratio) mixture (a) Mass spectra (b) DTA/TG graphs.

Figure 4.5 shows XRD patterns of the mixture at different temperatures. At 723 K, in addition to the peaks which are assigned to the elemental potassium, Li_3BN_2 and KBH_4, a peak at $2\theta = 31.74^o$ is observed. However no match was found for this reflection in ICDD database.

It is worth mentioning that there is a significant increase in released amount of ammonia in $LiNH_2$-KBH_4 mixture than for the previous $LiNH_2$-$NaBH_4$ system. The results for 1:1 and 2:1 mixtures are similar, except the amount of released NH_3 and H_2. The rate of NH_3/H_2 quantity for 1:1 mixture is higher than that for 2:1 molar ratio (Appendix A and B). The results are in line with $LiNH_2$-$NaBH_4$ system and similarly, NH_2 and NH_3 gases are derive from the decomposition of $LiNH_2$.

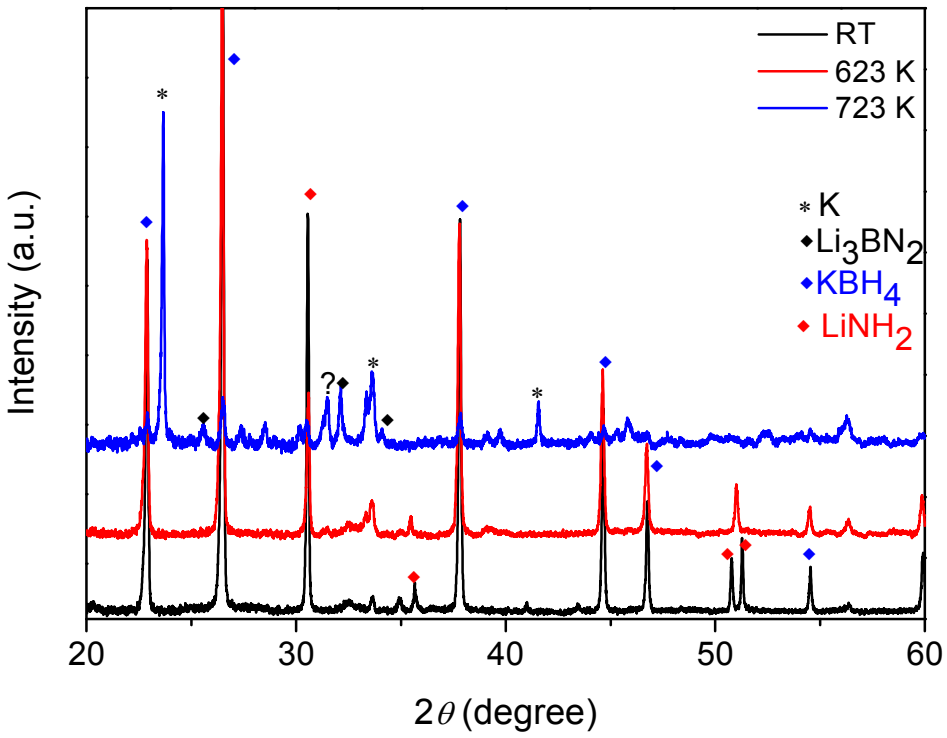

Figure 4.5: XRD diagrams of $LiNH_2$-KBH_4 (2:1 molar ratio) mixture at RT, 623 K and 723 K.

4.3 Thermal Decomposition Analyses of $NaNH_2$-KBH_4 Mixture

Previous studies showed that NH_3 release from $NaNH_2$ starts at ~553 K [39, 42, 61] while KBH_4 decomposes at 858 K [46, 50]. The thermal decomposition behavior of $NaNH_2$-KBH_4 system at 2:1 molar ratio was investigated. A novel compound formation, Na_2KBN_2, was observed while significant amount of hydrogen was emitted at approximately 673 K.

Figure 4.6b depicts the DTA/TG diagram of the $NaNH_2$-KBH_4 mixture. As seen from the DTA curve, four endothermic peaks emerge during the thermal analysis measurements. Although the first two endothermic effects (421 K and 450 K) could not be assigned precisely, one of them could be attributed to the melting point of $NaNH_2$, which is reported as 483 K [42]. As shown on Figure 4.7, the XRD diffractogram taken on the sample mixture heat treated for 2 hours at 573 K did not show any change in the phases therefore we exclude a possible reaction between the reactants. Moreover on the TG graph significant mass loss was not detected between 298 K and 623 K where this two endothermic effect is observed. Therefore these two results confirmed that one of the endothermic peaks can be connected to the melting process.

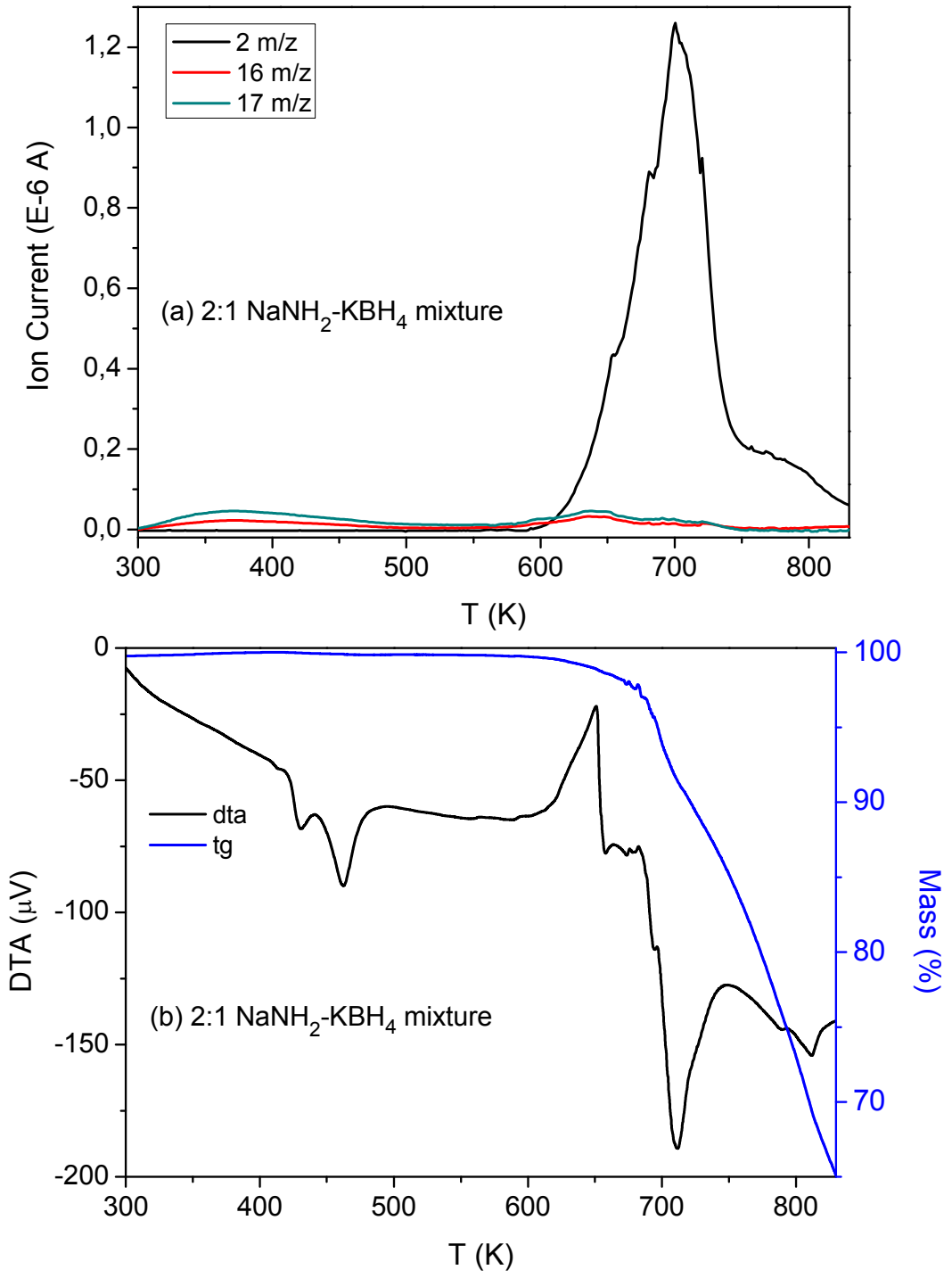

Figure 4.6: Thermal decomposition analysis of $NaNH_2$-KBH_4 (2:1 molar ratio) mixture (a) Mass spectra, (b) DTA/TG graphs.

The other two endothermic effects which are registered in the DTA/TG diagram at 651 K and 691 K are assigned to the start of dehydrogenation process of the molten mixture and its ultimate decomposition, respectively. The Mass spectrum in Figure 4.6a indicates that the hydrogen release starts slightly earlier at 596 K reaching its maximum at 700 K. The latter shows also an insignificant amount of ammonia emission. Mass loss during the hydrogen release of the $NaNH_2$-KBH_4 mixture is 9.7 % of the total mass of the mixture. However, the calculated weight percentage of hydrogen in this system is 6.11 % of the total mass. This difference in the theoretical and experimental mass loss can be explained with the loss of ammonia during the decomposition.

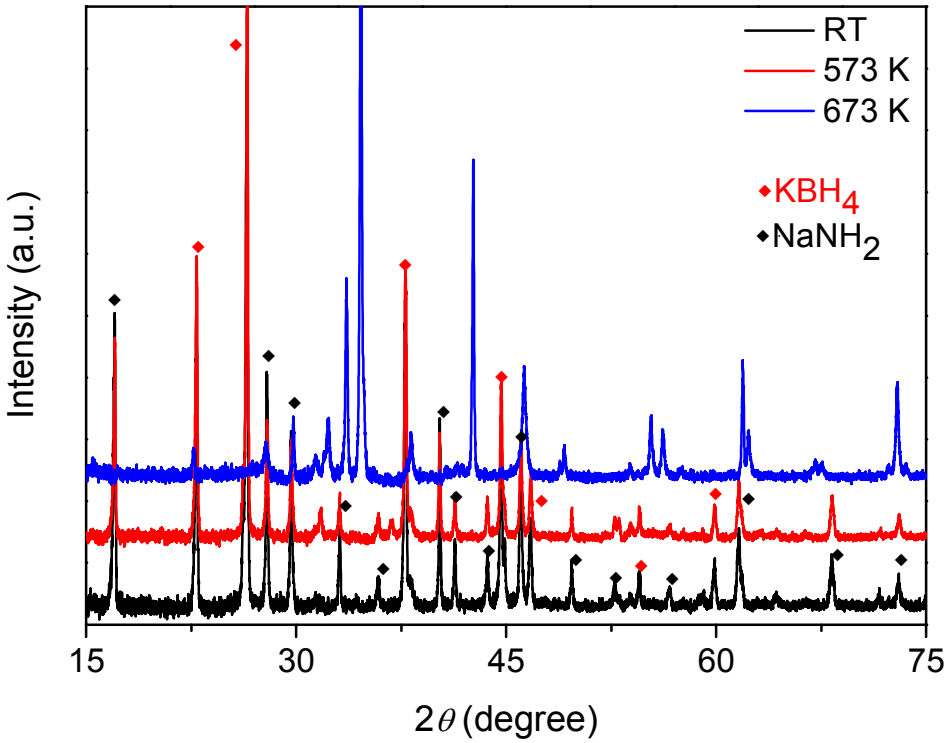

Figure 4.7: XRD diagrams of $NaNH_2$-KBH_4 (2:1 molar ratio) mixture at RT, 573 K and 673 K.

The final product of the ultimate decomposition at 673 K was investigated by XRD. The results showed surprisingly the formation of a new phase (Figure 4.7). This

new compound was identified and the thermal behavior was further investigated by DTA/TG coupled with Mass Spectroscopy and XRD experiments. The XRD diagram of the novel compound remains unchanged upon heating even up to 773 K (Appendix A). Above 773 K, the phase decomposes and yields an amorphous phase (Figure 4.8). The thermal investigations of the new compound, Na_2KBN_2, are in line with the XRD results. According to TG results of Na_2KBN_2, there is no mass loss until 823 K and above 823 K a significant mass loss is observed due to the decomposition of Na_2KBN_2. The crystal structure, space group and lattice parameters of this new compound are determined by Rietveld analysis and detailed in 4.3.1 and 4.3.1 sections.

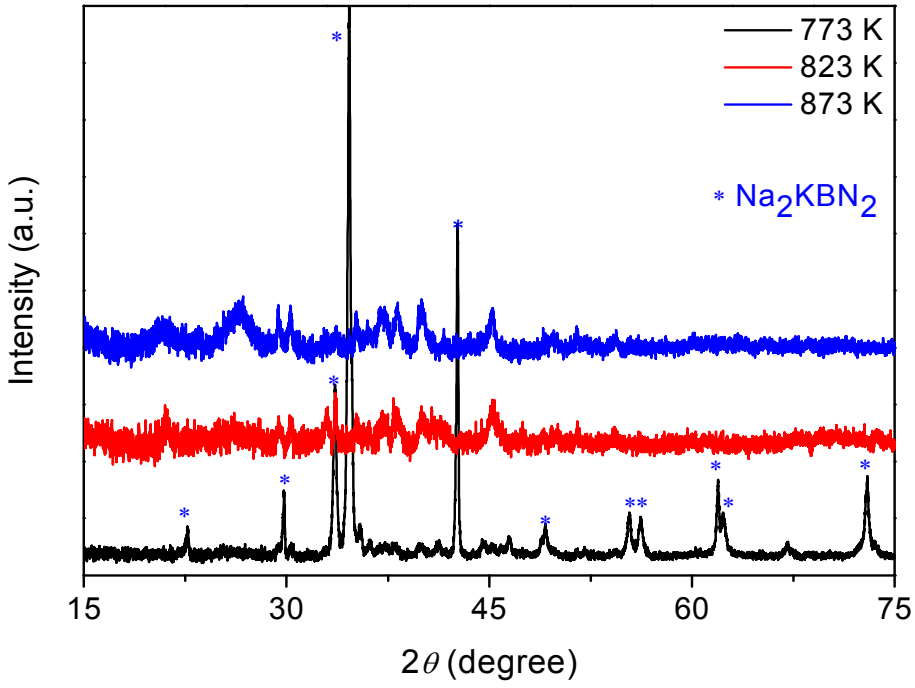

Figure 4.8: XRD diagrams of $NaNH_2$-KBH_4 (2:1 molar ratio) mixture at 773 K, 823 K and 873 K.

4.3.1 Crystal Structure Determination of Na_2KBN_2 by Rietveld Analysis

For the Rietveld refinements of Na_2KBN_2, the crystal structure parameters of Na_2KCuO_2 [98] was used as initial atomic coordinates. The theoretical and experimental XRPD diagrams of Na_2KBN_2 are given in Figure 4.9. The additional peak at 2θ = 31.36° in the experimental XRD results from Na_3BN_2 impurity. Structure parameters and refinement data of Na_2KBN_2 are summarized in Table 4.1, the atomic coordinates and displacement parameters for Na, K, B and N are depicted in Table 4.2.

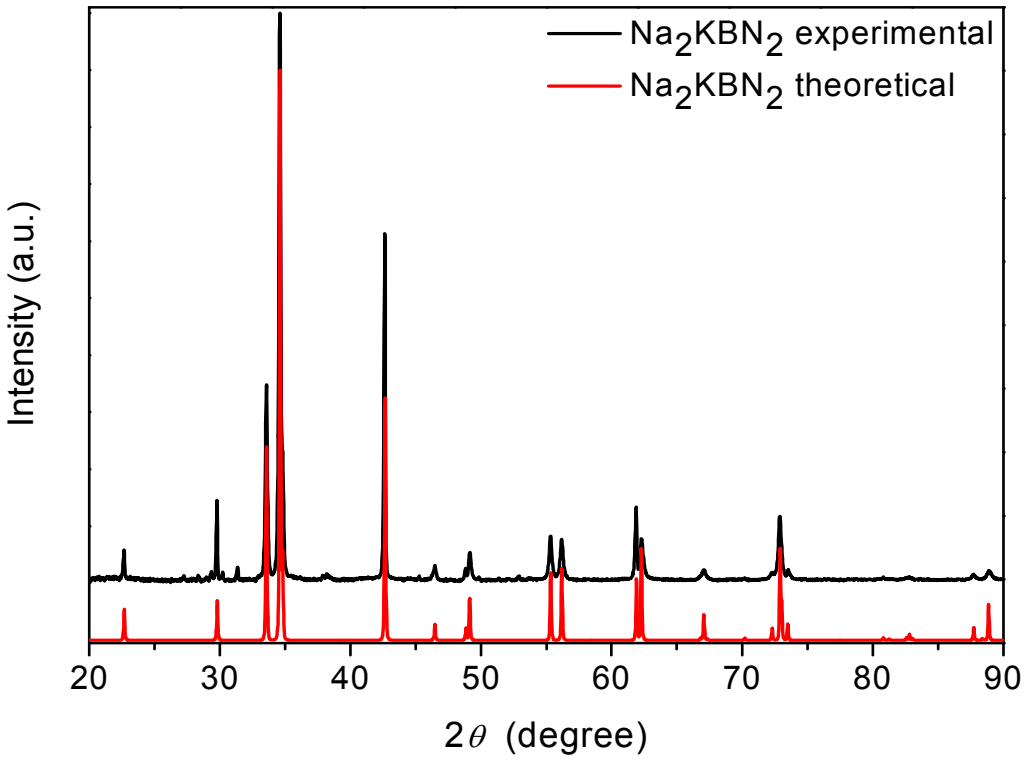

Figure 4.9: Experimental and theoretical XRD diagrams of Na_2KBN_2.

Table 4.1: The crystallographic data and refinement details for Na_2KBN_2.

Space group	*I* 4/*m m m* (139) – tetragonal
Unit Cell	*a* = 4.2359(0)Å, *c* = 10.3014(2)Å c/a = 2.4319 *V* = 184.837(6) Å^3, *Z* = 2
Calculated density	2.2262(1) g/cm^3
Diffractometer	Huber G670
Detector/Monochromator	Image Plate/Germanium
Radiation, Wavelength	Cu $K_{\alpha 1}$, 1.540598 Å
Absorption coefficient	136.19 cm^{-1}
Number of free parameters	8
Two-theta (max)	117.43
Mode of refinement	Full Profile
Program for structure solution	WinCSD [76]
R_{int}, R_{prof}	0.0455, 0.1330

Table 4.2: Atomic coordinates and displacement parameters for Na_2KBN_2.

Atom	Wyck.	Site	x/a	y/b	z/c	B(is/eq)	Ocp	U_{iso} [Å^2]
Na1	4d	-4m2	½	0	¼	1.54(5)	1	0.0195(6)
K1	2b	4/mmm	0	0	½	1.62(4)	1	0.0205(5)
N1	4e	4mm	0	0	0.1317(4)	1.90(10)	1	0.0241(13)
B1	2a	4/mmm	0	0	0	1.0(2)	1	0.013(2)

The crystal structure of Na_2KBN_2 was solved from powder data by Rietveld refinement. The compound crystallizes in the tetragonal space group *I* 4/*mmm* (No.139) with *a* = 4.2359(0) Å, *c* = 10.3014(2) Å and *Z* = 2. The crystal structure is characterized by elongated rhombic dodecahedra M_{14} (Fig. 4.10) formed by 8 Na and 6 K atoms each which are centered by the linear $[N–B–N]^{3–}$ anions. The $(BN_2)@Na_{8/4}K_{6/6}$ polyhedra

are stacked along [001] and condensed via common tetragonal faces to generate a space-filling 3D arrangement (Fig. 4.11).

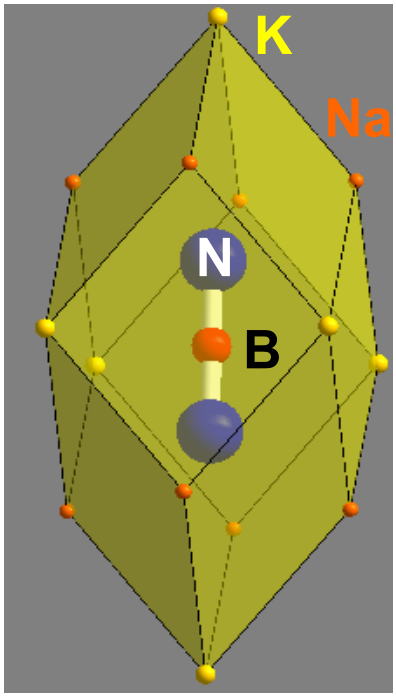

Figure 4.10: $\{(BN_2)@Na_{8/4}K_{6/6}\}$coordination polyhedron (BN_2-centered rhombic dodecahedron).

Thus, the chemical composition of each filled polyhedron represents at the same time the chemical formula of the compound: $(BN_2)@Na_{8/4}K_{6/6} \equiv (BN_2)Na_2K$. The (B–N) bonds length for the strictly linear $[N–B–N]^{3-}$ units is: d(B–N) = 1.357(4) Å. The B atoms are further surrounded by 2 sets of 4×Na and a set of 4× K atoms each, at a distance of d(B–Na) = 3.334(4) Å and d(B–K) = 2.995(2) Å, respectively. Additional two potassium atoms at larger distance (d(B–K) = 5.151(1)Å) complete the rhombic dodecahedron. The nitrogen ligands are mono-capped square-antiprismatically coordinated by four sodium (d(N–Na) = 2.444(2) Å) and 4+1 potassium atoms each (d(N–K) = 3.288(2)(4×) Å, 3.794(4) (1×) Å). The alkali metal atoms in turn are

coordinated by 4 (Na) and 8 (K) nitrogen neighbors in a tetrahedral and cube-like arrangement, respectively.

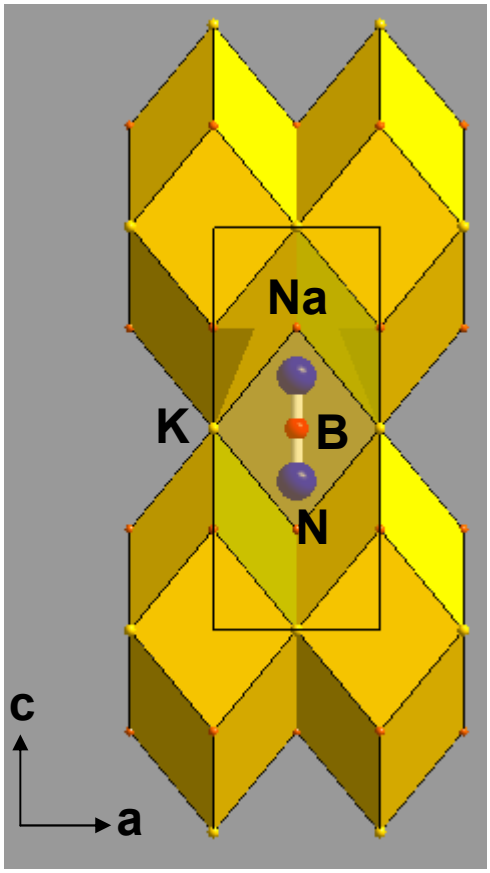

Figure 4.11 Crystal structure of Na_2KBN_2 built up by condensed $(BN_2)@Na_{8/4}K_{6/6}$ polyhedra (rhombic dodecahedron) stacked along [001].

4.3.2 Vibrational Spectroscopy Analysis of Na_2KBN_2

The relevant moieties for the vibrational spectra of Na_2KBN_2 are the linear $[N–B–N]^{3-}$ with the point group symmetry $D_{\infty h}$. The four fundamentals are distributed as:

$$\Gamma_{vib}(D_{\infty h}) = \Sigma_g(\nu_1, R) + \Sigma_u(\nu_2, IR) + \Pi_u(\nu_3, IR) \qquad \text{(eq. 4.5)}$$

The modes with the parity *g* are only Raman and those with *u* are only IR active. In the crystalline Na_2KBN_2, the boron atoms are centering the position 4/mmm/D_{4h}. In this case, the Σ_g, Σ_u and Π_u modes in $D_{\infty h}$ transforms as A_{1g}(R), A_{2u} (IR) and E_u (IR) (D_{4h}), meaning that the selection rules for the free anion ($D_{\infty h}$) will be holding also for the solid. The *I* centered unit cell contains two and the spectroscopic primitive cell only one $[BN_2]^{3-}$ group, so that a factor group splitting is strictly to be excluded. The $^{11}B/^{10}B$ isotope splitting is expected only for the antisymmetric valence vibration ν_2 and the deformation ν_3 in which the central boron atom is displaced.

In accordance with the predictions, the vibrational spectra of Na_2KBN_2 are very simple, the expected three internal modes and the isotope splitting are observed. In Figure 4.12, the symmetric stretch is observed exclusively in the Raman spectrum at ν_1 = 1013 cm^{-1}. Due to isotope splitting the ν_2 and ν_3 modes appear as an IR doublet each, at ν_2 = 1631 cm^{-1} (^{11}B), 1693 cm^{-1} (^{10}B) and ν_3 = 604 cm^{-1} (^{11}B), 627 cm^{-1} (^{10}B), respectively. With these wavenumbers following set of force constants were obtained: f(B–N) = 7.29 Ncm^{-1}, f' = 1.18 $Ncm^{-1}$and f_D = 0.42 Ncm^{-1}. The present results are directly comparable with those of Na_3BN_2 and the vibrational data for the other well-known nitridoborates [99-101].

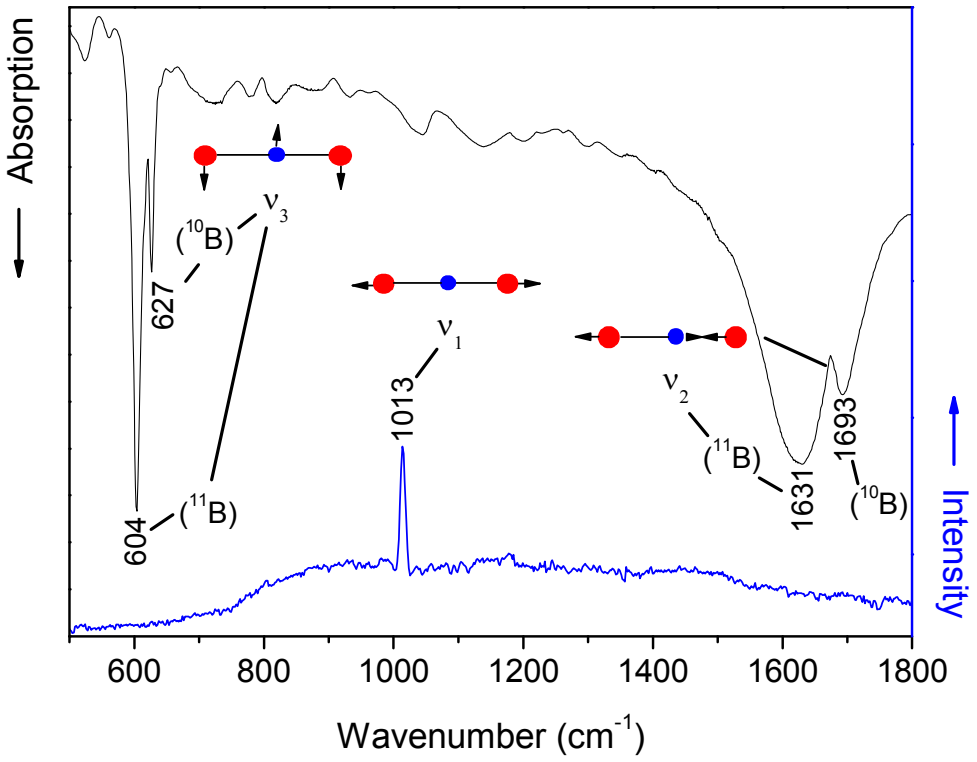

Figure 4.12: Vibrational spectra of Na_2KBN_2.

As a summary, the thermal decomposition behaviors of these three systems ($LiNH_2$-$NaBH_4$, $LiNH_2$-KBH_4 and $NaNH_2$-KBH_4) were investigated in detail. Besides, the end products after decompositions of these systems were characterized by XRPD and vibrational spectroscopy analyses. The results are given in Table 4.3.

Comparison of the three systems showed, that the starting temperature for H_2 release is the lowest for the $NaNH_2$ -KBH_4 system. In each case the H_2 release was accompanied by NH_2 and NH_3 evolution. In the $LiNH_2$ -$NaBH_4$ and $LiNH_2$ -KBH_4 systems this originated from the decomposition of $LiNH_2$. In the $NaNH_2$ -KBH_4 system similarly release of NH_2 and NH_3 can be again connected to -NH_2 containing compound.

The accompanying gases, both on volumetric and weight basis, was found as the lowest for the $NaNH_2$ -KBH_4 system where unfortunately also the smallest amount of

hydrogen was detected. Both the theoretical and experimental results showed that the largest amount of hydrogen can be stored in $LiNH_2$ -$NaBH_4$ mixture at the molar ratio of 2:1. The maximum hydrogen release temperature 667 K was found as the lowest for this system and the starting temperature of the hydrogen is also relative low value (621 K). The starting temperature of hydrogen release can be decreased most probably in the presence of catalysts which are the target of our prospective research. Based on these results $LiNH_2$ -$NaBH_4$ system is one of the most promising among the investigated three systems as hydrogen storage material.

Table 4.3: The summary of the decomposition behaviors of the new amide-borohydride systems.

System (2:1 molar ratio)	**$LiNH_2$-$NaBH_4$**	**$LiNH_2$-KBH_4**	**$NaNH_2$–KBH_4**
H_2 release starts at (K)	621	683	596
H_2 release max. at (K)	667	727	700
Theoretical H_2 density (wt%)	9,5	8,0	6,1
End products after dehydrogenation	Li_3BN_2, Na, amorphous B, NH_3, H_2	Li_3BN_2, K, amorphous B, NH_3, H_2	Na_2KBN_2, NH_3, H_2

Chapter 5

CONCLUSION

The aim of the thesis work was to characterize novel complex hydride mixtures for hydrogen storage. The investigations were focused on four complex hydride systems: ball milled *$NaBH_4$-$NaNH_2$* and thermally treated *$LiNH_2$-$NaBH_4$*, *$LiNH_2$-KBH_4*, *$NaNH_2$-KBH_4* mixtures.

The previous experimental results on thermally treated $NaBH_4$-$NaNH_2$ mixture indicated a two step reaction: in the first step a new compound, α- and β-Na_2BNH_6, was formed and identified first time in our group. The dehydrogenation took place in the second step where the ultimate end product, Na_3BN_2, was produced.

A new synthesis route using ball milling method was introduced in this thesis work for the same system ($NaBH_4$-$NaNH_2$ mixture). The mechanochemical treatment of the $NaBH_4$-$NaNH_2$ mixture at different ratios by ball milling was shown to be a suitable and successful method for the synthesis of α-Na_2BNH_6 similar to the thermal treatment method. The observed two step reactions can be written as shown below:

$$2NaNH_{2(s)} + NaBH_{4(s)} \xrightarrow{\text{Ball milling}} \alpha\text{-}Na_2BNH_{6(s)} + NaNH_{2(s)} \xrightarrow{HEAT} Na_3BN_{2(s)} + 4H_{2(g)}$$

The thermal decomposition analysis showed that the synthesis method had no effect on the hydrogen release behavior of the new compound α-Na_2BNH_6. Both mechanochemically and thermally synthesized Na_2BNH_6 started releasing hydrogen at ~553 K in the absence of additives.

Following the characterization of mechanochemically synthesized Na_2BNH_6, the effect of transition metal catalysts on the hydrogen release temperature and the reversibility of the reaction was studied. Transition metals (Pt, Pd, Ni and Ti), their chlorides and some of their carbon black supported forms were added into the mixture by dry doping to decrease the hydrogen release temperature of the resulting products. It

was found that Ti and $TiCl_3$ additions did not affect the dehydrogenation temperature of Na_2BNH_6, but Pt, Pd, Ni were successful in decreasing the onset of dehydrogenation to ~60 K. The most significant improvement was achieved in the presence of Pt/Vulcan carbon and Pd/Black Pearls 2000. The dehydrogenation temperature was decreased to ~396 K with 5.6 wt% Pt/Vulcan carbon and to ~392 K with 2.9 wt% Pd/Black Pearls 2000 addition. 60% improvement in the onset of dehydrogenation temperature together with nearly 7 wt% H_2 gravimetric capacity make this system very promising hydrogen storage system.

The rehydrogenation experiments were performed with and without Pt/Vulcan additives on Na_3BN_2 samples. Only the formation of NaH was observed in the XRPD diagram for the pure Na_3BN_2 compound after 400 bar hydrogen loading at 473 K and for the sample with Pt/Vulcan, after 350 bar H_2 load at 373 K. Under these conditions the reversibility of the hydrogen release was not successful. Altering the catalyst-carbon support ratios at different hydrogen loads and times can offer a solution for this problem in ongoing investigations.

The thermal decomposition behaviors of new alkali metal amide-borohydride systems $LiNH_2$-$NaBH_4$, $LiNH_2$-KBH_4 and $NaNH_2$-KBH_4 were also investigated. The onset of hydrogen release and the temperature where it peaks were determined for the above three systems. Based on thermal analysis results, the theoretical and the experimental gravimetric hydrogen capacity were compared in different systems. The possible reaction mechanism was defined and the intermediate products -if any- were identified.

It was shown that dehydrogenation of the $LiNH_2$-$NaBH_4$ system occurs in two steps without formation of any crystalline intermediate phase. In the first step the hydrogen release started at 621 K and ~70 % of the total hydrogen was released together with small amount of NH_2, NH_3 gases. The presence of these gases was connected to the decomposition of $LiNH_2$. The second dehydrogenation step started at 724 K. After dehydrogenation, the final products found in this system were Li_3BN_2, Na and B.

The hydrogen release in the $LiNH_2$-KBH_4 system started at 683 K and was accompanied by high amount of NH_3 gases which indicated that KBH_4 catalyzed the decomposition of $LiNH_2$. The end products Li_3BN_2, K, and B showed similarities with the previous system.

Among these three systems, dehydrogenation starting temperature was the lowest (596 K) in the $NaNH_2$-KBH_4 mixture and it peaked at 700 K. A new compound, Na_2KBN_2, was observed and identified as the decomposition product of the $NaNH_2$-KBH_4 mixture. The analysis of the X-ray powder diffraction data showed that the new compound crystallized in the tetragonal space group; I 4/mmm (No.139). The lattice constants were a = 4.2359(0) Å, c = 10.3014(2) Å, and Z = 2.

Comparison of the three systems showed that in each case the H_2 release was accompanied by NH_2 and NH_3 evolution. In the $LiNH_2$-$NaBH_4$ and $LiNH_2$-KBH_4 systems, this originated from the decomposition of $LiNH_2$. Similarly in the $NaNH_2$-KBH_4 system, the release of NH_2 and NH_3 can be connected to -NH_2 containing compound.

The accompanying gases were found to have the lowest volume fraction for the $NaNH_2$-KBH_4 system where unfortunately the absolute amount of the detected hydrogen was also the smallest. Both the theoretical and experimental results showed that the largest amount of hydrogen can be stored in $LiNH_2$ -$NaBH_4$ mixture (~10 wt%) at the molar ratio of 2:1. For this system, the maximum hydrogen release temperature (667 K) was also found to be the lowest while the starting temperature of the hydrogen release was 621 K, slightly above the lowest starting temperature (596 K) which was observed in the $NaNH_2$-KBH_4 system. The starting temperature of hydrogen release can be decreased most probably in the presence of catalysts which are the target of future research. Based on these results $LiNH_2$ -$NaBH_4$ system is one of the most promising among the investigated three systems as hydrogen storage material.

BIBLIOGRAPHY

1. J.M. Roberts, “Yirminci Yüzyıl Tarihi”, 2003, Dost Yayınevi, Ankara, p.49.
2. http://www.iags.org/futureofoil.html
3. http://www.eia.doe.gov/pub/oil_gas/petroleum/presentations/2000/long_term_supply/index.htm
4. E. Fakihoğlu, Y. Yürüm, T.N. Veziroğlu, *Int. J. Hydrogen Energy*, 29 (2004) 1371.
5. M. Jacoby, “Filling up with hydrogen”, *C&EN*, August 22, (2005)
6. Hydrogen Storage “Think-Tank” Report, March 14, 2003, Washington, DC.
7. M. Altmann, C. Graesel, “The acceptance of hydrogen technologies”. Available from: http://www.hyweb.de/accepth2/ , 1998.
8. K. Haraldson, A. Folkesson, M. Saxe, P. Alvfors, *Int. J. Hydrogen Energy*, 31 (2006) 317.
9. L. Zhou, Renewable and Sustainable Energy Reviews, 9 (2005) 395.
10. M. Ricci, P. Bellaby, R. Flynn, *Int. J. Hydrogen Energy,* 33 (2008) 5868.
11. A. Züttel, “Materials for hydrogen storage” *Materials Today*, September 2003.
12. F.E. Pinkerton, B.G. Wicke, “Bottling the hydrogen genie” *The Industrial Physicist*, vol. 10, issue 1, February/March 2004, 20.
13. http://www.greencarcongress.com/2006/09/bmw_announces_m.html
14. D.K. Ross, *Vacuum*, 80 (2006) 1084.
15. G. Liang, J. Huot, S. Boily, A.V. Neste, R. Schulz, *J. Alloys Comp.* 292 (1999) 247.
16. A. Zaluska, L. Zaluski, J.O. Ström-Olsen, *Appl. Phys. A*, 72 (2001) 157.
17. W. Luo, E. Rönnebro, *J. Alloys Comp.* 406-406 (2005) 392.
18. F. Schülth, B. Bogdanovic, M. Felderhoff, *Chem. Commun*. (2004) 2249.
19. W. Grochala, P.P. Edwards, *Chem. Rev.* 104 (2004) 1283.

20. B. Bogdanovic, M. Schwickardi, *J. Alloys Comp.* 253 (1997) 1.
21. B. Bogdanovic, M. Schwickardi, *Appl. Phys. A*, 72 (2001) 221.
22. S. Suda, Y.M. Sun, B.H. Liu, Y.Zhou, S. Morimitsu, K. Arai, N. Tsukamoto, M. Uchida, Y. Candra, Z.P. Li, *Appl. Phys. A*, 72 (2001) 209.
23. P. Chen, Z.Xiong, J. Luo, J. Lin, K.L. Tan, *Nature*, 420 (2002) 302.
24. A. Zaluska, L. Zaluski, J.O. Ström-Olsen, *J. Alloys Comp.,* 298 (2000) 1.
25. J.J. Vajo, G.L. Olson, *Scriptica Materialia*, 56 (2007) 829.
26. R.A. Zidan, S. Takara, A.G. Hee, C.M. Jensen, *J. Alloys Comp.,* 285 (1999) 119.
27. M. Resan, M.D. Hampton, J.K. Lomness, D.K. Slattery, *Int. J. Hydrogen Energy,* 30 (2005) 1417.
28. B. Bogdanovic, R.A. Brand, A.Marjanovic, M. Schwickardi, J. Tölle, *J. Alloys Comp.,* 302 (2000) 36.
29. J. Graetz, J.J. Reilly, *Scriptica Materialia*, 56 (2007) 835.
30. C.M. Jensen, R. Zidan, N. Mariels, A. Hee, C. Hagen, *Int. J. Hydrogen Energy,* 24 (1999) 461.
31. C.M. Jensen, K.J. Gross, *Appl. Phys. A*, 72 (2001) 213.
32. V.P. Balema, J.W. Wiench, K.W. Dennis, M. Pruski, V.K. Perchasky, *J. Alloys Compd*. 329 (2001) 108.
33. J. Chen, N. Kuriyama, H.T. Takeshita, T. Sakai, *J. Phys. Chem. B*, 105 (2001) 11214.
34. M. Resan, M.D. Hampton, J.K. Lomness, D.K. Slattery, *Int. J. of Hydrogen Energy* 30 (2005) 1417.
35. R. Genma, N. Okada, T. Sobue, H.H. Uchida, *Int. J. Hydrogen Energy,* 31 (2006) 309.
36. G.P. Meisner, G.G. Tibbets, F.E. Pinkerton, C.H. Olk, M.P.Balogh, *J. Alloys Comp.,* 337 (2002) 254.
37. W. Luo, *J. Alloys Comp.,* 381 (2004) 284.

38. H.Y. Leng, T. Ichikawa, S. Hino, N. Hanada, S. Isobe, H. Fuji, *J. Phys. Chem. B*, 108 (2004) 8763.
39. H.Y. Leng, T. Ichikawa, S. Hino, N. Hanada, S. Isobe, H. Fuji, *J. Alloys Comp.,* 404-406 (2005) 443.
40. Z.T. Xiong, G.T. Wu, J.J. Hu, P. Chen, *J. Power Sources*, 159 (2006) 167.
41. Y. Kojima, M. Matsumo, Y. Kawai, *J. Phys. Chem. B*, 110 (2006) 9632.
42. Z.T. Xiong, J.J. Hu, G.T. Wu, Y.F. Liu, P.Chen, *Catalysis Today*, 120 (2007) 287.
43. P. Chen, Z. Xiong, G. Wu, Y. Liu, J.Hu, W. Luo, *Scriptica Materialia*, 56 (2007) 817.
44. J.J. Vajo, S.L. Skeith, F. Mertens, *J. Phys. Chem. B*, 109 (2005) 3719.
45. F.E. Pinkerton, G.P. Meisner, M.S. Meyer, M.P. Balogh, M.D. Kundrat, *J. Phys. Chem. B*, 109 (2005) 6.
46. Y. Nakamori, A. Ninomiya, G. Kitahara, M. Aoki, T. Noritake, K. Miwa, Y. Kojima, S. Orimo, *J. Power Sources*, 155 (2006) 447.
47. J.Yang, A.Sudik, D.J.Siegel, D.Halliday, A.Drews, R.O.Carter III, C. Wolverton, G.J.Lewis, J.W.A.Sachtler, J.J.Low, S.A.Faheem, D.A.Lesh, V.Ozolins, *J. Alloys Comp.* 446-447 (2007) 345.
48. P.A.Charter, P.A.Anderson, J.W.Prendergast, A.Walton, V.S.J.Mann, D.Book, W.I.F.David, S.R.Johnson, P.P. Edwards, *J. Alloys Comp.* 446-447 (2007) 350.
49. A.Züttel, S.Rentsch, P.Fisher, P. Wenger, P.Sudan, Ph. Mauron, Ch. Emmenegger, *J. Alloys Comp.* 356-357 (2003) 515.
50. S. Orimo, Y. Nakamori, A.Züttel, *Mater. Sci. Eng. B*, 108 (2004) 51.
51. P.Vajeeston, P.Ravindran, A. Kjekshus, H. Fjellvag, *J. Alloys Comp.*, 387 (2005) 97.
52. Y. Nakamori, K. Miwa, A. Ninomiya, H. Li, N. Ohba, S. Towata, A. Züttel, S. Orimo, *Phys. Review B* , 74 (2006) 45126.
53. Y. Nakamori, S. Orimo, *J. Alloys Comp.* 370 (2004) 271.

54. Y. Nakamori, H.W. Li, K.Kikuchi, M. Aoki, K. Miwa, S. Towata, S. Orimo, *J. Alloys Comp.* 446-447 (2007) 296.
55. F.E. Pinkerton, *J. Alloys Comp.* 400 (2005) 76.
56. M. Aoki, K. Miwa, T. Noritake, G. Kitahara, Y. Nakamori, S. Orimo, S. Towata, *Appl. Phys. A* 80 (2005) 1409.
57. A.Züttel, S.Rentsch, P.Fisher, P. Wenger, P.Sudan, Ph. Mauron, Ch. Emmenegger, *J. Power Sources* 118 (2003) 1.
58. F.E. Pinkerton, M.S.Meyer, G.P.Meisner, M.P.Balogh, *J. Phys. Chem. B,* 110 (2006) 7967.
59. F.E. Pinkerton, M.S.Meyer, G.P.Meisner, M.P.Balogh, *J. Alloys Comp.,* 433 (2007) 282.
60. S. Acar, "Sodium Amide-Sodium Tetrahydridoborate System as a Potential Hydrogen Storage Material." MS Thesis, Graduate School of Sciences and Engineering, Koc University, July 2007
61. P.A. Charter, P.A. Anderson, J.W. Prendergast, A. Walton, V.S.J. Mann, D. Book, W.I.F. David, S.R. Johnson, P.P. Edwards, *J. Alloys and Compd.* 446-447 (2007) 350.
62. M.Somer, S.Acar, C.Koz, I.Kokal, P.Höhn, U.Aydemir, R.Cardoso-Gil, L.Akselrud, *Submitted,* (2009).
63. J.F. Fernandez-Bertran, *Pure Appl. Chem*., 71 (1999) 581.
64. V.V.Boldryev, *Solid State Ionics*, 63-65 (1993) 537.
65. V.V. Boldyrev, K. Tkacova, *J. Material Synthesis and Processing*, 8, ¾ (2000) 121.
66. P. Butyagin, *J. Material Synthesis and Processing*, 8, ¾ (2000) 205.
67. E. Ivanov, C. Suryanarayana, *J. Material Synthesis and Processing*, 8, ¾ (2000) 235.
68. U. Steinike, K. Tkacova, *J. Material Synthesis and Processing*, 8, ¾ (2000) 197.
69. H. Mio, J. Kano, F. Saito, *Chem. Eng. Sci.*, 59 (2004) 5909.

70. H. Mio, J. Kano, F. Satio, K. Kaneko, *Mat. Sci. Eng. A*, 332 (2002) 75.
71. C. Suryanarayana, *Progress in Materials Science* 46 (2001) 15.
72. R. Jenkins, R.L. Snyder, *Introduction to X-ray Powder Diffractometry*, 1996, John Wiley & Sons, Inc., New York, 48.
73. http://serc.carleton.edu/details/images/9514.html
74. B.D. Cullity, S.R. Stock, *Elements of X-ray Diffraction*, 2001, 3rd ed., Prentice Hall, New Jersey, 103.
75. R.A. Young, *The Rietveld Method*, 1993, Oxford University Press Inc., New York, 2.
76. L.G. Akselrud, P.Yu. Zavalii, Yu.N. Grin, V.K. Pecharsky, B. Baumgartner, E. Wölfel, Materials Science Forum 133-136 (1993) 335.
77. G. Cao, *Nanostructures and Nanomaterials: Synthesis, Properties and Applications*, 2004, Imperial College Press Inc., London, 332.
78. A. Wieckowski, E.R.Savinova, C.G.Vayenas, *Catalysis and Electrocatalysis at Nanoparticle Surfaces*, 2003, CRS Press, New York, 410.
79. M.E. Brown, *Introduction to Thermal Analysis Techniques and Applications*, 2001, 2nd ed., Kluwer, New York, 55.
80. R.F. Speyer, *Thermal Analysis of Materials*, 1994, Marcel Dekker Inc., New York, 121.
81. W. Henderson, J.S. McIndoe, *Mass Spectrometry of Inorganic, Coordination and Organometallic Componds: Tools Techniques Tips*, 2005, John Wiley&Sons, Inc., England, 1.
82. ThermoStar, GSD 301 T User Manual 2002.
83. C.G. Herbert, R.A.W. Johnstone, *Mass Spectroscopy Basics*, 2003, CRC Press, Boca Raton, 164.
84. C.M. Barschik, D.C.Duckworth, D.H. Smith, *Inorganic Mass Spectrometry: Fundamentals and Applications,* 2000, Marcel Dekker, Inc., New York, 53.
85. R.M. Smith, K.L. Busch, Understanding Mass Spectra: A Basic Approach, 1999, John Wiley&Sons, Inc.,New York, 12.

86. Jasco, Model FT/IR-600 Plus Function Manual 2001.
87. Bruker, RFS 100 User Manual 2004.
88. G.W. Parshall, S.D. Ittel, *Homogeneous Catalysis; The Applications and Chemistry of Catalysis by Soluble Transition Metal Complexes*, 1992, 2nd Edition, John Wiley & Sons Inc., New York
89. J.A. Anderson, M.F. Garcia, *Catalytic Science Series-Vol. 5: Supported Metal in Catalysis*, 2005, Imperial College Press, New York, 123.
90. D. Hua, Y. Hanxi, A. Xinping, C. Chuansin, *Int. J. Hydrogen Energy*, 28 (2003) 1095.
91. G. Padro, F. Lau, *Advances in Hydrogen Energy*, 2000, Kluwer Academic Publishers, New York, 232.
92. R. Janot, A. Rougier, L. Aymard, C. Lenain, R. Herrera-Urbina, G. A. Nazri, J. M. Tarascon, *J. Alloys Compd*, 356-357 (2003) 438.
93. J.J. Spivey, Catalysis: Volume 16, Royal Society of Chem., (2002), Cambridge
94. http://www.basf-fuelcellproducts.com/custom/index.php
95. D. Ficher, M. Jansen, *Angew. Chem. Int. Ed.*, 41, (2002), 1755.
96. R. G. Pearson, *Science*, 151 (1966) 172.
97. T. Ichikawa, S. Isobe, N. Hanada, H. Fujii, *J. Alloys Comp*. 365 (2004) 271.
98. W. Losert and R. Hoppe, *Z. Anorg. Allg. Chem.*, 515 (1984) 87.
99. M. Somer, *Z. Naturforsch.* 46b (1991) 1664.
100. M. Somer, U. Herterich, J. Curda, W. Carrillo–Cabrera, A. Zürn, K. Peters, H.G von Schnering, *Z. Anorg. Allg. Chem.* 626 (2000) 625.
101. M. Somer, Ö. Yaren, O. Reckeweg, Y. Prots, W. Carrillo-Cabrera, *Z. Anorg. Allg. Chem.*, 630 (2004) 1068.

APPENDIX A: XRD DIAGRAMS

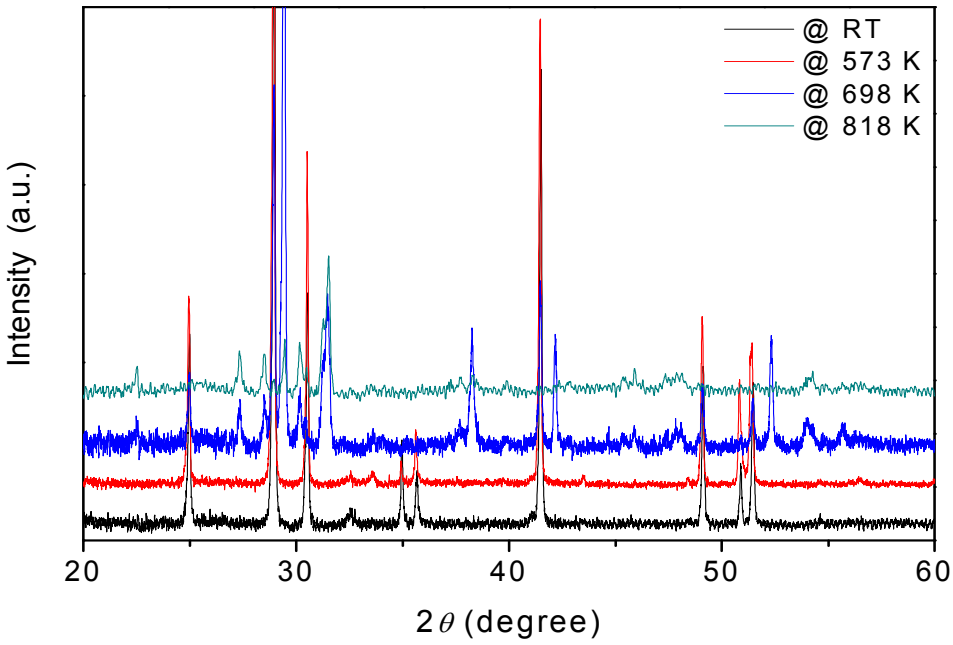

Figure A.1: XRD diagrams of 1:1 molar ratio $LiNH_2$-$NaBH_4$ mixture at different temperatures.

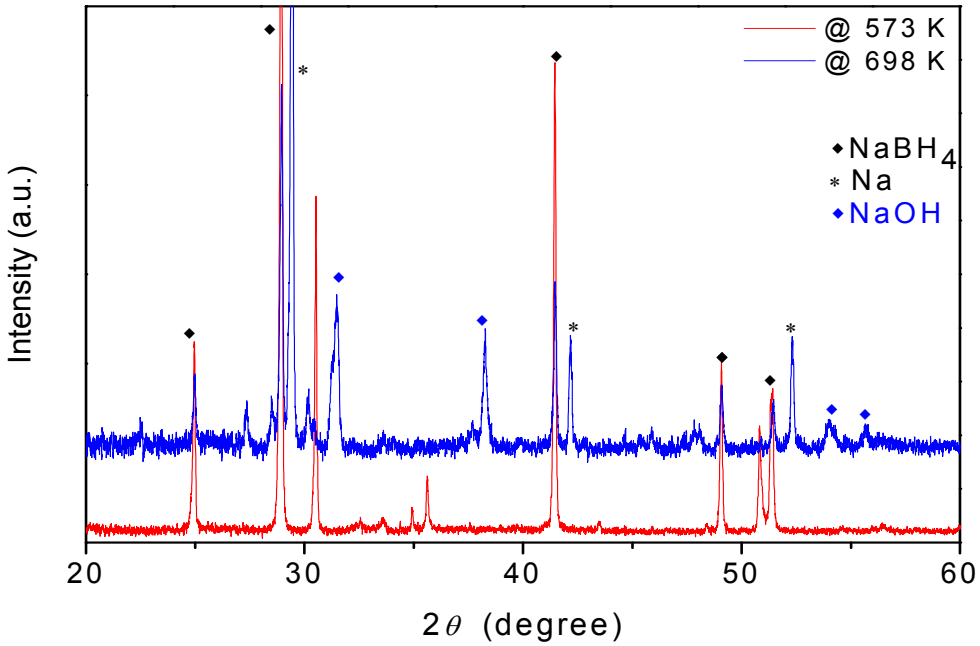

Figure A.2: XRD diagrams of $LiNH_2$-$NaBH_4$ mixture (1:1) at 573 K and 698 K.

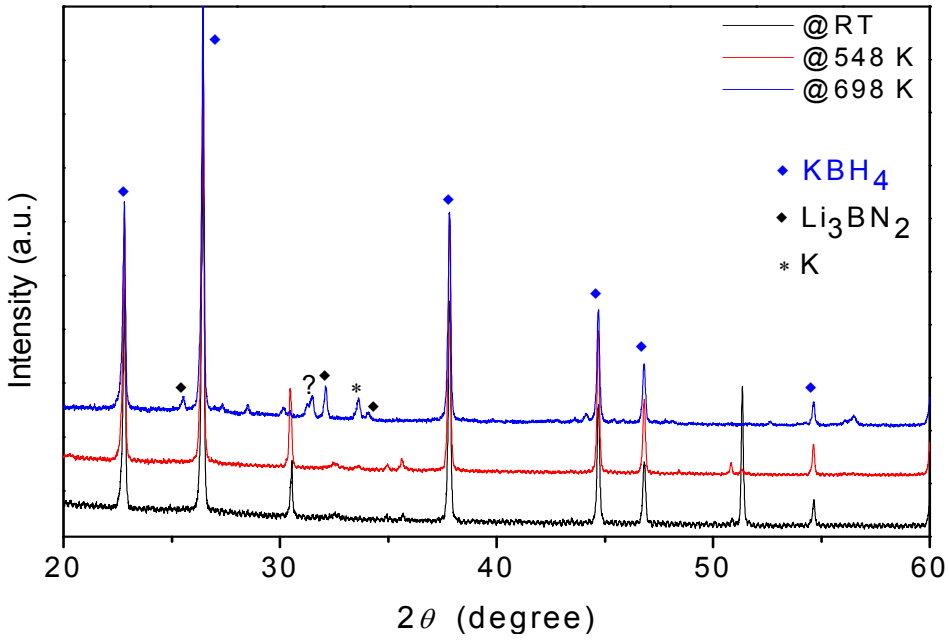

Figure A.3: XRD diagrams of 1:1 molar ratio $LiNH_2$-KBH_4 mixture at RT, 548 K and 698 K.

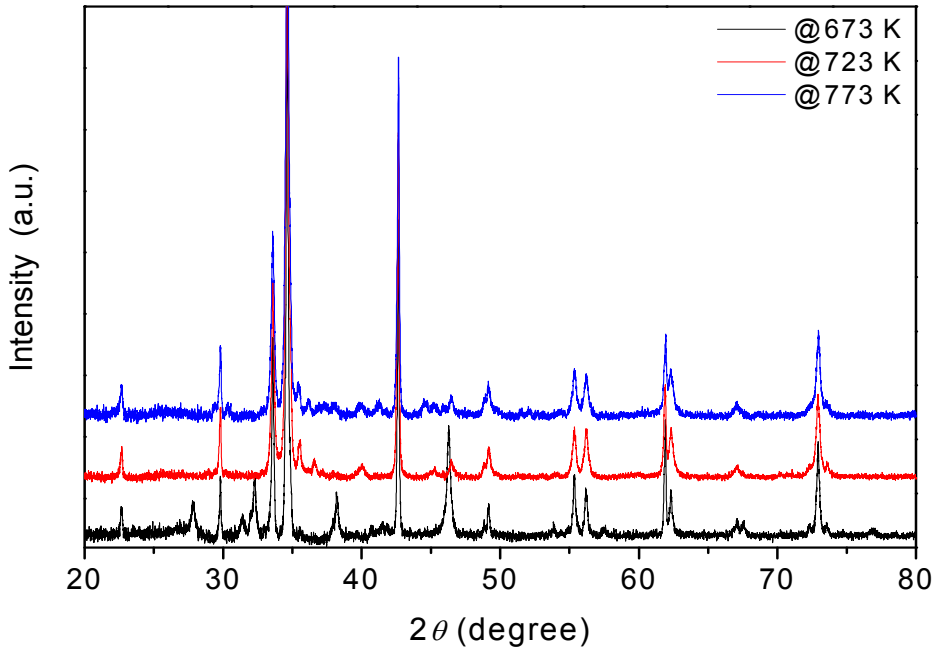

Figure A.4: XRD diagrams of 2:1 molar ratio $NaNH_2$-KBH_4 mixture at 673 K, 773 K and 823 K.

APPENDIX B: DTA/TG DIAGRAMS & MASS SPECTROSCOPY

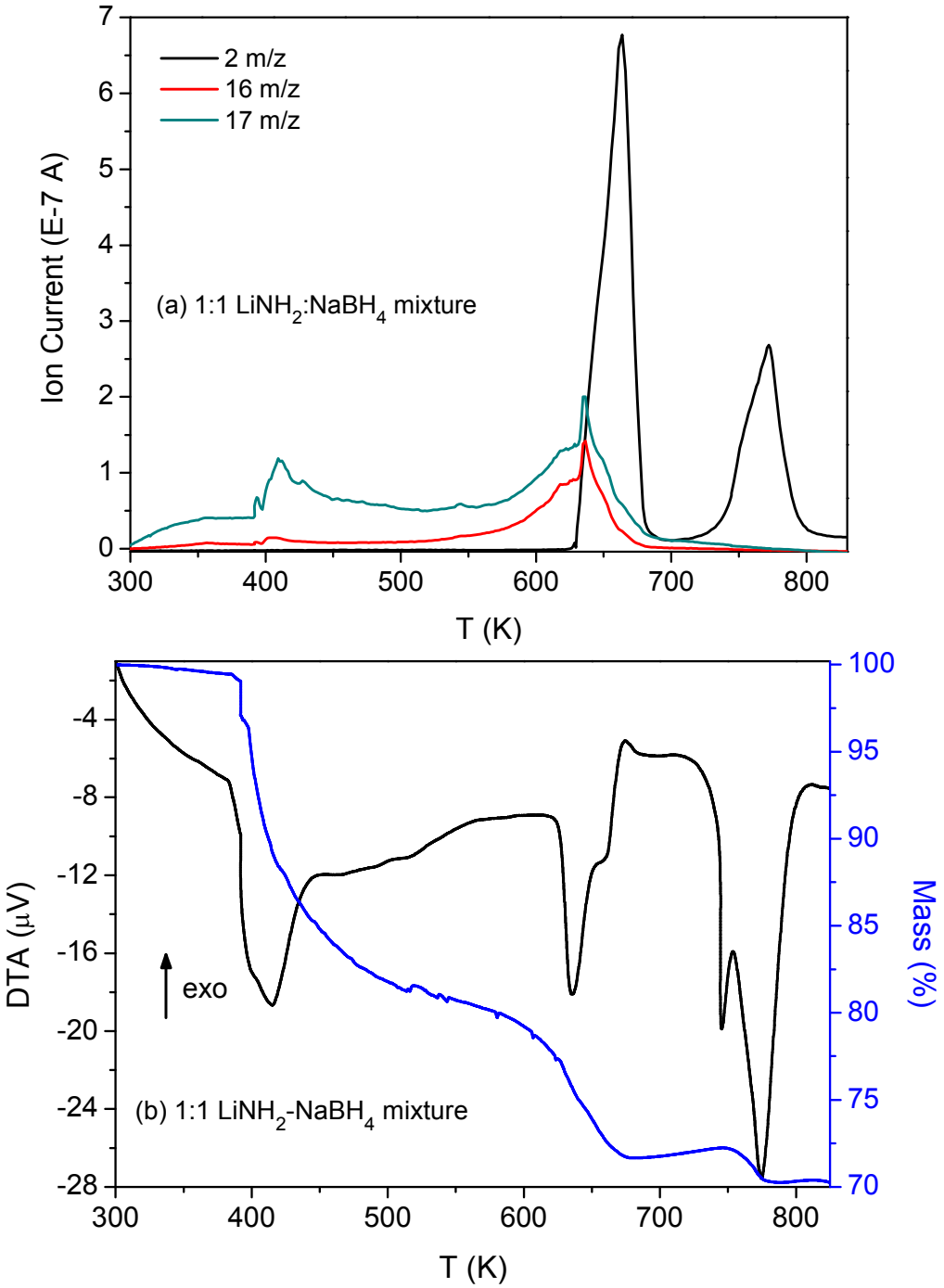

Figure B.1: Thermal decomposition analysis of 1:1 molar ratio $LiNH_2$-$NaBH_4$ mixture (a) Mass spectroscopy, (b) DTA/TG measurements.

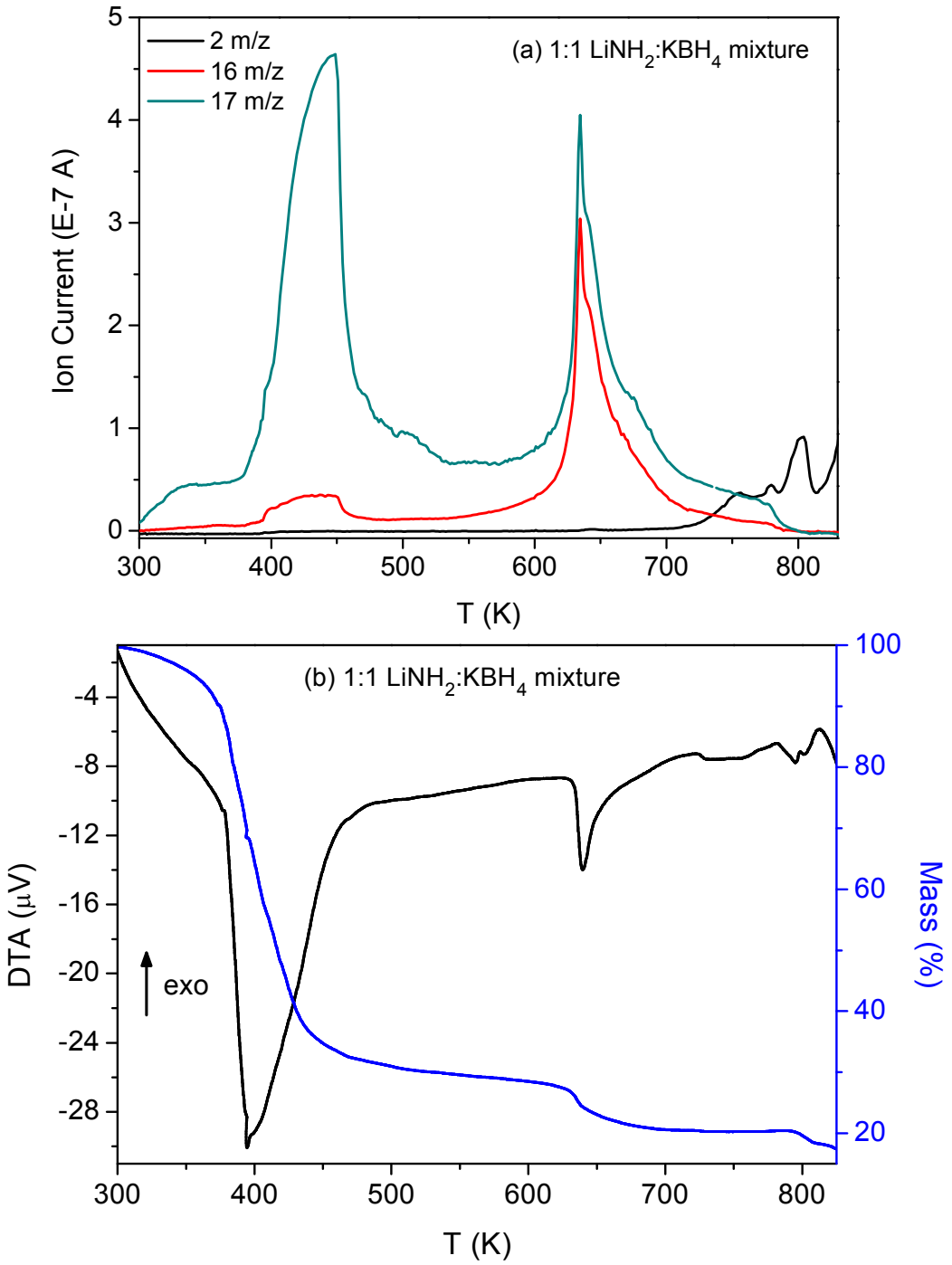

Figure B.2: Thermal decomposition analysis of 1:1 molar ratio $LiNH_2$-KBH_4 mixture (a) Mass spectroscopy, (b) DTA/TG measurements.

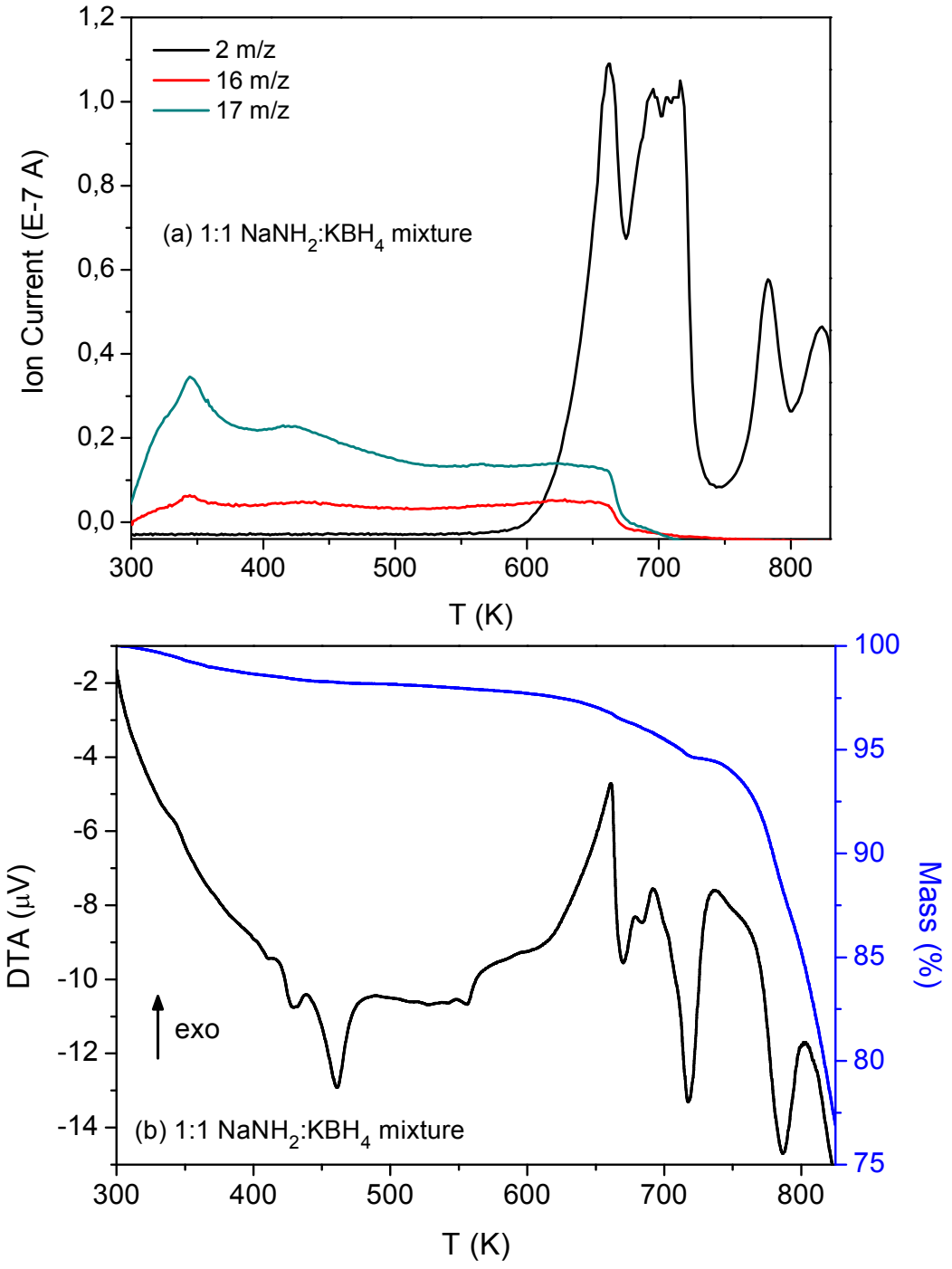

Figure B.3: Thermal decomposition analysis of 1:1 molar ratio $NaNH_2$-KBH_4 mixture (a) Mass spectroscopy, (b) DTA/TG measurements.

APPENDIX C: MASS SPECTROSCOPY DIAGRAMS

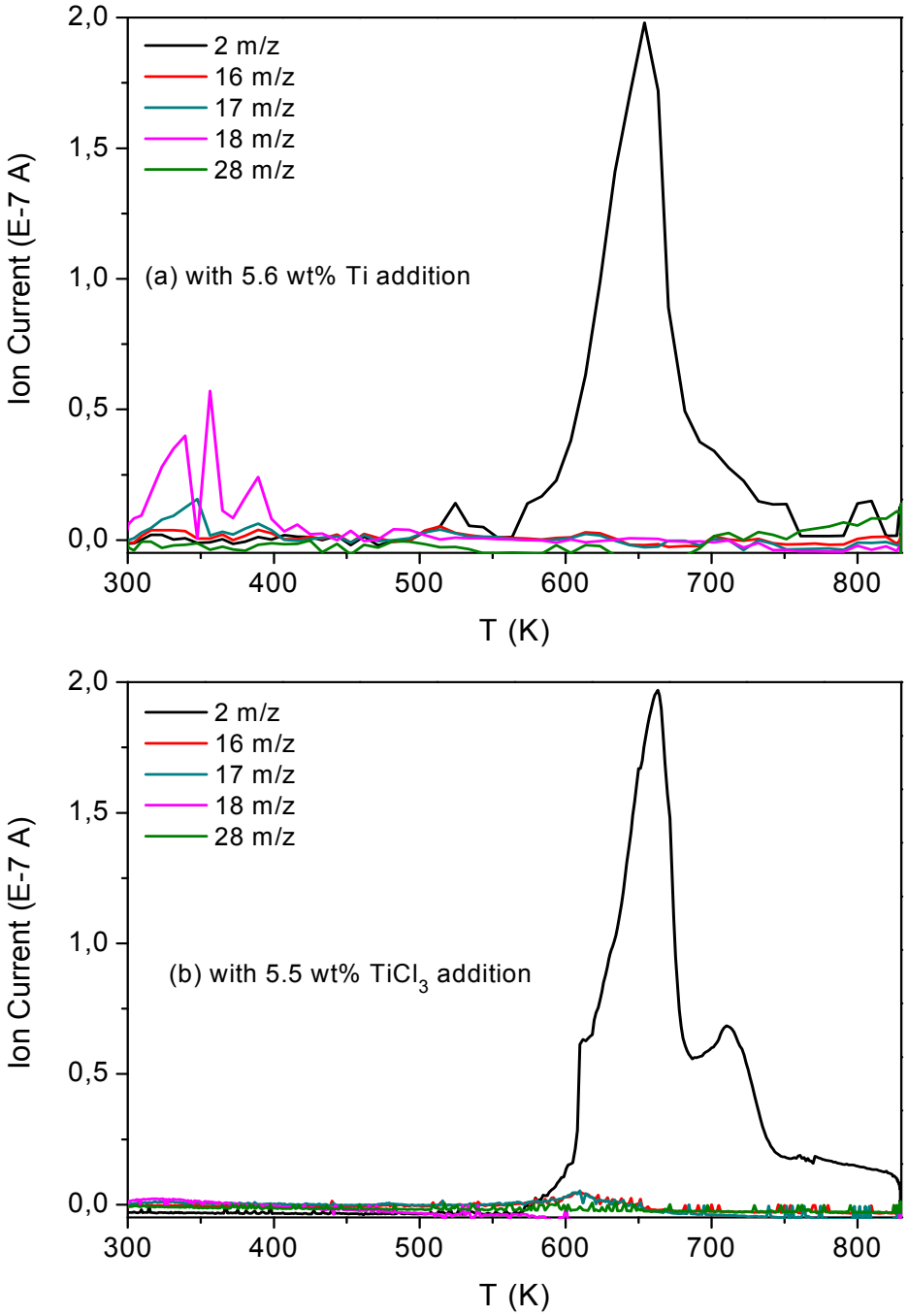

Figure C.1: Thermal decomposition graph of ball-milled $NaNH_2$-$NaBH_4$ (2:1 molar ratio) mixture (a) 5.6 wt% Ti and (b) 5.5 wt% $TiCl_3$ additions.

VITA

Cevriye Koz was born in Karaman, Turkey, on June 29, 1983. She completed her high school in Kütahya Anadolu Öğretmen Lisesi in 2001. She received the degree of Bachelor of Science in Chemistry from Bilkent University, Ankara, in May 2006. The following September she entered Koç University and is a candidate for the Master of Science Degree in Material Science and Engineering.